Design, Analysis and Fabrication of Silicon-Based Optical Materials and Photonic Crystal Devices

Umenyi Amarachukwu Valentine
Electronic and Computer Engineering
Graduate School of Engineering, Gunma University, Kiryu, Japan
ID: 07812471

A dissertation Submitted for the degree of
Doctor of Philosophy

September 2010

The dissertation of Umenyi Amarachukwu Valentine is approved by:

1. Professor Osamu Hanaizumi (Committee Chairman)

2. Professor Masahisa Itoh (Member)

3. Professor Kazumasu Takada (Member)

4. Associate Professor Kuniyuki Motojima (Member)

5. Associate Professor Kenta Miura (Member)

Day of the defense: August 3, 2010

Signature from Chairman of PhD desertation committee:

Abstract

As the integration of electronic components grow so does the need for low power, low cost, and high-speed devices. These have resulted in an increased need for complementary metal-oxide semiconductor (CMOS) compatible materials and fabrication technique for novel structures as well as accurate models of the electromagnetic field behavior in them. Recent advances in materials technology and fabrication techniques have made it feasible to consider silicon (Si)-based optical materials and photonic crystal (PhC) devices having physical dimensions of the order of the optical wavelength as the possible means to achieve these needs. Research has shown that light emission from Si is possible in low-dimensional state, i.e., Si-nanocrystals (Si-ncs). Furthermore, three-dimensional (3-D) control of light compatible with CMOS fabrication technology is required in order to fully integrate optical functionalities into the existing Si-technology. However, the difficulties in the fabrication of 3-D PhC waveguides have resulted in using two-dimensional (2-D) PhC structures. Finally, numerical simulations provide a framework for quick low-cost feasibility studies and allow for design optimization before devices are fabricated. In this dissertation, we present our efforts along these directions.

This dissertation addressed the method of obtaining high quantum efficiency from Si-ncs compatible with CMOS processing. Si ions were implanted into a fused-silica substrate (10 mm$\times$10 mm$\times$1 mm^t) at room temperature in the Takasaki ion accelerators for advanced radiation application (TIARA) of the Japan Atomic Energy Agency. The implantation energy was 80 keV, and the implantation amount was 2×10^{17} ions/cm^2. The Si-implanted substrate was cut into four pieces (5 mm$\times$5 mm$\times$1 mm^t) using a diamond-wire saw, and the four pieces were annealed in ambient air at 1100, 1150, 1200,

and 1250 ^{o}C for 25 min in a siliconit furnace. PL spectra were measured at room temperature with excitation using a He-Cd laser (λ=325 nm). Ultraviolet (UV)-PL spectra having peaks around a wavelength of 370 nm were observed from all the samples. In our experiments, the UV-PL peak had a maximum intensity after annealing at 1250 ^{o}C, and the longer wavelength PL peak around 800 nm observed from the samples annealed at 1100 and 1150 ^{o}C disappeared by annealing above 1200 ^{o}C. The two PL peaks of the Si-ion-implanted samples may have originated from interface layers between Si-ncs and SiO_2 media. However, we successfully obtained only the UV-light emission peaks by selecting the proper annealing temperatures. UV-light-emitting materials are expected to be useful as light sources for next-generation optical-disk systems whose data densities are higher than Blu-ray Disk systems.

Additionally, this dissertation addressed the numerical modeling of PhC devices. Accurate computations can provide a detailed understanding of the complex physical phenomena inherent in PhC devices. The finite-difference time-domain (FDTD) method, which is widely used by many researchers around the Globe, is a powerful tool for modeling PhC devices. We developed a modified and easy FDTD method based on a regular Cartesian Yee's lattice for calculating the dispersion diagram of triangular lattice PhCs. Our method uses the standard central-difference equation, which is very easy to implement in any computing environment. The Bloch periodic boundary conditions are applied on the sides of the unit cell by translating the periodic boundary conditions to match with the directions of periodicity in the triangular lattice. Complete and accurate bandgap information is obtained by using this FDTD approach. Convergence, accuracy, and stability analysis were carried out, which ensures the reliability of this method. Numerical results for 2-D transverse electric (TE) and transverse magnetic (TM) modes in triangular lattice PhCs are in good agreement with results from 2-D plane wave expansion method. The obtained results are in consistence with the reported ones. To ease the practical application of this method, clear explanations on the computer implementation are also provided.

Finally, this dissertation addressed the use of CMOS-compatible fabrication method and 2-D periodic structures to realize the control of light in 3-D. In particular, we designed, analyzed and fabricated novel PhC waveguides utilizing Si-ion implantation and 2-D periodic structures. The transport of ions in matter (TRIM) prediction of implantation depth distribution profile (1×10^{17} ions/cm^2, 80 keV) shows the range of about 150 nm. Assuming the effective refractive index of the Si-rich region to be 1.89 and by using FDTD method, the PhC design parameters based on the telecommunication wavelength (λ=1.55 μm) were obtained by varying the radius to lattice constant ratio (r/a) from 0.2 to 0.45. We analyzed both TE and TM mode propagation in triangular-lattice PhCs. The designed parameters were found to be a=664 nm and r/a=0.35. The PBG spanned from normalized frequency of 0.39 to 0.46 [2πc/a] in the TE-mode triangular lattice and the gap to midgap ratio was 0.16. The designed pattern was fabricated and the diameter, the period and the depth of air holes of the waveguide were estimated by atomic force microscopy (AFM) to be 464, 666 and 175 nm, respectively. Numerical results using FDTD characterization show that, straight line PhC waveguides can achieve $\approx$100% transmission, while the 60^o bend showed $\approx$80% transmission owing to the dispersion mismatch at the two 60^o bends.

These results may serve as useful guides and components in future high-density photonic integrated circuits associated with optical communications, computing, and signal processing.

There is one strong motivation I have which I think many also have. A child is born, then the child grows up and gets old and die even though he/she want to live more and more in good and sound health. LIFE is a wonderful gift. Yes, with Life we move and exist. Just like a person without life is dead, so the whole universe (including photonic crystal structure) without light is also dead. According to mankind oldest book, The Bible, Life and Light come from one source and as a lover of Life and Light, I want to dedicate this piece of knowledge **To** Jehovah God, The source of Life and True Light, Who is addressed in the following verse:

"For with you is the source of Life; By Light from you we can see light" - Psalm 36:9

Acknowledgements

There is something very important that is technically omitted in this thesis - the love, care and support I received from others during this project! Below I will try, as much as my imperfect memory allows me, to remember them all.

Just over five years ago, I called up my friend, Dr. Tosin Famakinwa, and asked about taking up a PhD program in Japan. He introduced me to the student support staff, Ms Katy Niwa, who kindly introduced me to my PhD advisor, Professor Osamu Hanaizumi. After series of interviews with other professors, they recommended me to Monbukagakusho scholarship program. In the first year, my application was not granted, however, effort was made in the second year and the scholarship was awarded. It was great and exciting news for me and my family to hear. The four years we have been living in Japan has been the combined effort of people whose love and kindness are not affected by nationality, language or class. Therefore, I would like to take the time to heartily appreciate their help and support expressed in love to me and my family.

First of all I would like to thank my supervisors, Prof. Osamu Hanaizumi and Asso. Prof. Kenta Miura for their guidance during this project. I remember very well my first meeting with Prof. Hanaizumi. He told me that all the work in his laboratory are governed by Maxwell's Equation! This was like the Newton's first law - a push that gave me motivation in the beginning of this project. Furthermore, Prof. Hanaizumi is not just a Professor, but also a good and caring family head who understands very well what it means to balance family life and secular work. I heartily appreciate the understanding and enormous support I received from him throughout this project.

I still remember the time arrived at Narita airport and there was Prof. Miura waiting to take me to Gunma University which I appreciated very much. He has been giving many support and advices and corrections throughout the project. He gave me the first introduction into the research activities in Hanaizumi laboratory. I learned many things from him, such as paying attention to details. I admire his simple way of life and diligence at work. I was very happy when he was promoted to a Professor in Gunma University.

I've been happily working for Prof. Hanaizumi and Asso. Prof. Miura since four years. Their approach to science will always be indelibly imprinted on my own career. I am grateful to acknowledge their superb mentorship and guidance over the years. Even on their busiest days, I have never seen them turn away a student needing answers, advice, or experiment checking.

One of the advantages of working for Prof. Hanaizumi has been the excellent group of fellow students that I have had the pleasure to work with in his lab. In particular, I have worked with Masashi Honmi, Shin-ya Kawashiri, and Teruyoshi Shinagawa. They have contributed directly to this thesis through their work on Si-ion implantation and nanocrystal characterization. I appreciate very well their endurance especially during fabrication and characterization of photonic crystal waveguides. It was really hard time to focus light into the waveguide! I also have a great admiration for those in the group that have devoted their time to alternative energy research-solar cells, liquid crystals and other optical devices. I also enjoyed working with Dr. Mayank Kumar (former PhD student in our laboratory and Monbukagakusho fellow) and his wife Seema for their encouragement and meaningful conversations we had together. I would also like to acknowledge several other students that I meet in Hanaizumi lab and in the engineering faculty, Gunma University, the Tuesday launchers (formerly Friday launchers) for all the friendly conversation we had together.

I will not forget the love and understanding that I and my family received from Ms Katy Niwa right from the time we started the first application in Nigeria till now. It will be difficult for me to use the word "especially" here

because there are uncountable kindness she has shown to us, her diligent work that contributed to awarding the scholarship, her mother's love and understanding she employed actively that contributed to the quick issuance of my family's COE due to my wife's pregnancy then and also in obtaining quick alien registration and health insurance that saved us from the huge amount of hospital bill after delivery, her continuous encouragement and cheerful smiles even when she is too busy, she still found time for us. There is so much to say about her but I want her to know that she is remembered very well!

A friend in need is a friend indeed! Many of my friends have directly and indirectly supported me in this project. I want to appreciate the steady and encouraging effort I received from Dr. Tosin Famakinwa, who also was a former Monbukagakusho fellow before moving to Australia. As a Christian brother, he also helped me to maintain my spirituality while caring for other things. Some friends are also neighbors! I appreciate so much my good neighbor, Dr. Jaspal Bange (postdoctoral fellow with ATEC Gunma University) for his humility and honest effort to support and make others happy including me. The matured way he responds to his duty and the willingness to give necessary support, providing assistance and attentive listening and excellent suggestions are all remembered. During my trying period, he was always available to give necessary support and encouragement. I also appreciate very much the time he spent with me day and night reviewing my thesis till its final printing.

I also want to thank and acknowledge my thesis examination committee: Professors Osamu Hanaizumi, Masahisa Itoh, Kazumasu Takada, Kuniyuki Motojima, and Kenta Miura for the time and energy they spent in assessing my thesis and for the motivating questions I received from them during the examinations. I want to thank the staff of the electronic and computer engineering department. Recently I came to know Dr. Tomoyuki Sasaki now in Hanaizumi lab and I admire his gentle and mild effort in helping the new students and translating for me the document procedures for PhD graduates. My apologies to those that I am undoubtedly forgetting.

Additionally, I want to acknowledge the members of the student's support section for their endearing effort in making my study easier without much stress. I am particularly grateful to Ms Miyoshi from the head office in Maebashi, especially for those sleepless nights when she was trying to obtain COE for my family; to Ms Maruoka Emi for those bicycles she arranged for our children; to those I am not able to mention or have retired from their post or transferred to another office, I and my family will always remember you all! The timely and willing assistance I received from Ms Barbara at the Kiryu City office should not go unnoticed! I appreciate them very much.

One of the problems for foreign nationals in Japan is the Japanese language ability! According to research, language means more than the spoken words; it involves the understanding of the culture behind the spoken words. In this regards, I want to appreciate the kind training I received from my Japanese language teachers, their efforts were amazing. Though I am not too good in spoken Japanese, however, I have learned to understand Japanese feeling and thus can easily communicate with Japanese using few spoken words.

I am also appreciative of the financial support I received through a Japanese Government (Monbukagakusho) fellowship. I thank all the staff of this office for their diligent work in making sure that my allowances were paid on time.

I'm happy to have made too many friends in my years at Gunma University to list here. I will only say that I have had a great time and that although the time has come for me to graduate, I am in no hurry to leave.

I also want to acknowledge my former colleagues in VOIX Networks Limited; my former classmate and lecturers in Magnitogorsk Government Technical University, Russia; especially my former supervisor, Professor Alexander Nikolaevitch Panov, who also gave me similar trust and motivation during my Master's program as did Professor Hanaizumi in this PhD project. Also I appreciate the kind suggestions and encouragement I received from Professor Charles Ume of Geogia Tech. USA.

My appreciation also goes to my Japanese Christian brothers and sisters who have been a source of encouragement to me and my family.

Finally, I want to deeply appreciate my immediate and extended family members for all their support and encouragement over the years; my late father, Engineer Emmanuel Ogbuju Umenyi for his love and earnest desire to give us higher training; and my Mother, Roseline, for her motherly love and care. I also extend my appreciation to my brother and sisters in Nigeria for all their love and encouragements. I want them to know that they are very dear to me.

There is a natural combination that makes children grow well in the family. One is the Father's masculine quality and the other is the Mother's loving care. My lovely wife, Zareta, deserves my continuous care and love for her endless love, enduring qualities, and active support in training and bringing up our four children, Mariam, Michael, Hannah and Joanna. Additionally, I appreciate our children's endurance and obedience which had made it easier to balance the family life and other activities. Without their loving support, it would have been very difficult to complete this program. I want them to know that I love them all!

Umenyi Amarachukwu Valentine
September 2010
Gunma University, Kiryu, Japan.

Contents

List of Figures

LIST OF FIGURES

List of Tables

Chapter 1

Introduction

In this chapter we will try to explain the motivation and objectives of this work. These include the areas of importance in this research and what contribution our work is making towards the general goal. Finally, we will give the outline of the thesis chapter by chapter.

1.1 Silicon-based Photonics

Silicon-based photonic crystal is the study and application of photonic crystals that uses silicon as an optical medium. Silicon is unquestionably the most important material in the microelectronics industry. Its excellent electronic properties, studied for more than half a century, the abundance on earth, low cost, and its stable oxide, make it a natural choice for realizing integrated electronic circuits.

1.1.1 Motivation

The performance of electronic devices and their cost have been greatly improved by down scaling the component on a chip to a minimum feature size, making it possible to have more than 10^8 transistors on a single chip. As the integration of electronic components grow, i.e., device dimensions decrease to even smaller sizes, so does the need for low power, low cost, and high-speed devices, i.e., new miniaturization strategies are sought. In 1965, Gordon Moore predicted that the number of transistors incorporated in a chip will double every 24 months, [1] and, forty years later, device dimensions continue to scale down accordingly (see Fig. 1.1). In addition to enabling the conveniences afforded to us by today's microelectronic devices, such as wireless phones and

personal computers, this miniaturization of electronics has led to improved speed and performance, as well as to lower power consumption.

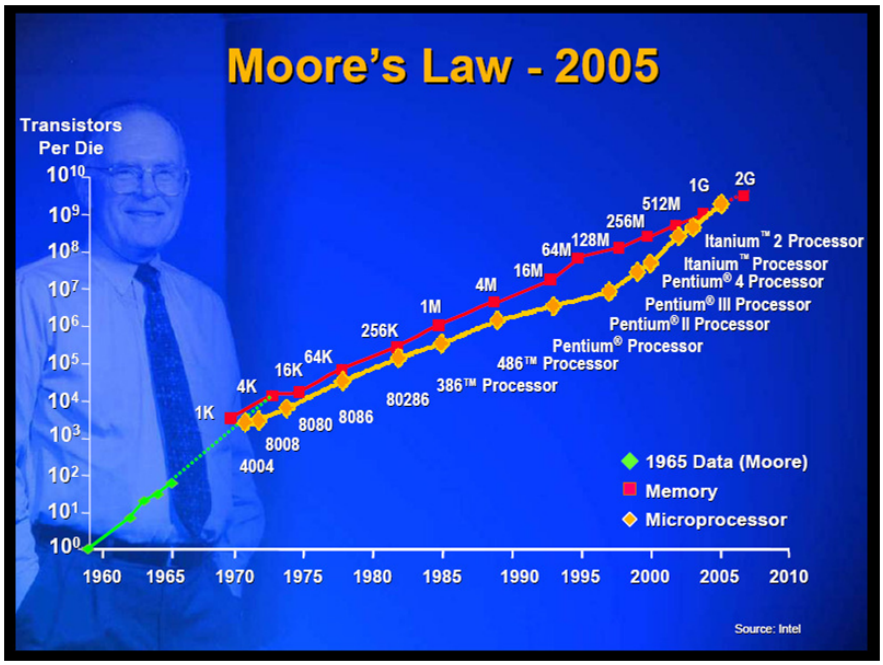

Figure 1.1: The Gordon Moore prediction - that the number of transistors incorporated in a chip will double every 24 months.

However, the scaling down of features introduces signal propagation delay between the different parts of a chip due to the tighter packing of the interconnections. It is believed that the propagation time delay will reach the actual computation delay, making it the limiting factor of the performance of a chip. This problem is commonly referred to as the interconnect bottleneck, and using photons instead of electrons for the communication on a chip could be a solution [2]. For this reason, a lot of effort has been made in the field of silicon photonics to achieve the monolithic integration of optical components on CMOS-compatible silicon chips. This brings great challenges to overcome, since silicon is a poor optically active material due to its indirect band gap.

Recent breakthroughs in the study of the optical properties of silicon have paved the way for the production of fully compatible silicon devices. One of the most significant advances was the observation of light emission from porous silicon [3] and silicon nanocrystals [4, 5, 6], which boosted the field of silicon photonics, as previously light emission was generally restricted to III-V-based compounds, which are expensive and

often incompatible with silicon. More recently, the Raman effect was exploited to achieve lasing in silicon [7], and modulation of light in silicon [8] and low loss silicon passive components [9] have been demonstrated. All these interesting results show silicon from another perspective and make it a very attractive material for electro-optic integrated circuits.

One area in the rapidly growing field of silicon photonics is that of light emitting nanocrystals. By scaling down a semiconductor crystal to a few nanometers, one can change the electronic properties of the semiconductors. The engineering of the bandgap can transform indirect bandgap material into potential light-emitters [4, 5]. It has also been shown that silicon nanocrystals can be obtained in a SiO_2 matrix, which is fully compatible with silicon-based platforms [4].

Another area of silicon photonics that has attracted attention lately is that of photonic crystal components as well as their numerical modeling. Photonic crystals [10, 11, 12] are periodic structures with periods of the order of the wavelength of the light and a very high refractive index contrast within each period [13, 14]. For telecommunications, where infrared light with wavelengths in the range 1.3μm to 1.6μm are used, the photonic crystal period is typically 0.7 μm or less. The periodicity can extend in 1-, 2- or 3-dimensions. Because of this high refractive index contrast, light will be scattered very strongly throughout the structure, and the scattered waves from each period can either add up or cancel out each other, depending on the wavelength of the light. The most complex, and also the most interesting photonic crystals have a periodic nature in all 3 dimensions. For a well-chosen geometry and a unit cell with sufficiently high refractive index contrast the scattering from each cell can interfere in such a way that all light inside the crystal within a certain wavelength range is cancelled out, so no propagation is possible in the structure [10]. This wavelength range is called a photonic bandgap (PBG). The PBG makes it possible to control the flow of light in a structure. For instance, one could fashion a waveguide enclosed in a 3-D photonic crystal. This waveguide could have very sharp bands, because the photonic crystal forbids the propagation of light outside the waveguides. Light is therefore forced to follow the path of the waveguide. Similarly, one could trap light in a cavity enclosed by 3-D photonic crystal. Although 3-D photonic crystals can control light in all directions, they are very difficult to fabricate for optical and infrared wavelengths. Their 3-D nature requires a very accurate stacking of elements with a high refractive index,

and to introduce deliberate defects to serve as e.g. waveguides or cavities is far from obvious. Consequently, many approaches utilizing 2-D photonic crystal structures have been proposed and demonstrated [15, 16].

An increased need for accurate models of the electromagnetic field behavior of photonic crystal structures are growing rapidly [17]. Their numerical methods of modeling have also experienced a lot of developments in the last few years [18, 19]. They provide a framework for quick low-cost feasibility studies and allow for design optimization before devices are fabricated. Furthermore, accurate computations can provide a detailed understanding of the complex physical phenomena inherent in photonic crystals. Therefore, we will also delve into numerical methods for photonic crystal modeling. Especially of interest is the finite-difference time-domain (FDTD) method, which we will use throughout the thesis for simulation and analyses of photonic crystals.

1.1.2 Objectives

The primary goals of this study are to obtain high quantum efficiency of light-emission from Si-nanocrystals and develop CMOS-compatible fabrication technique for novel photonic crystal devices as well as their numerical method. In practical, we will conduct the following research:

- Design, fabricate and assess a silicon light emitting material, i.e., silicon nanocrystals
- Develop, implement and analyze an FDTD based method for triangular lattice photonic crystals
- Design, fabricate and characterize silicon based photonic crystal waveguides utilizing Si-ion implantation and 2-D structures

1.2 Literature Survey

The literature survey is conducted based on the primary areas in this research and are summarized below.

Light emission from silicon:

- Si nanocrystals

- Fabrication methods
- Photoluminescence measurements

The details can be found in Chapter 2 of this thesis.

Numerical Modeling and Analyses:

- Methods
- Triangular lattice
- Photonic crystals
- Waveguides

The details can be found in Chapter 5 of this thesis.

Photonic Crystals:

- Principles
- Fabrication methods
- Characterization
- Applications

The details can be found in Chapter 4 of this thesis.

1.3 Organization of the thesis

The results presented in this thesis are related to the three subjects discussed in the previous section, namely, light emission from silicon, photonic crystals and their numerical modeling. Silicon nanocrystals are the focus of the second chapter of this thesis. In this chapter, the basic theory of the quantum confinement effect is described in order to understand the interesting features of nanocrystals, and also the potential applications of silicon nanocrystals. This will be followed by details of the fabrication and characterization of these structures. The third chapter deals with the ultraviolet light emission from fused-silica fabricated by Si-ion implantation and the results from the formation of silicon nanocrystals embedded in a SiO_2 matrix will also be presented. This includes a discussion of their optical properties and their potential applications.

The fourth chapter deals with photonic crystals. The fundamental science relating to this subject will be outlined, and overviews of the numerical modeling methods, fabrication and characterization techniques for these devices will be introduced. The unique dispersion properties of 2D photonic crystals and their application to waveguides will be discussed. The fifth chapter deals with the modified FDTD method for triangular lattice photonic crystals. The fundamental theory relating to this subject will be outlined, and details of the simulation techniques for photonic crystals will be introduced including the formulation and implementation of the method. The band diagram of a triangular lattice Photonic crystal for a given polarization of light and a given range of wavelengths, is calculated by a 2-D FDTD method using this approach and compared with that of 2-D plane wave expansion (PWE) method. The enhancement of the spectral peak identification will be shown. Also we investigate the convergence, accuracy, and stability of our approach and the deployment requirements.

The main ambition of this project was to bring those subjects together to develop a novel photonic crystal waveguides consisting of silicon-ion implanted silicon dioxide layers. The sixth chapter presents a detail design, analysis, fabrication and characterization of these novel structures. The possibility of prohibiting light propagation for certain directions with a photonic crystal can help in reaching this goal. By careful engineering of photonic band gap components to the wavelength of interest (λ=1.55 μm), the performance of these structures should be increased significantly. An FDTD method has been applied to optimize the optical transmission properties of several structures for transverse electric polarized light. The propagation of transverse electric polarized light through those structures has also been investigated experimentally, and will be presented.

Finally, in the seventh chapter, we give our conclusions and discuss future directions for research in these areas. It is hoped that the work presented in this thesis will motivate further research in this direction.

1.4 List of Publications included in this Thesis

The work conducted during this thesis has led to a number of publications in international refereed journals.

Journal Publications:

1. **A.V. Umenyi**, K. Miura, O. Hanaizumi, "Modified Finite-Difference Time-Domain Method for Triangular Lattice Photonic Crystals," IEEE J. Lightw. Technol., vol. 27, num. 22, pp.4995, Nov. 2009, (www.ieeexplorer.org).

2. **A.V. Umenyi**, M. Honmi, S. Kawashiri, K. Miura, O. Hanaizumi, S. Yamamoto, A. Inouye, M. Yoshikawa, "Ultra-Violet Light Emitting Fused-Silica Substrates Fabricated by Si-Ion Implantation, " Surface and Coatings Tech., (Under review).

3. **A.V. Umenyi**, S. Kawashiri, M. Honmi, T. Shinagawa, K. Miura, O. Hanaizumi, S. Yamamoto, A. Inouye, M. Yoshikawa, "Design and Fabrication of Novel Photonic Crystal Waveguides Consisting of Si-ion Implanted SiO2 Layers", Key Engineering Materials, 2010 (Accepted for publication).

4. **A.V. Umenyi**, S. Kawashiri, K. Miura, O. Hanaizumi, "Theoretical Analysis of Photonic Band Gaps and Defect Modes of Novel Photonic Crystal Waveguide Consisting of Si-Ion Implanted SiO2 using Finite-Difference Time-Domain Method, "Key Engineering Materials, 2010 (Under review).

The work was also presented at a number of (mostly international) conferences.

Conference Publications:

1. **A.V. Umenyi**, K. Miura, O. Hanaizumi, "Modified Finite-Difference Time-Domain Method for Triangular Lattice Photonic Crystals," IEICE Technical Report meeting, vol. 108, no. 370, OPE2008-137, pp. 5-10, Nov. 2008, Tokyo Japan.

2. **A.V. Umenyi**, K. Miura, O. Hanaizumi, "Simple Finite-Difference Time-Domain Method for Triangular Lattice Photonic Crystals," Opto-Electronic and Communication Conference (OECC) 14th International Conference July, 2009, Hong Kong. (IEEE conference proceedings, pp.1-2, (www.ieeexplorer.org))

3. **A.V. Umenyi**, K. Miura, O. Hanaizumi, "A New Approach to Simple and Easy FDTD Method for Triangular Lattice Photonic Crystals," The Japan Society of Applied Physics, 31pZN-15, March 2009, Japan. (Abstract book)

4. **A.V. Umenyi**, M. Honmi, S. Kawashiri, K. Miura, O. Hanaizumi, S. Yamamoto, A. Inouye, M. Yoshikawa, "UV and Visible Light Emitting Fused-Silica Substrates

Fabricated by Si-Ion Implantation," Surface Modification of Materials by Ion Beam technique 16th International Conference 2009, Tokyo Japan.

5. **A.V. Umenyi**, S. Kawashiri, K. Miura, O. Hanaizumi, "FDTD Analysis of Fused-Silica Substrates Fabricated by Si-ion Implantations for Photonic Crystal Devices," ISSS and AMDE 1st International Conference, Dec. 2009, Kiryu Japan.

6. S. Kawashiri, M. Honmi, **A.V. Umenyi**, T. Shinagawa, K. Miura, O. Hanaizumi, S. Yamamoto, A. Inouye, M. Yoshikawa, "Novel Photonic Crystal Waveguides Utilizing Si-ion Implantations," ISSS and AMDE 1st International Conference, Dec. 2009, Kiryu Japan.

7. **A.V. Umenyi**, M. Honmi, S. Kawashiri, T. Shinagawa, K. Miura, O. Hanaizumi, S. Yamamoto, A. Inouye, M. Yoshikawa, "Silicon Based Novel Photonic Crystal Waveguide Fabrication and Numerical Characterization by Si-Ion Implantation and FDTD Method," OECC2010 15th International Conference, July 2010 Sapporo Japan.

References

[1] G. E. Moore, Electronics 38, 114 (1965). 1

[2] Sematech, International Technology Roadmap for Semiconductors, 2005. 2

[3] L. T. Canham, Appl. Phys. Lett. 57, 1046 (1990) 2

[4] L. Pavesi, L.D. Negro, C. Mazzoleni, G. Franzo, F. Priolo, Nature 408 (2000) 440. 2, 3

[5] O. Hanaizumi, K. Ono, Y. Ogawa, Appl. Phys. Lett. 82 (2003) 538. 2, 3

[6] K. Miura, Y. Kato, H. Hoshino, and O. Hanaizumi, Thin Solid Films 516, 7732-7734 (2008). 2

[7] N. Koshida, H. Koyama, Appl. Phys. Lett. 60 (1992) 347. 3

[8] Z.H. Lu, D.J. Lockwood, J.-M. Baribeau, Nature 378 (1995) 258. 3

[9] Y. Yamada, T. Orii, I. Umezu, S. Takeyama, T. Yoshida, Jpn. J. Appl. Phys. 35 (1996) 1361. 3

[10] E. Yablonovitch: Phys. Rev. Lett. Vol. 58 (1987). p. 2059 3

[11] S. John: Phys. Rev. Lett. Vol. 58 (1987). p. 2486 3

[12] J. D. Joannopoulos R. D. Meade and J. N. Winn: *Photonic Crystals : Molding the flow of Light, Second edition* (Princeton NJ: Princeton University Press, 2008). 3

[13] O. Hanaizumi K. Ono Y. Ogawa and T. Matsumoto: Appl. Phys. Lett. Vol. 84 (2004). p. 3843 3

[14] N. Fukaya D. Oshaki and T. Baba: Jpn. J. Appl. Phys. Vol. 39 (2000). p. 2619 3

[15] M. Loncar T. Doll J. Vuckovic and A. Scherer: IEEE J. Lightw. Technol. Vol. 18 (2000). p. 1402 4

[16] A. Mekis J. C. Chen I. Kurland S. Fan P. R. Villeneuve and J. D. Joannopoulos: Phys. Rev. Let. Vol. 77 (1996). p. 3787 4

[17] A. Chutinan and S. Noda, waveguides and Waveguide bends in two-dimensional Photonic crystal slabs, *Phys. Rev. B, Condens. Matter*, vol. 62, no. 7, pp. 4488-4492, Aug. 2000. 4

[18] A. Taflove and S. C. Hagness, *Computational Electromagnetics: The finite-Difference Time-Domain Method*. Norwood, MA: Artech House, 2000. 4

[19] K. S. Yee, Numerical solution of initial boundary value problems involving Maxwell's equation in isotropic media, *IEEE Trans. Antennas Propag.*, vol. AP-14, no. 3, pp. 302-307, May 1966. 4

REFERENCES

Chapter 2

Silicon Nanocrystals and Ion Implantation

2.1 Introduction

In this chapter we will explain the fundamentals of the core material and method of this research: silicon nanocrystals and ion implantation. Silicon nanocrystals are low dimensional silicon. Therefore, we will briefly go over the light emission from silicon in the first section. additionally, we will then explain the fabrication and characterization methods as well as the quantum confinement effect model of nanocrystals and their emission properties. In the second section, detail principles of operation of ion implantation will be explained as well as their advantages in this work. To conclude this section, we briefly discuss the simulation tools that can be used to model ion implantation technique.

2.2 Silicon Nanocrystals

2.2.1 Light emission from Silicon

Silicon is the most prevalent material in the electronics world, not only because of its abundance and low cost, but also because it has a high-quality, stable oxide that provides excellent electronic passivation. However, due to its indirect band gap, the electronic structure of silicon prevents this material from being a strong light emitter. In indirect band gap semiconductors like silicon, there is a mismatch in momentum space between the electron and hole states (see Fig. 2.1). To conserve momentum, excitation and relaxation between the conduction band and valence band extrema require the assistance of a crystal lattice vibration. Radiative recombination of excited charge

carriers is therefore a three-body process, and, as a result, it is much less efficient than the analogous two-body recombination in a direct band gap semiconductor, where the conduction and valence band extrema are matched in momentum space. The low probability of radiative recombination in indirect band gap materials favors non-radiative decay processes, and excited electrons generally lose energy as heat, not emitted photons. These materials exhibit only very faint luminescence, even at low temperatures, and this weakness has traditionally prevented the desirable extension of silicon microelectronics to silicon optoelectronics; LEDs and lasers cannot be produced from bulk silicon.

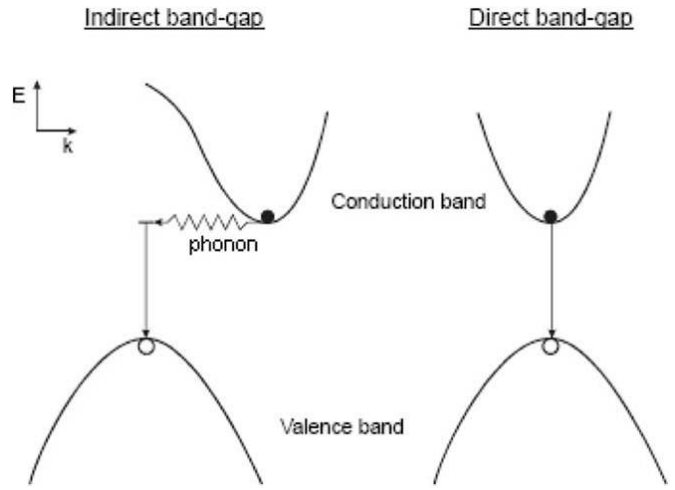

Figure 2.1: The illustration of indirect and direct bandgap - silicon as an indirect bandgap cannot emit light due to mismatch in momentum space between electron and hole states.

Hope for using silicon as a light emitter was resurrected in 1990, when Canham discovered that porous silicon, which has nanometer-scale features, exhibits efficient room-temperature photoluminescence at visible energies above the bulk Si band gap of 1.12 eV [1, 2]. Here, photoluminescence (PL) refers to the emission of a photon upon the relaxation of an electron-hole pair (exciton) that has been excited by some external light source. The relaxation energy of the charge carriers is determined by the energy difference between the conduction and valence bands.

Since the discovery of room-temperature PL from porous silicon, considerable effort has been devoted to the development of silicon nanostructure-based light emission sources. The luminescence of Si nanocrystals has been studied in various systems,

from single nanocrystals [3, 4] to multilayered structures, [5]. Photoluminescent silicon nanostructures have been fabricated by many methods, including porous etching [1], implantation of Si+ ions [3, 6, 7], rf co-sputtering of Si and SiO_2 [4], Laser Ablation Deposition [8], Self-assembling Growth [9, 10], Flame Hydrolysis Deposition [11], and Plasma Enhanced chemical vapor deposition of silicon suboxides [12, 13]. We will explore these methods in the subsection below.

An alternative to developing integration methods for traditional optical materials is to attempt to exploit quantum mechanical effects to improve the optical properties of silicon or other currently CMOS compatible materials. Following this approach, nanostructured silicon has been identified for many years as a promising candidate material for silicon photonics.

2.2.2 An Overview of different Fabrication Methods

The fabrication of Si-based nanomaterials with high quality is very important in order to obtain efficient and stable luminescence. Thus far, various growth technologies have been developed, and are being successfully used for the formation of Si-based nanostructures. Silicon nanocrystals can be fabricated through a variety of techniques as mentioned in the previous subsection and all of those methods rely on the low mobility of silicon in silicon dioxide [14] and the equilibrium phase separation of Si from SiO_2 in silicon-rich oxide layers at high temperatures [15]. However, whatever method is used, it is much more important that both growth mechanism and process parameter must meet the needs of the formation of the expected nanostructure. Following is an overview of these methods and at the end we summarize by choosing the fabrication method for this work and give some reasons for our choice.

Plasma Enhanced Chemical Vapor Deposition (PECVD)

PECVD is one of the main techniques to fabricate Si-based nanomaterials, which are deposited by glow-discharge decomposition of reactive gas mixtures at the high vacuum growth system, whereas it should be noted that this method is divided into the following two process approaches, i.e. the direct deposited formation and the predisposition plus postannealing formation. PECVD has largely replaced low pressure chemical vapor deposition (LPCVD) for SiO_2 and other film depositions because it provides higher deposition rates and good step coverage, low deposition temperature is less prone to

particle contamination and has a number of other advantages that make it one of the most important technologies for the deposition of amorphous thin films. Initiation of chemical processes with the help of electric discharge producing ions and radical species was known for a long time. In 1963 Atl et al. [16] showed that the PECVD process could be used for microelectronic applications. The method was primarily used for diffusion masks and passivation. More common applications of this process for microelectronic fabrication started with the introduction of commercial processing equipment in 1974. In recent years, new material demands and lower-processing-temperature requirements in ULSI circuits, solar energy cells, flat-panel displays, and optoelectronic integrated systems have made plasma-enhanced deposition processes increasingly important.

One of the major advantages of plasma deposition processing for optical integration besides it's high deposition rate is it's flexibility for depositing films with desirable properties. Films with unique composition and given physical and chemical properties can be obtained by adjusting deposition parameters such as temperature, rf power, pressure, precursors gas mixture and their ratio. Although the deposition is at relatively low temperatures, to achieve low loss material high temperature annealing is commonly applied. Mechanically and chemically stable thick films can be deposited and easily formed into channel waveguides and waveguide components by plasma etching. The deposition rates can be in the range of 0.15 - 0.3 mm/min and the optical quality of the obtained films is usually very good giving optical losses of 0.1 dB/cm and below.

Si-Ion Implantation

Ion implantation is a technique with which ions can be introduced at a well-defined depth and concentration into any material, in a reproducible fashion. In the ion implantation procedure, ions are extracted from a plasma and accelerated by an electric field to the sample. The ions impact with sufficient energy to travel some distance into the sample before they come to rest. The total dose of implanted ions is controlled by monitoring the integrated current as the ion beam is rastered over the sample. In this way an implanted layer can be created with good uniformity across large substrates. Usually, the ion implantation is used for the fabrication of shallow junction semiconductor devices, while recently, the Si nanocrystalline can also be obtained using Si ions with higher energy and larger dose implanted into silica glass, the quartz or thermally

grown SiO_2 layer, followed by annealing treatment. At the same time, the Si concentrations, implanted depth and average size in the samples can be controlled by controlling the implanted dose and energy of the Si ions, as well as the annealing temperature.

Iwayama et al. [7] reported the implantation of Si ions into silica glass in order to form the Si nanopariticles. Si ions have an energy of 1 MeV and a dose of (1-4) 10^{17} ions/cm^2. The Si precipitates develop around a depth of 1.5 mm, and the sizes of the Si nanopariticles are 1.5-2.0 nm after annealing at 1100^{o}C. More recently, low-dimensional Si nanocrystals have been produced by negative ion implantation (80 keV, 1×10^{17} ions/cm^2) into ultra-pure quartz or into thermal grown silicon dioxide layers on substrates, followed by high-temperature thermal annealing at 1100^{o}C for 1 h [3, 6]. Transmission electron micrograph (TEM) showed that the Si nanocrystals are embedded within the oxide matrix. Their sizes, effective refractive index and optical filling factors were ≈3 nm in diameter, 1.89% and 1.17%, respectively. Miura et. al. [6] reported the fabrication of Si-nc including fused-silica substrates by using the Si-ion implantation and annealing, and evaluated their PL properties. As a result, they found a blue-light emission band in addition to the longer wavelength band reported by Pavesi et al. [3] They observed PL peaks around a wavelength of 400 nm from their samples after annealing and succeeded in increasing the blue PL peak intensity to over four times higher than the longer wavelength peak by annealing at 1200 ^{o}C.

Laser Ablation Deposition

Laser ablation has various applications in fundamental studies of physics, chemistry and technological fields. In practice, the pulsedlaser deposition of materials by laser ablation has been widely used for the making of thin films. Nowadays, the pulsed-laser ablation has been successfully applied to fabrication of Si ultrafine particles. This method has such main advantages as rapid thermogenic speed, higher Si particle concentration and small surface contamination, etc.

Werwa et al.[8] reported the preparation of the nanometer sized crystallites of silicon in the He carrier gas by a pulsed Nd: YAG laser ablation supersonic expansion technique. HREM is used to verify that particles with diameter are in the range of ≈3 nm. In order to achieve a more uniform size distribution of Si nanocrystallites, the ablated deposition of nc-Si: Er thin films has been carried out by Zhao et al.[17]. The films were obtained by a twostep process, in which the a-Si:Er films were prepared by

ablating polycrystalline Si: Er targets, and were followed by annealing temperatures from 500 to 1000^{o}C. The average crystallite size in the nc-Si: Er was ≈6 nm. The study of dynamics on laser ablation deposition is very important for the fabrication of Si nanocrystallites with high quality. Yoshida et al.[18] have presented an inertial fluid model to explain the deposited dynamic of Si nanocrystallites. In this model, it can be found that the dissipated kinetic energy, namely the cohesive energy of as-formed ultrafine crystallite, is proportional to the inert gas ambient pressure. Therefore, the average size of Si ultrafine particles can be controlled by changing the pressure of inert gas. Furthermore, Lee et al.[19] investigated the Nd: YAG laser-induced breakdown of 20 mm glass microspheres using time-resolved optical shadow images and Schlieren images, and developed a numerical model that simulated the breakdown process in the glass microsphere. The result indicates that the agreement between the experimental shockwave velocity and the simulation was good, i.e. the model is sound.

Self-assembling Growth

The self-assembling growth is a new technique developed in the last few years in order to form nanoscale semiconductor quantum dots. It should be pointed out that when this method is adopted, the creation of energy-preferred nucleation sites on the solid state surface is very important. Nakagawa et al.[9] reported the self-assembling growth of Si nanoquantum dots on ultrathin SiO_2 layer by controlling the early stages of the SiH_4 gas LPCVD. It has been suggested that the thermal dissociation of surface Si-O bond plays a key role in creation of nucleation sites on as-grown SiO_2 surface. To obtain the formation of Si nanoquantum dots with much higher density and smaller size, Miyazaki et al.[10] have grown hemispherical Si nanoquantum dots on Si-OH bonds on terminated SiO_2 surface, which also prepared slightly etched back in a 0.1%HF solution or dipped in pure water. The measurements of Fourier transform infrared attenuated total reflection (FTIR-ATR) have confirmed that the 0.1%HF-treated SiO_2 surface has much higher nucleation density, and the activation energy is as low as 1.75 eV, so that the density of the Si nanoquantum dots is increased with Si-OH bonds density. In addition, Yasuda et al.[20] showed that chemically active sites on SiO_2 surface can be either passivated or introduced intentionally by treating them in a proper chlorosilane gas, $SiHnCl_{4-n}$ (n = 0, 1, 2), and the SiH_2Cl_2 treatment is found to enhance Si nucleation greatly, the nucleation density reaches $1.8\times10^{11}/cm^2$. They have also fabricated Si nanoquantum

dots by LPCVD decomposition of Si_2H_6 gas. The technical feature of this method is compatible with oxidation, annealing and doping, and is suitable for the formation of Si nanoquantum dots on large area substrate.

Sputtering

In sputtering deposition glass molecules can be sputtered from a target by means of electron or ion bombardment, as well as rf-power. Hanaizumi et. al. [4] reported the observation of blue light emission from a Si:SiO_2 co-sputtered film without annealing, which was observed by naked eye with small optical gain ($\approx$1.3 cm^{-1}). Miura et. al. [5] reported the fabrication Si/SiO_2 multilayered films having nanometer-order-thick Si and SiO_2 layers by using radiofrequency (rf) magnetron sputtering and subsequently annealed the samples at high temperatures (from 1150 to 1250 ^oC). They observed UV photoluminescence having a sharp peak at a wavelength of around 370 nm from a sample annealed at 1200 ^oC.

In one of the earlier papers describing the formation of channel waveguides [21] the authors used RF power applied both to the substrate and to the target. This method (bias sputtering method) allows filling small trenches or gaps between the waveguides otherwise difficult to fill during sputtering. In conventional sputtering the sputtered glass is deposited upon the grooves, but the grooves remain unfilled since overhangs can easily close them up. The glass composition is limited by the available targets. In order to obtain a core with a high refractive index, pure silica can be used as a target, since the refractive index of sputtered silica is higher than that of bulk material by about 0.5 percent. The refractive-index difference depends on the RF power applied. Typical sputtering rate is quite low, approximately 1 mm/h. Usually the deposited glass is of poor quality leading to high propagation loss of order 1 dB/cm.

Flame Hydrolysis Deposition (FHD)

Flame hydrolysis (FHD) is mainly a technology for the fabrication of optical fiber preforms. It was adopted for the production of planar devices for optical communication in 1990 [11] and is now commonly used for the deposition of glass on silicon for integrated optical circuits such as star couplers, splitters, Mach-Zehnder interferometers and Arrayed waveguide gratings. The first step of the process is to deposit two successive glass particle layers as the undercladding (called also buffer) and core on a Si

substrate (alternatively one layer above a thermally oxidized silicon wafer) by the flame hydrolysis of $SiCl_4$. This process leads to the deposition of a soot of silica (SiO_2) that for the core layer can be doped by the inclusion of GeO_2, P_2O_5, and B_2O_3, all from their respective halide gases. After sintering of the soot at 1200-1350^{o}C, glasses of different refractive indices can be obtained. The desired core ridges for the channel waveguides are then defined by photolithography followed by reactive ion etching. The obtained pattern is finally covered with an overcladding (top) layer in another FHD process. Deposition of sequential layers of silica with differing refractive indices leads to the microfabrication of buried optical waveguide structures. The deposition is relatively fast (several mm/min), glass composition can be widely changed by co-deposition of different precursors, although this composition can be changed both physically and chemically during the consolidation process. The optical quality of the obtained film is very good and optical losses are very low.

Summary

Though each system has unique advantages and disadvantages, the ion implantation method, which creates a Gaussian profile of excess Si in a SiO_2 substrate that is subsequently annealed to nucleate and grow nanocrystals, is a fully CMOS-compatible procedure. We therefore choose to work on silicon nanocrystals produced by ion implantation in order to explore the optoelectronics of this easily integratable system. This technique was selected primarily for compatibility with CMOS processing; ion implantation is already commonly used in silicon microelectronics to create doped regions in circuits. Low loss waveguides can be achieved using ion implantation by utilizing its gentle refractive index distribution. The refractive index and its depth can be controlled by changing the implantation dose and energy. The total dose of implanted ions is controlled by monitoring the integrated current as the ion beam is rastered over the sample. In this way an implanted layer can be created with good uniformity across large substrates. Ion implantation is available as a collaboration service with Japan Atomic Energy Agency. In the next section, we will discuss the characteristics of ion implantation technique, which will be used throughout the thesis.

2.2.3 Photoluminescence Measurement

Photoluminescence (PL) is the optical radiation emitted by a semiconducting crystal after excitation with incident light source (usually a laser). Most of the light results from the difference in energy of the excited electron (in the conduction energy band) returning to its ground state (valence energy band). At low temperatures (4-77K) the excited electrons return to their initial energy through more complex mechanisms involving mainly point (0-D) defects and interactions with the vibrational energy states (phonons) of the crystal. The PL spectra have narrow bands (peaks) which make analysis possible. The PL is a complementary technique to the absorption spectra. The emission spectrum contains fingerprint-type peaks related to the energy of each excited level and can be used as a sensitive probe to find impurities and other defects in semiconductors. Fig. 2.2 shows a typical PL measurement setup.

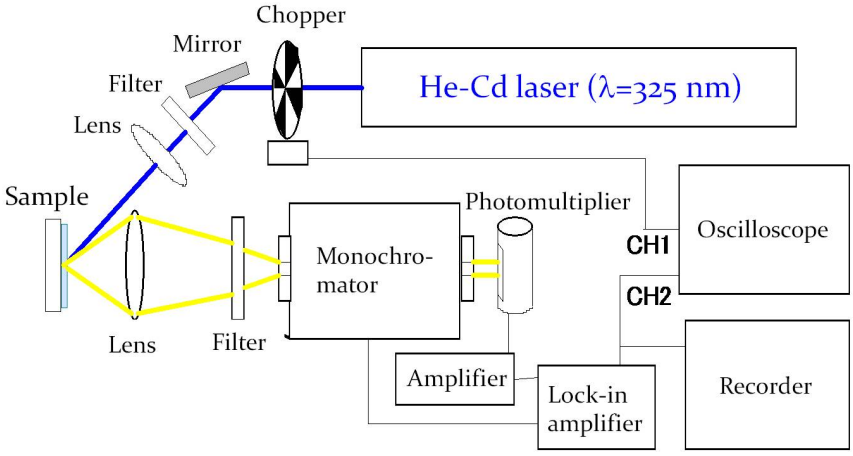

Figure 2.2: The schematic of PL measurement setup - the He-Cd laser (Kimmon IK3251R-F) with a wavelength of λ=325 nm is used.

To excite the nanocrystals, the He-Cd laser (Kimmon IK3251R-F) with a wavelength of λ=325 nm is used. The light is passed through chopper and detected by the monochromator (Nikon P250), photomultiplier tube (Hamamatsu R3896), and lock-in amplifier (NF LI-572B).

2.2.4 Structural Characteristics

Si-based nanocrystalline material is a low dimensional small quantum system with complex structure formations. When the size of Si-nc decreases due to a low Si content

in the deposited film or to allow annealing temperature treatments, the emission band shifts to the blue. On the contrary for high Si content in the film or high annealing temperature the emission band shows a red shift. The exact origin of the emission is not clear. Certainly the reduced dimensionality effect in Si crystal plays a crucial role. However, as the PL characteristics are determined by both the quantum confinement and surface passivation, the role of the surface cannot be neglected. As shown in Fig. 2.3, the structure of the Si-nc is formed by three layered structures: the central region made of amorphous or Si nanocrystallites, the interface region made of substoichiometric and stressed silica and the surface for the amorphous or Si nanocrystallines embedded in SiO_2 or SiO_x films.

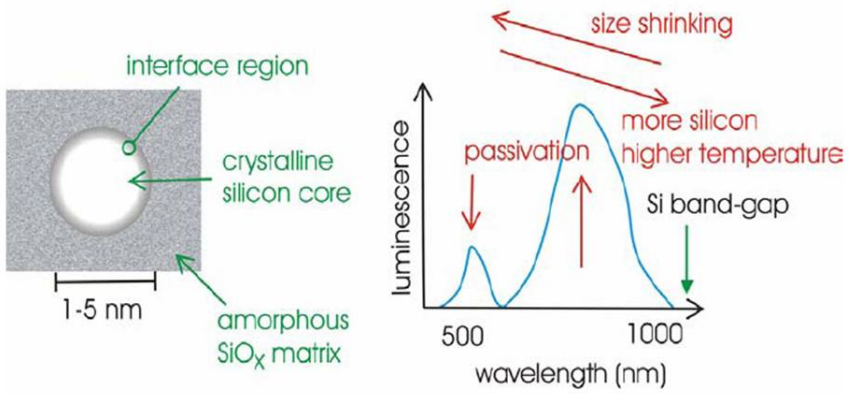

Figure 2.3: The schematic structure of Si-based nanocrystalline material - embedded in SiO_2 or SiO_x films.

The study indicates that their luminescent properties are dependent directly on the structural characterization. Therefore, in order to deepen knowledge for the luminescent properties, an important question is to clarify the structural characterizations of these materials. In this section, we will analyze their microstructures by means of various measuring methods.

Si nanocrystallites

The size and distribution of Si nanocrystallites are important structural parameters, which dominate the quantum confined effect (QCE)-based luminescence of Si nanocrystallines. They can be controlled by various technical parameters, such as substrate temperature, energy-carried beam intensity, gas flow ratio, reactive gas pressure, annealing

temperature, etc. The size and distribution are related both to the Si atomic content and to the annealing temperature for the Si nanocrystallites embedded in SiO_2 or SiO_x matrix, and the size and numbers of the Si nanocrystallites are increasing with Si atomic content and annealing temperature. Zhu et al.[22] studied the correlation between size of Si nanocrystallites and annealing temperature, and the result indicates that the sizes of Si nanocrystallites were rapidly increased with the annealing temperature increasing at a certain Si atomic concentration. For instance, the average sizes of Si nanocrystallites are 3 and 6 nm when annealing temperatures are 1000 and 1100 ^{o}C, respectively. In addition, annealing temperature and the Si atomic content in the SiO_x matrix also have observable influence for the size of Si nanocrystallites. The study found that the size of Si nanocrystallites was reduced with Si atomic content increasing [23]. For example, the average sizes of Si nanocrystallites in the $SiO_{1.30}$ and $Si_{1.65}$ films are 3.4 and 2.7 nm at the annealing temperature of 1100 ^{o}C, respectively. The Si crystallites have a spherical or, occasionally ellipsoidal shape, and are uniformly dispersed in the films. Iacona et al.[24] reported a detailed study of correlation between luminescence and structural properties of Si nanocrystals, the result confirmed that when annealing temperatures were increased from 1100 to 1250 ^{o}C, the sizes of Si nanocrystallites were increased from 1.0 to 2.1 nm at the Si atomic concentration 44%, while the sizes of Si nanocrystallites were increased from 1.1 to 1.7 nm when Si atomic concentrations increased from 37% to 44% at annealing temperature of 1250 ^{o}C. Except for annealing temperature, annealing time can also affect the size of Si nanocrystallites. In general, the sizes of Si nanocrystallites are increased with the annealing time increasing.

In contrast, for the Si nanocrystallites to cope with a thin SiO_2 layer, the size of Si nanocrystallites is reduced as increasing the annealed temperature. Hirano et al.[25] found that the sizes of the self-assembling grown Si nanoquantum dots were reduced from 1.3 to 0.8 nm when the samples were annealed in N_2 ambient at the temperature of 1000 ^{o}C. This is due to O_2 molecules incorporated to Si nanoquantum.

Oxygen-related defect

The oxygen-related defect plays an important part in the luminescent properties of Si-based nanocrystallines. Usually, this defect can be classified into two main formations, i.e. the nonbridging oxygen hole center (NBOHC) created in the glassy SiO_2 or SiO_x and the localized state formed at the Si/SiO_2 interface. Previous works indicate that

both 4.8 and 2.0 eV optical absorption bands and 1.9 eV PL band are caused by NBOHC generated in high-purity silica glasses which are subjected to g-rays or other forms of radiation. Other oxygen-related defect is localized states which exist in the interface region of the Si nanocrystallite/SiO_2(SiO_x) or the Si/SiO_2 superlattice. The generation of these defects is correlated by the enrichment of silicon and oxygen.

2.2.5 Luminescent Mechanism

In this subsection, we will discuss the luminescent properties of the various Si-based nanomaterials. In order to give a good understanding on the PL properties, it is necessary to know the luminescent mechanism. Up to now, a few models have been considered by many investigators, e.g. the quantum confined effect (QCE) model, the oxygen-related model defect and the quantum confined effect-luminescent center model. In this section, we will present a brief analysis of the luminescent properties based on the ranges of the luminescent wavelength, shift of peak energy, changes of luminescent intensity and structural characterization of the materials.

Quantum confined effect model

The first and more favorable explanation for the PL properties of nanometer sized Si crystallites is the QCE model. This model indicates that the PL properties result in Si nanocrystallites with nanoscale structures, which have quantum confinement actions for the photogenerated or electroinjected carriers. According to the view of the semiconductor physics, when the Si nanocrystallite size is reduced, the bandgap will become large, and create the quantum energy level in the conductor band and valence band. Then, the selection rule of indirect bandgap luminescence is not applicable to Si-based nanocrystallites due to the forfeit of translation symmetrization of periodic crystal. As a result, with the size of the Si nanocrystallites reduced, not only light emitting intensity is increased, but also peak energy is blue-shifted [6]. Fig. 2.4 shows the change of the bandgap energy and PL peak energy with the size of the Si nanocrystallite size.

Takagi et al.[26] studied the visible PL properties on Si microcrystallites embedded in a Si oxide matrix in 1990. They have confirmed that the luminescent energy depended on Si crystallite sizes ranging from 2.8 to 5.6 nm. The inverse relation between light emission energy and the square of the crystallite size indicates that the carrier confinement in the Si nanocrystallites causes this PL phenomenon. Moreover, Kanzawa

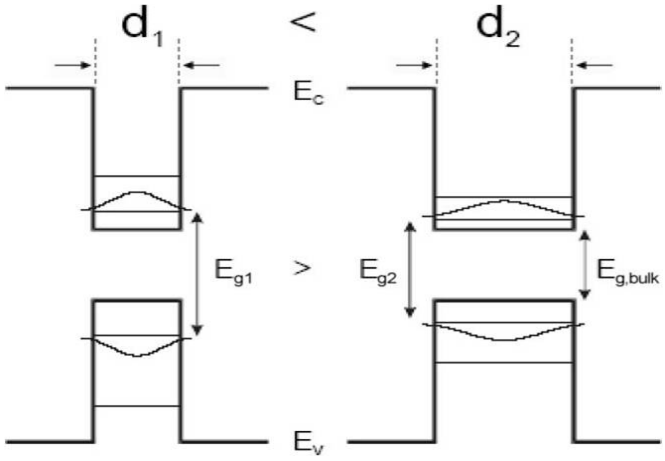

Figure 2.4: The illustration of quantum confinement effect - when the Si nanocrystallite size is reduced, the bandgap will become large, and create the quantum energy level in the conductor band and valence band.

et al.[27] also measured the PL spectra of Si nanocrystals embedded in SiO_2 films as a function of the size, and found that as the average particles size decreased from 3.8 to 2.7 nm, the PL peak energy exhibited a blue shift from 1.42 to 1.54 eV, and its peak intensity increased progressively. This strong size dependence of the PL peak energy suggests that the PL properties arise from the recombination of electrons and holes confined in the Si nanocrystals. More recently, strong room-temperature PL properties have been observed in high temperature annealed substoichiometric silicon oxide thin films prepared by PECVD [24]. The normalized room-temperature PL spectra shows that the wavelengths of the PL peak were increased from 770 to 880 nm with the annealing temperature increasing from 1100 to 1300^{o}C. This is because the size of the Si nanocrystallites might have enlarged when annealing temperature is increased. The dependence of the PL properties on the nanocrystallite size is in qualitative agreement with the carrier quantum confinement theory.

Oxygen-related defect model

Another important light-emitting phenomenon is the oxygen-related defect luminescence. However, it is worthwhile to be noted that this luminescence is different from that of the quantum confined effect-based luminescence, i.e. its properties are almost independent of the Si nanocrystallite size. The study pointed out that the defects in semiconductor materials can cause energy levels in its bandgap. The photogenerated

electrons are trapped in these energy levels, then transited to valence band, which accrues the combination with holes when the samples are excited by light energy. In this light emission process, the oxygen-related defects play the role in the luminescent centers. Among them, NBOHC is one of the most important light emitting defects.

Quantum confined effect-luminescent center model

This model indicates that the PL and EL properties of Si-based nanocrystalline materials are dependent not only on the Si nanocrystal size, but also on the oxygen-related defect. It should be noted that the defect center in this structure exists in the Si/SiO_2 interface region, it acts as a radiative recombination center.

2.3 Ion Implantation

Ion implantation is the process of depositing a chemical species into a substrate by direct bombardment of the substrate with high-energy ions of the chemical for deposition. Over the years, ion implant has steadily replaced thermal diffusion for doping a material in wafer fabrication because of its many advantages. The greatest advantage of ion implant over diffusion is its more precise control for depositing dopant atoms into the substrate. Doping, which is the primary purpose of ion implant, is used to alter the type and level of conductivity of semiconductor materials. It is used to form bases, emitters, and resistors in bipolar devices, as well as drains and sources in MOS devices. It is also used to dope polysilicon layers. During ion implantation, impurity atoms are vaporized and accelerated toward the silicon substrate. These high-energy atoms enter the crystal lattice and lose their energy by colliding with some silicon atoms before finally coming to rest at some depth (Fig. 2.5). Adjusting the acceleration energy controls the average depth of depositing the impurity atoms. Heat treatment is used to anneal or repair the crystal lattice disturbances caused by the atomic collisions.

2.3.1 The Principle of Operation

Ion implantation equipment (see Fig. 2.6) typically consists of an ion source, where ions of the desired element are produced, an accelerator, where the ions are electrostatically accelerated to a high energy, and a target chamber, where the ions impinge on a target, which is the material to be implanted. Thus ion implantation is a special case of particle radiation. Each ion is typically a single atom or molecule, and thus the actual amount

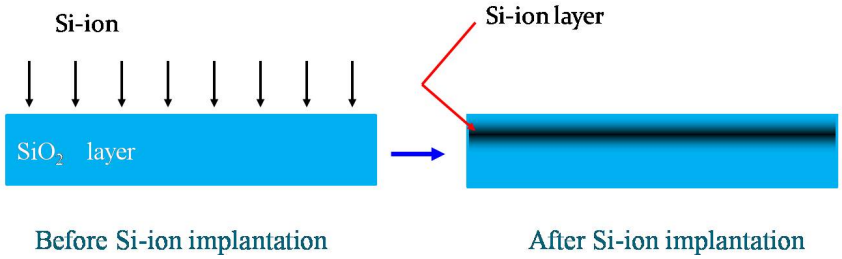

Figure 2.5: The schematic of ion implantation - a layer of Si-rich region is formed after implantation with subsequent thermal annealing.

of material implanted in the target is the integral over time of the ion current. This amount is called the dose. The currents supplied by implanters are typically small (microamperes), and thus the dose which can be implanted in a reasonable amount of time is small. Therefore, ion implantation finds application in cases where the amount of chemical change required is small.

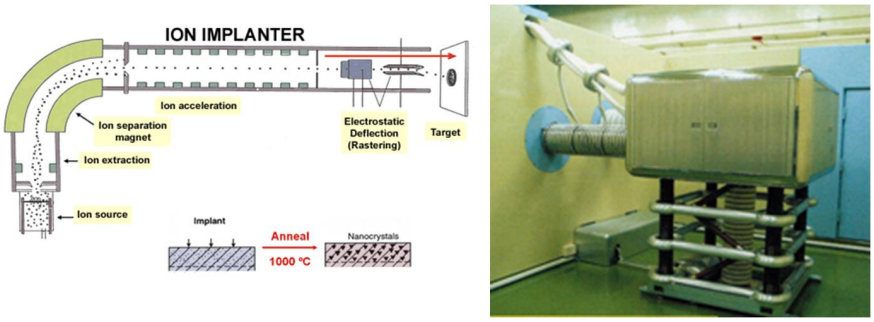

Figure 2.6: The schematic of ion implantation and the actual equipment - we are supported by Japan Atomic Energy Agency (JAEA) located at Takasaki Center for Advanced Radiation Research.

Typical ion energies are in the range of 10 to 500 keV (1,600 to 80,000 aJ). Energies in the range 1 to 10 keV (160 to 1,600 aJ) can be used, but result in a penetration of only a few nanometers or less. Energies lower than this result in very little damage to the target, and fall under the designation ion beam deposition. Higher energies can also be used: accelerators capable of 5 MeV (800,000 aJ) are common. However, there is often great structural damage to the target, and because the depth distribution is broad, the net composition change at any point in the target will be small. The energy of the ions, as well as the ion species and the composition of the target determine the depth of penetration of the ions in the solid: A monoenergetic ion beam will generally have a broad depth distribution. The average penetration depth is called the range of

the ions. Under typical circumstances ion ranges will be between 10 nanometers and 1 micrometer. Thus, ion implantation is especially useful in cases where the chemical or structural change is desired to be near the surface of the target. Ions gradually lose their energy as they travel through the solid, both from occasional collisions with target atoms (which cause abrupt energy transfers) and from a mild drag from overlap of electron orbitals, which is a continuous process. The loss of ion energy in the target is called stopping and can be simulated with the binary collision approximation method.

2.3.2 Post Implantation Annealing

Thermal annealing is an important postgrowth treatment necessary to be performed before proceeding to further processing. For some crystals, whether optical or electronic, strains develop during growth and can be reduced by thermal annealing. During thermal annealing where the crystals are heated at a particular rate to a particular temperature, kept there for a particular time duration and then slowly cooled down to room temperature. Thumb rule for thermal annealing is to anneal at a temperature 2/3 of the melting point (taken in degrees Kelvin) of the material. At this temperatures the defects (dislocations) become mobile and the crystal heals itself. Annealing can be done either in high vacuum or in the presence of inert atmosphere, i.e., in presence of argon or nitrogen atmosphere. Many of the useful crystals consist of more than one component, ie. compound crystals, for example, CdS, CdSe, GaAs, InP etc. In the cases where the vapor pressure of one of the component is higher compared to the other, a deficit of the more volatile component occurs. To prevent such deviations from the stoichiometric composition we anneal such crystals in an atmosphere containing an excess of the component having the higher vapor pressure. For example CdS can be annealed in sulfur atmosphere, GaAs can be annealed in As atmosphere.

Fig. 2.7 shows the actual picture (left) of annealing equipment used in this work and the schematic diagram (right). It consists of a siliconit furnace, thermocouple, and temperature controller. The controller is programmed for the maximum temperature and annealing time. The sample to be annealed is inserted inside siliconit tube with the thermocouple placed close to it. The operation of the equipment is then monitored through a camera to an attached TV monitor placed in our office.

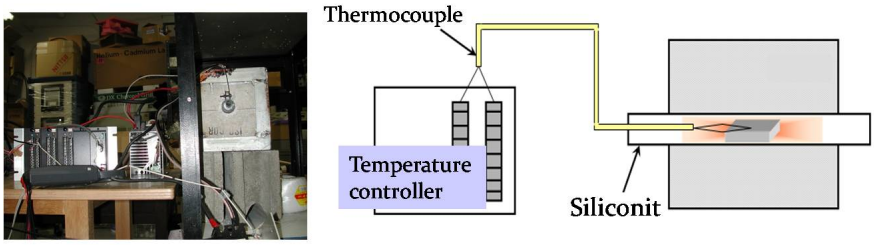

Figure 2.7: The actual picture of annealing equipment used in this work and the schematic diagram - It consists of a siliconit furnace and temperature controller.

2.3.3 Problems with Ion Implantation

Crystallographic Damage

Each individual ion produces many point defects in the target crystal on impact such as vacancies and interstitials. Vacancies are crystal lattice points unoccupied by an atom: in this case the ion collides with a target atom, resulting in transfer of a significant amount of energy to the target atom such that it leaves its crystal site. This target atom then itself becomes a projectile in the solid, and can cause successive collision events. Interstitials result when such atoms (or the original ion itself) come to rest in the solid, but find no vacant space in the lattice to reside. These point defects can migrate and cluster with each other, resulting in dislocation loops and other defects.

Amorphization

The amount of crystallographic damage can be enough to completely amorphize the surface of the target: i.e. it can become an amorphous solid. In some cases, complete amorphization of a target is preferable to a highly defective crystal: An amorphized film can be regrown at a lower temperature than required to anneal a highly damaged crystal.

Sputtering

Some of the collision events result in atoms being ejected (sputtered) from the surface, and thus ion implantation will slowly etch away a surface. The effect is only appreciable for very large doses.

Ion channelling

If there is a crystallographic structure to the target, and especially in semiconductor substrates where the crystal structure is more open, particular crystallographic directions offer much lower stopping than other directions. The result is that the range of an ion can be much longer if the ion travels exactly along a particular direction, for example the ¡110¿ direction in silicon and other diamond cubic materials. This effect is called ion channelling, and, like all the channeling effects, is highly nonlinear, with small variations from perfect orientation resulting in extreme differences in implantation depth. For this reason, most implantation is carried out a few degrees off-axis, where tiny alignment errors will have more predictable effects. Ion channelling can be used directly in Rutherford backscattering and related techniques as an analytical method to determine the amount and depth profile of damage in crystalline thin film materials.

2.3.4 The Transport of Ion in Matter (TRIM) Simulation Tool

The distribution of the implanted silicon ions can be calculated using the TRIM code developed by Ziegler [28]. This code uses universal stopping potentials that can predict the implantation distribution with an average accuracy of about 5% [29]. As shown in Fig. 2.8, there is a strong correlation between the implantation depth and the width, or 'straggle', of the ion distribution.

In order to have a well defined silicon nanocrystal layer for device applications, it is desirable to implant silicon ions at low energy to achieve a narrow implantation zone [30]. However, the ion beam current that can be extracted from the source plasma decreases rapidly at low ion beam energies, proportionately increasing the implantation time and the cost of implanting the desired stoichiometric excess of silicon in the oxide layer. Most of the samples prepared for this thesis were implanted with 80 keV silicon ions, an energy selected to balance implantation depth, straggle in the depth distribution, and sample preparation cost. More details are discussed in Chapter 6.

2.4 Conclusion

Silicon nanocrystals can be fabricated through a variety of techniques as we have discussed above. Among these processes, we use ion implantation and thermal annealing

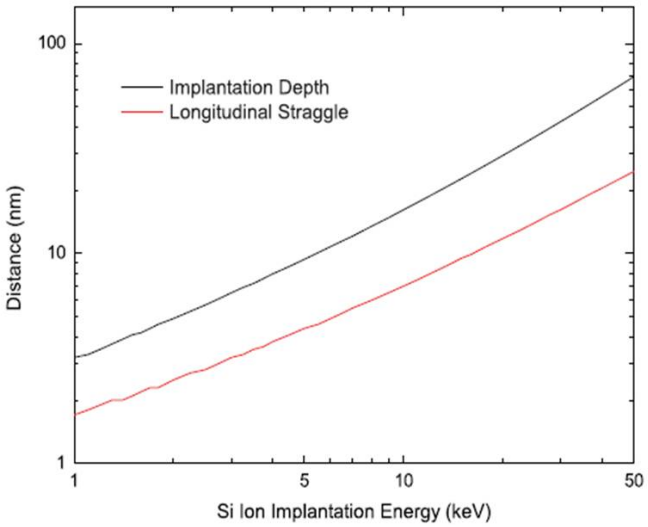

Figure 2.8: The calculated implantation range of Si ions into SiO_2 - as a function of impact energy.

to create silicon nanocrystals for our experiments and devices. This technique was selected primarily for compatibility with CMOS processing; precise control of the delivered dopant purity and dose and flexibility in the concentration and profile that can be achieved; ion implantation is already commonly used in silicon microelectronics to create doped regions in circuits. In the ion implantation procedure, ions are extracted from a plasma and accelerated by an electric field to the sample. The ions impact with sufficient energy to travel some distance into the sample before they come to rest. The total dose of implanted ions is controlled by monitoring the integrated current as the ion beam is rastered over the sample. In this way an implanted layer can be created with good uniformity across large substrates. Ion implantation is available in collaboration work with Japan Atomic Energy Agency (JAEA) located at Takasaki Center for Advanced Radiation Research.

References

[1] L. T. Canham, Applied Physics Letters 57, 1046 (1990). 12, 13

[2] A. G. Cullis and L. T. Canham, Nature 353, 335 (1991). 12

[3] L. Pavesi, L.D. Negro, C. Mazzoleni, G. Franzo, F. Priolo, Nature 408 (2000) 440. 13, 15

[4] O. Hanaizumi, K. Ono, Y. Ogawa, Appl. Phys. Lett. 82 (2003) 538. 13, 17

[5] K. Miura, Y. Kato, H. Hoshino, and O. Hanaizumi, Thin Solid Films 516, 7732-7734 (2008). 13, 17

[6] K. Miura, T. Tanemura, O. Hanaizumi, S. Yamamoto, K. Takano, M. Sugimoto, M Yoshikawa, Nucl. Instr. and Meth. in Phys. Res. B 263 (2007) 532. 13, 15, 22

[7] Iwayama, T. S., Fujita, K., Nakao, S. et al., Visible photoluminescence in Si+ implanted silica, J. Appl. Phys., 1994, 75(12): 7779. 13, 15

[8] Werwa, E., Seraphin, A. A., Chiu, L. A. et al., Synthesis and processing of silicon nanocrystallites using a pulsed laser ablation supersonic expansion method, Appl. Phys. Lett., 1994, 64(14): 1821. 13, 15

[9] Nakagawa, K., Fukuda, M., Miyazaki, S. et al., Self-assembling formation of silicon quantum dots by low pressure chemical vapor deposition, Mat. Res. Soc. Symp. Proc., 1997, 452: 243. 13, 16

[10] Miyazaki, S., Hamamoto, Y., Yoshida, E. et al., Control of selfassembling formation of nanometer silicon dots by low pressure chemical vapor deposition, Thin Solid Films, 2000, 369: 55. 13, 16

[11] T. Kominato, Y. Ohmori, H. Okazaki and M. Yasu, "Very lowloss GeO2-doped silica waveguides fabricated by flame hydrolysis deposition method," Electron. Lett. 26, 327-329 (1990). 13, 17

[12] Peng, Y. C., He, Y. L., Liu, M., Study of deposition mechanism of nc-Si:H films grown by PECVD, Chinese J. Vac. Sci. Technol. (in Chinese), 1998, 18(4): 283. 13

[13] Tong, S., Liu, X. N., Gao, T. et al., Intense violet photoluminescence at room temperature in as-deposited a-Si:H:O films, J. Non-crystal Solids, 1998, (227-230): 498. 13

[14] L. A. Nesbit, Appl. Phys. Lett. 46, 38 (1985). 13

[15] R. E. Johnson and A. Muan, J. Amer. Chem. Soc. 51, 430 (1968). 13

[16] L. L. Atl, S. W. Ing, Jr., and K. W. Laendle, "Low-Temperature Deposition of Silicon Oxide Films," J. Electrochem. Soc. 110, 465 (1963). 14

REFERENCES

[17] Zhao, X. W., Isshiki, H., Aoyagi, Y. et al., Formation and device application of Er-doped nanocrystalline Si using laser ablation, Mater. Sci. Eng., 2000, B74: 197. 15

[18] Yoshida, T., Takeyama, S., Yamada, Y. et al., Nanometer-sized silicon crystallites prepared by excimer laser ablation in constant pressure inert gas, Appl. Phys. Lett., 1996, 68(13): 1772. 16

[19] Lee, J., Becker, M. F., Keto, J. W., Dynamics of laser ablation of microparticles prior to nanoparticle generation, J. Appl. Phys., 2001, 89(12): 8146. 16

[20] Yasuda, T., Nishizawa, M., Yamasaki, S. et al., Controlled bond formation between chemical vapor deposition Si and ultrathin SiO_2 layers, J. Vac. Sci. Technol., 2000, B18(3): 1752. 16

[21] N. Imoto, N. Shimizu, H. Mori, and M. Ikeda, Sputtered Silica Waveguides with an Embedded Three-Dimensional Structure, JLT, LT-1, 289-294 (1983). 17

[22] Zhu, J. G., White, C. W., Budai, J. D. et al., Growth of Ge, Si, and SiGe nanocrystals in SiO2 matrices, J. Appl. Phys., 1995, 78(7): 4386. 21

[23] Inokuma, T., Wakayama, Y., Muramoto, T. et al., Optical properties of Si clusters and Si nanocrystallites in high-temperature annealed SiOx films, J. Appl. Phys., 1998, 83(4): 2228. 21

[24] Iacona, F., Franz, G., Spinella, C., Correlation between lumine scence and structural properties of Si nanocrystals, J. Appl. Phys., 2000, 87(3): 1295. 21, 23

[25] 25. Hirano, Y., Sato, F., Saito, N. et al., Fabrication of nanometer sized Si dot multilayers and their photoluminescence properties, J. Non-crystal Solids, 2000, (266-269): 1004. 21

[26] Takagi, H., Ogawa, H., Yamazaki, Y. et al., Quantum size effects on photoluminescence in ultrafine Si particles, Appl. Phys. Lett., 1990, 56(24): 2379. 22

[27] Kanzawa, Y., Kageyama, T., Takeoka, S. et al., Sized-dependent near-infrared photoluminescence spectra of Si nanocrystal embedded in SiO2 materials, Solid State Communications, 1996, 102(7): 533. 23

[28] http://www.srim.org/. 28

[29] J. F. Ziegler, J. P. Biersack, and U. Littmark, The Stopping and Range of Ions in Solids, New York, Pergamon Press, (1985). 28

[30] P. Normand, D. Tsoukalas, E. Kapetanakis, J. A. Van Den Berg, D. G. Armour, J. Stoemenos, and C. Vieud, Elec. and Sol. Lett. 1, 88 (1998). 28

Chapter 3

Ultraviolet-Light Emission from Fused-Silica

In this chapter we will explain the fabrication and observation of ultrviolet light emission from Si-ion-implanted fused-silica substrates under different implanting and thermal annealing conditions. UV-PL spectra having peaks around a wavelength of 370 and 800 nm were observed from the samples. We show that only the UV-light emission peak can be obtained by selecting the proper implantation and subsequent annealing conditions. We explain the fabrication method, the possible cause of the PL peak and wavelength peak shift due to change in the Si-ion-implant dose, and finally, we discuss the benefits of UV-light emission materials to the current and future Si-based technology.

3.1 Introduction

The realization of Silicon(Si)-based optoelectronic devices for integration into the current Si-technology and ultra-high speed and low-cost new generation information and communication technologies has led to many research on Si-based luminescent materials utilizing the quantum confinement effect [1], such as porous Si [2], Si-nanocrystal (Si-nc) [3, 4], and Si/SiO_2 superlattice [1, 5]. Si-ncs exhibit unique optical properties that are not observed in bulk materials. This includes the emission of light in different frequencies, which are very useful in designing the optoelectronic devices. Such emissions as red, blue, green, ultra-violet (UV) [6, 7, 8, 9] are used in designing light sources, for example, the traditional DVDs utilizes the red light sources, the Blu-ray Discs (BDs) utilizes the blue light sources. These materials are also useful in photonic

crystal technology for guiding light in the optical devices and circuits [9]. The light-emission properties of Si-ncs has to be improved and fabricated by a compatible method for integration into the existing Si-technology. Many methods have been used in the fabrication of Si-ncs (please see chapter 2 for details), which includes co-sputtering [3], chemical vapor deposition (CVD), molecular beam epitaxy (MBE), laser ablation [5], Si-ion implantation [4], etc. One of the most promising approaches to producing Si-nc, compatible with conventional microelectronic processing, may be ion implantation [10]. This is because of its ability to control the depth and distribution by changing the ion dose and acceleration energy. Subsequently, ion implantation is a potential candidate for manufacturing chemically stable and pure Si-nc for research and applications in Si-based optoelectronic devices.

The UV-light emission obtained from Si-ncs utilizing different method of fabrication and the possible cause of the PL peak has been reported earlier [11, 12, 13, 14, 15, 16, 17]. For example, the UV-PL having wavelengths from 310 to 370 nm was observed from Si-nc-including thin films prepared by reactive laser ablation of Si targets [18]. The UV-PL spectra having a peak wavelength of around 370 nm were obtained from sputtered SiO_2 films including Si-ncs produced after thermal annealing at 800 to 1100 ^{o}C [19]. The UV-light emission might originate from emission centers of interface layers between Si-ncs and SiO_2 matrices, and its intensity might be affected by sizes of Si-ncs [19]. Sample A of an oxidized porous Si in ref. [20] emitted UV-light around a wavelength of 370 nm after thermal oxidization at 700 to 1150 ^{o}C, and it was also explained that the UV-light emission seemed to originate from Si-ncs and interface layers between Si-ncs and SiO_2 produced in the thermal oxidization process [20].

We previously fabricated Si-ncs including fused-silica substrates by using the Si-ion implantation method with subsequent annealing and observed blue PL from the substrates [11]. The blue-light-emitting substrates were implanted with Si ions under the energy of 80 keV and the dose of 1×10^{17} ions/cm^2. Up to now, there are no reports about successfully achieved single UV-PL from Si-ion-implanted SiO_2 layers.

3.2 Fabrication and PL Measurements

3.2.1 Ion Implantation and Annealing

Si ions were implanted into a commercial fused-silica substrate (10 mm$\times$10 mm$\times$1 mm^t, made by ATOCK, Inc.) at room temperature in the Takasaki ion accelerators for

advanced radiation application (TIARA) of the Japan Atomic Energy Agency (see Fig. 2.6 of chapter 2). The implantation energy and dose were varied as follows:

- First sample energy = 80 keV, and dose = 1×10^{17} ions/cm^2,
- Second sample energy = 80 keV, and dose = 2×10^{17} ions/cm^2,
- Third sample energy = 80 keV, and dose = 3×10^{17} ions/cm^2, and
- fourth sample energy = 300 keV, and dose = 1×10^{17} ions/cm^2.

The Si-ion-implanted substrates were cut into four pieces (5 mm×5 mm×1 mm^t) as shown in Fig. 3.1 using a diamond-wire saw, and the pieces were annealed in an air ambient for 25 min at 1100, 1150, 1200, and 1250 ^{o}C using a siliconit furnace shown in Fig. 2.7 of chapter 2.

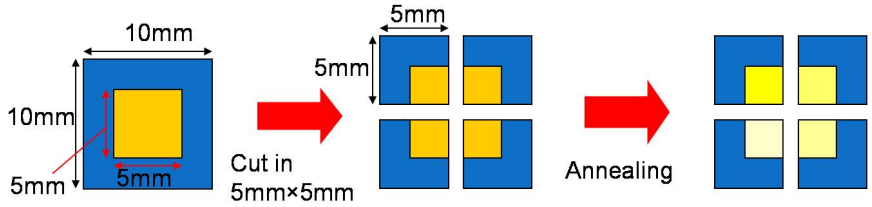

Figure 3.1: Four samples of ion-implanted substrates - cut using diamond-wire saw and annealed at 1100, 1150, 1200, and 1250 ^{o}C.

3.2.2 Photoluminescence Measurement

PL spectra were measured at room temperature with excitation using a HeCd laser (Kimmon, IK3251R-F, λ = 325 nm (≈3.8 eV), 20 mW). A monochromator (Nikon, P250), a photomultiplier (Hamamatsu, R2658), and a lock-in amplifier (NF, LI-572B) were used in our measurement setup described in Fig. 2.2 of chapter 2. We observed UV-light emission from all samples with PL peaks around a wavelength of 370 nm. The intensity of the PL spectra were calibrated by using a white-light spectrum measured with an optical spectrum analyzer (Anritsu, MS9701C + MS9030A) at wavelengths from 350 to 1750 nm because sensitivities of the monochromator and the photomultiplier depend on input wavelengths.

3.3 Results and Discussion

In this subsection, we discuss the results obtained from varying the Si-ion implantation energy, dose, and annealing temperature of four different samples. The PL measurement results are shown in Fig. 3.2 (a,b,c,d). We will give an explanation of Fig. 3.2 (a) and show the table of analysis for all samples.

3.3.1 Comparing the Fabricated Samples

Fig. 3.2 (a) shows the PL measurements from sample fabricated with energy = 80 keV, dose = 1×10^{17} ions/cm^2, and annealing temperature is varied as follows: 1100, 1150, 1200, and 1250^{o}C corresponding to each sample piece. As we can see in Fig. 3.2 (a), almost all the samples have PL peak wavelength arround 400 nm. The annealing temperature of 1100^{o}C has additional PL peak wavelength at 800 nm. The strongest PL intensity is obtained by annealing at 1200^{o}C. The effect of annealing temperature can be seen as follows: annealing temperature 1100^{o}C is 415 nm, 1150^{o}C is 412 nm, 1200^{o}C is 405 nm, and 1250^{o}C is 403 nm. It shows that the PL peak wavelength shifts to shorter wavelength as the annealing is increased while the PL intensity is strongest at 1200^{o}C and decreased when annealing temperature was increased above 1200^{o}C.

The results from other samples also show the same phenomenom, as the annealing temperature was increased, the PL peak wavelength also changed as well as the PL intensity. This experiment comfirmed the effect of Si-ion implantation parameters and the annealing conditions on the formation of Si-ncs in SiO_2 layers. Table 3.1 shows the variation of these parameters and results obtained. Furthermore, we will look into the origin of PL emission from these samples.

Table 3.1: The variation of implantation and annealing parameters - the effects of Si ion implantation and annealing temperature on the PL intensity and peak wavelength.

Sample	**Energy (keV)**	**Dose ($\times10^{17}$)**	**Wavelength peak (nm)/Temp. (°C)**				
			1100	**1150**	**1200**	**1250**	**No-anneal**
1	80	1	800,415	412	405	403	-
2	**80**	**2**	**795**	**836,378**	**372**	**374**	-
3	80	3	821	860,391	863,383	-	880,376
4	300	1	743	873,376	866,383	-	-

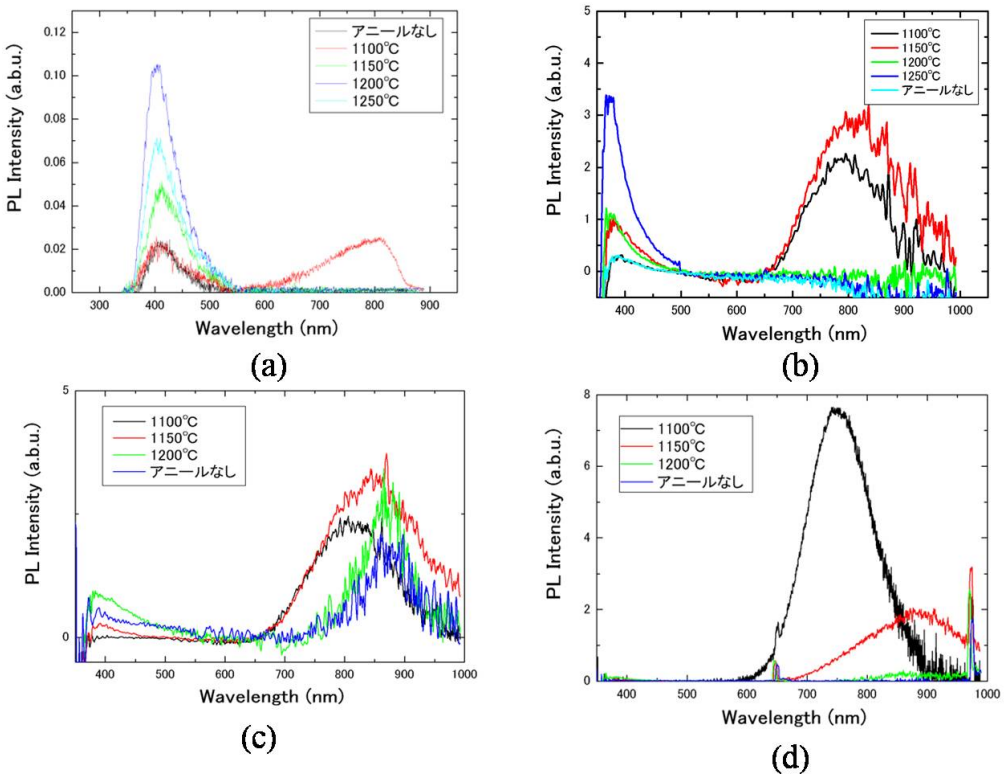

Figure 3.2: Measured PL spectra of different implantation and annealing conditions - energy and dose of (a) 80 keV, 1×10^{17} ions/cm^2, (b) 80 keV, 2×10^{17} ions/cm^2, (c) 80 keV, 3×10^{17} ions/cm^2, (d) 300 keV, 1×10^{17} ions/cm^2, and annealing temperatures of 1100, 1150, 1200, and 1250 ^{o}C.

3.3.2 A Single Peak from UV-Light Emission Band

Here we look more closely on Fig. 3.3, which presents the PL spectra of the samples (energy, 80 keV and dose, 2×10^{17} ions/cm^2) cut into four and generated at room temperature. UV-PL spectra having peaks around a wavelength of 370 nm were observed from all the samples. The UV-peak wavelengths of the samples are almost the same in spite of the varying annealing temperature. In our experiments, the UV-PL peak had a maximum intensity after annealing at 1250 ^{o}C, and the intensity was about 7.5 times higher than the samples annealed at 1100 ^{o}C.

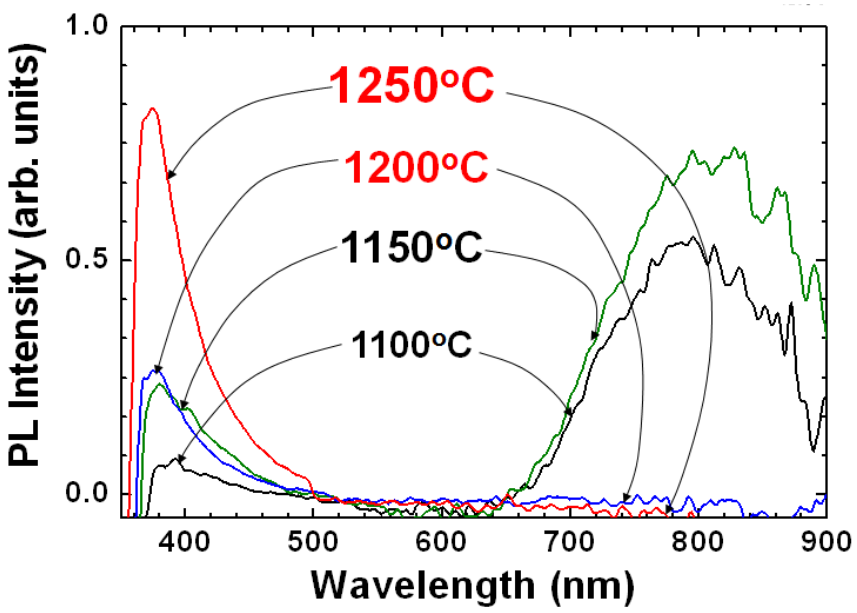

Figure 3.3: Measured PL spectra of Si-ion-implanted fused-silica substrates - Annealed at 1100, 1150, 1200, and 1250 ^{o}C (energy, 80 keV and dose, 2×10^{17} ions/cm^2).

In addition to UV PL peaks, lower-energy (longer wavelength) peaks were observed from our samples. The main PL peak from the sample annealed at 1100 and 1150 ^{o}C was located at around 1.6 eV (λ ≈800 nm). In contrast, the main PL peak from the sample annealed at 1200 ^{o}C was located in the UV range. The UV peak energy was around 3.4 eV (λ ≈370 nm) and the peak around 1.6 eV disappeared. The UV-PL peak from the sample annealed at 1250 ^{o}C had a higher intensity but the same energy, and the peak around 1.6 eV disappeared also. Such two PL peaks have been observed from Si/SiO_2 multilayered films and were described as originating from interface layers between Si and SiO_2 [12].

It is worth noting that the Si-ion-implant conditions were different from our previuos report [11] in their implantation dose and the annealing temperature of 1100, 1150, 1200, 1250 ^{o}C are common to [11]. The report in [11] shows blue-light emission at around 400 nm with the implantation energy 80 keV and Si dose 1×10^{17} ions/cm^2, while in this report, the energy 80 keV and Si-ion dose 2×10^{17} ions/cm^2 were used and shows UV-light emission at around 370 nm.

3.3.3 Origin of Light Emission

Kanemitsu et al. reported that interface layers having a band-gap energy (Eg) around 1.6 eV are produced between Si-ncs and surrounding SiO_2 if Si-ncs are surrounded by an SiO_2 medium. They also stated that the origin of emission from Si-ncs at around a wavelength of 800 nm (1.6 eV) is in the interface layers [8, 9, 10]. Kanemitsu et al. [10] indicates that interface layers between Si and SiO_2 of oxidized porous Si change to another material structure having a direct band-gap energy of 3 to 4 eV by migration of O atoms generated with increasing oxidization temperature. It has been also demonstrated by Canham et al. [13, 14], that with increasing porosity, the characteristic mean sizes of the crystallites decrease, and contemporarily the emission spectrum is shifted towards the shorter-wavelength, due to quantum confinement effects (see section 1 in Chapter 2 for more details).

Considering the above given reports and in ref. [11, 12], it seems reasonable to assume that the longer-wavelength peak (800 nm) in our samples (annealed at 1100 and 1150 ^{o}C) might have originated from the interface layers between Si-ncs and SiO_2 [8], while the shorter-wavelength peak (370 nm) in our samples (annealed at 1200 and 1250 ^{o}C) might have originated from the Si-nc's quantum confinement effect [10, 13, 14]. With increasing the temperature, the fraction of emitting nanocrystals starts to increase, giving rise to a stronger intensity. This ends at 1150 ^{o}C for the longer-wavelength peak, and at temperature above 1150 ^{o}C, the oxidation sets in, thereby decreasing the characteristic mean sizes of the crystallites (interface layers between Si-ncs and SiO_2 changes to another material structure having a direct band-gap energy of 3.4 eV). Consequently, the density of Si-ncs increases, and hence the PL peak increases. Therefore, we successfully obtained only the UV-light emission peak from our Si-ion-implanted samples by selecting the proper annealing temperature.

3.3.4 Application and benefits of UV Light Emission

UV-light emitting devices are expected to be useful in many applications such as light sources and photonic crystal waveguides [21, 22]. For example, the traditional DVDs uses red laser (650 nm) and the blue-ray disk systems uses blue laser (405 nm) sources. Similarly future higher-density optical-disk systems can use UV laser source (370 nm). The benefit of using an UV laser source is that it has a shorter wavelength than blue and red laser, which makes it possible to focus the laser spot with even greater precision. This allows data to be packed more tightly and stored in less space, so it's possible to fit more data on the disc even though it's the same size as a CD/DVD. Also the use of ion implantation technique has many benefits. Firstly, this technique is compatible with the current Si-technology, thereby making it easy and possible to integrate Si-based optoelectronic components into the existing Si-technology. Secondly, it has the advantage that a given number of ions can be placed at a controlled depth and distribution by changing the ion dose and acceleration energy [11, 15], which may enable the integration of functional materials like waveguides, resonators, etc, into the existing silicon chips. Finally, ion-beam synthesis of Si-ncs is a potential candidate for manufacturing chemically stable and pure Si-ncs for fundamental research and applications in monolithically integrated Si-based optoelectronic devices.

3.4 Conclusion

We fabricated fused-silica substrates that emit UV-light by using Si-ion implantation and high-temperature annealing. By changing the implantation and annealing conditions we could control the PL intensity and peak wavelength position. The result of their analyses showed that the PL intensity and peak wavelength position can be optimized by chosing appropriate implantation and subsequent annealing conditions. In particular, we found a sharp UV peak around a wavelength of 370 nm after annealing at 1250 ^{o}C. The UV-light emission seems to originate from Si-ncs themselves and interface layers between Si-ncs and SiO_2 media. In addition to the UV-PL peak, we observed other PL peaks ranging from red to infrared wavelengths from our samples. However, we successfully obtained only the UV-light emission peaks by selecting the proper annealing temperatures.

References

[1] Z.H. Lu, D.J. Lockwood, J.-M. Baribeau, Nature 378 (1995) 258. 33

[2] N. Koshida, H. Koyama, Appl. Phys. Lett. 60 (1992) 347. 33

[3] T. Izumi, Parity 19 (2004) 20, in Japanese. 33, 34

[4] L. Pavesi, L.D. Negro, C. Mazzoleni, G. Franzo, F. Priolo, Nature 408 (2000) 440. 33, 34

[5] Y. Yamada, T. Orii, I. Umezu, S. Takeyama, T. Yoshida, Jpn. J. Appl. Phys. 35 (1996) 1361. 33, 34

[6] O. Hanaizumi, K. Ono, Y. Ogawa, Appl. Phys. Lett. 82 (2003) 538. 33

[7] O. Hanaizumi, K. Ono, Y. Ogawa, T. Koga, Y. Hasegawa, A. Ogihara, G. Saito, Jpn. J. Appl. Phys. 41 (2002) L1084. 33

[8] Y. Kanemitsu, T. Ogawa, K. Shiraishi, K. Takeda, Phys. Rev. B 48 (1993) 4883. 33, 39

[9] Y. Kanemitsu, H. Uto, Y. Masumoto, T. Matsumoto, T. Futagi, H. Mimura, Phys. Rev. B 48 (1993) 2827. 33, 34, 39

[10] Y. Kanemitsu, T. Futagi, T. Matsumoto, H. Mimura, Phys. Rev. B 49 (1994) 14732. 34, 39

[11] K. Miura, T. Tanemura, O. Hanaizumi, S. Yamamoto, K. Takano, M. Sugimoto, and M. Yoshikawa, Nucl. Instr. and Meth. B 263, 532-534 (2007). 34, 39, 40

[12] K. Miura, Y. Kato, H. Hoshino, and O. Hanaizumi, Thin Solid Films 516, 7732-7734 (2008). 34, 38, 39

[13] L. T. Canham, Appl. Phys. Lett. 57, 1046 (1990) 34, 39

[14] A. G. Cullis and L. T. Canham, Nature 353, 335 (1991) 34, 39

[15] T.S. Iwayama, T. Hama, D.E. Hole, I.W. Boyd, Surf. Coat. Technol. 158 (2002) 712. 34, 40

[16] VL. Nikolova, R.G. Saint-Jacques, C. Dahmoune, G.G. Ross, Surf. Coat. Technol. 203 (2009) 2501. 34

[17] V. Levitcharsky, R.G. Saint-Jacques, Y.Q. Wang, L. Nikolova, R. Smirani, G.G. Ross, Surf. Coat. Technol. 201 (2007) 8547. 34

[18] I.A. Movtchan, R.W. Dreyfus, W. Marine, M. Sentis, M. Autric, G.L. Lay, N. Merk, Thin Solid Films 255 (1995) 286. 34

[19] H.Z. Song, X.M. Bao, N.S. Li, X.L. Wu, Appl. Phys. Lett. 72 (1998) 356. 34

REFERENCES

[20] J. Lin, G.Q.Yao, J.Q. Duan, G.G. Qin, Solid State Commun. 97 (1996) 221. 34

[21] O. Hanaizumi, K. Ono, Y. Ogawa, T. Matsumoto, Appl. Phys. Lett. 84 (2004) 3843. 40

[22] T. Sato, K. Miura, N. Ishino, Y. Ohtera, T. Tamamura, S. Kawakami, Opt. Quantum Electron. 34 (2002) 63. 40

Chapter 4

Photonic Crystals

In this chapter we will explain the fundamentals of the core structures of this work: photonic crystals. A photonic crystal is a periodic arrangement of electromagnetic media. Depending on whether we find a periodicity in one, two or three dimensions we speak of one-dimensional, two-dimensional and three-dimensional photonic crystal, respectively (Figure 4.1).

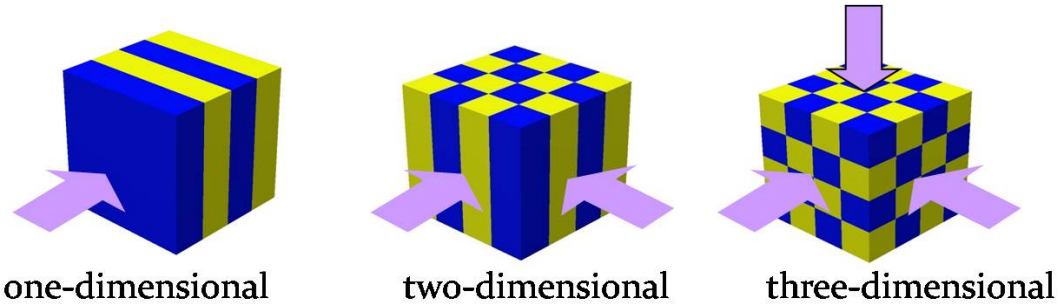

Figure 4.1: The Photonic Crystal (1-,2-,3-D) Structures - in one-, two-, and three-dimensions.

In analogy to the periodicity of the crystalline atomic lattice in semiconductors, where the periodic potential of atoms creates an energetic band-structure for electrons, the 'optical potential', i.e., the varying dielectric constant, leads to the development of a band-structure for photons in photonic crystals. Resulting photonic bandgaps which disallow the propagation of light in the crystal for frequencies inside the gap and artificially introduced defects can be applied on the development of for example mirror, waveguide, or microcavity structures. To prepare the fundamentals which are necessary for our analysis of novel photonic crystal waveguides we give a short introduction into the basic concepts of photonic crystals, origin of photonic bandgap and how they are

applied to 1-D periodic media. We will then explain how 3-D periodic media can be used to completely control light. However, because 3-D structures are difficult to fabricate, we prefer to work with 2-D periodic structures. Next, we will briefly discuss the various fabrication methods and simulation tools that can be used to model photonic crystal structures. To conclude this chapter, we will make a choice of our fabrication and modeling tool and give the reasons.

4.1 Introduction

The term photonic crystal is mainly used for 1-D, 2-D or 3-D periodic structures with a period of the order of the wavelength of the light and a high refractive index contrast in each unit cell. The concept was first introduced independently by Eli Yablonovitch and John in 1987 as a method of controlling spontaneous emission in a material [1, 2]. In a periodic medium, electromagnetic waves scattered within each period can either add up or cancel out. Because of this interference, the structure can become transparent or opaque, depending on the direction and the wavelength of the electromagnetic waves. For some geometries and a sufficiently high refractive index contrast a multi-dimensional photonic crystal can have a wavelength (or corresponding frequency) range where electromagnetic radiation cannot propagate through the structure in any direction. This wavelength range is called a photonic bandgap or PBG [3]. Photonic crystals come in many forms. The most obvious classification is by the dimensionality of the periodicity.

Figure 4.1 shows 3 kinds of photonic crystals with different periodicity. The most simple, 1-D photonic crystals have been known and used for a long time in the form of Bragg mirrors. These layered structures have a PBG for light incident perpendicular to the stack. As the angle of incidence moves away from the vertical direction, the PBG wavelength range decreases and ultimately closes. Both the width of the PBG and the maximum angle for which there is such a forbidden wavelength range is determined by the refractive index contrast between the layers; the higher the contrast, the broader the PBG [4]. In the next section, we will briefly go into the theory of these 1-D photonic crystals, as we will explain the behaviour of light in periodic media. When the periodicity is extended into other directions, the picture becomes more complicated. For each direction, the relationship between reflected electromagnetic waves is different, and the wavelength range for which the waves cancel out is shifted. Therefore, to

obtain a full PBG, these wavelength ranges should overlap for all directions. This is only possible when the refractive index contrast within the structure is sufficiently high and the structure has a high symmetry.

4.2 Electromagnetic Waves in Periodic Structures

The essential part of the invention of photonic crystals in 1987 [1, 2] was the combination of Maxwell's equations for electromagnetic fields in a dielectric structure with Bloch's theorem for periodic potentials from solid-state physics. The main aspect in understanding photonic crystals is the understanding of how these two principles interact in a periodically structured dielectric.

4.2.1 Maxwell Equations

The propagation of electromagnetic fields in photonic crystal is governed by the four macroscopic Maxwell's equations 4.1-4.4

$$\nabla \cdot \vec{B}(\vec{r},t) = 0 \tag{4.1}$$

$$\nabla \times \vec{E}(\vec{r},t) + \frac{1}{c}\frac{\partial}{\partial t}\vec{B}(\vec{r},t) = 0 \tag{4.2}$$

$$\nabla \cdot \vec{D}(\vec{r},t) = \rho(\vec{r},t) \tag{4.3}$$

$$\nabla \times \vec{H}(\vec{r},t) - \frac{1}{c}\frac{\partial}{\partial t}\vec{D}(\vec{r},t) = \frac{1}{c}\vec{J}(\vec{r},t) \tag{4.4}$$

where $\vec{E}$ and $\vec{H}$ are the electric and magnetic field vectors and $\vec{D}$ and $\vec{B}$ are the electric displacement and magnetic inductance. Since we consider a medium without free charges, the charge density ρ and the current density, $\vec{J}$ are equal to zero. To describe the interaction between light and matter one introduces macroscopic parameters such as the relative permittivity ϵ_r and the relative permeability μ_r. Assuming that each part of our structure is source-free, linear dielectric, macroscopic, isotropic and free of propagation losses and moreover possesses a magnetic permeability which is very close to unity (μ_r=1) and a dielectric constant which is not frequency dependent, the general material equations, which connect the electric and magnetic fields with the electric displacement and magnetic inductance under this assumption are now

$$\vec{B}(\vec{r},t) = \vec{H}(\vec{r},t) \tag{4.5}$$

$$\vec{D}(\vec{r},t) = \epsilon(\vec{r})\vec{E}(\vec{r},t) \tag{4.6}$$

where $\epsilon(\vec{r})$ is the spacially varying dielectric constant. In principal, $\epsilon(\vec{r})$ can also be time and/or frequency dependent, but this is not under consideration in our case. If we go back to Maxwell's equations with these assumptions they now can be written as two curl equations with the time derivatives only depending on $\vec{E}$ and $\vec{H}$ and two homogeneous equations completing the set.

$$\nabla \times \vec{E}(\vec{r},t) = -\frac{1}{c}\frac{\partial}{\partial t}\vec{H}(\vec{r},t) \tag{4.7}$$

$$\nabla \times \vec{H}(\vec{r},t) = \frac{1}{c}\epsilon(\vec{r})\frac{\partial}{\partial t}\vec{E}(\vec{r},t) \tag{4.8}$$

$$\nabla \cdot \vec{E}(\vec{r},t) = 0 \tag{4.9}$$

$$\nabla \cdot \vec{H}(\vec{r},t) = 0 \tag{4.10}$$

In practical applications, e.g. solving these equations numerically, it is sufficient to solve the curl equations while assuring the homogeneous equations are fulfilled. In this case it might be convenient to rearrange the curl equations in a way that they depend only on $\vec{E}$ or $\vec{H}$, respectively. This leads to two second order wave equations, which are often called master equations in literature [4]:

$$\nabla \times \left[\epsilon^{-1}(\vec{r})\nabla \times \vec{H}(\vec{r},t)\right] = -\frac{1}{c^2}\frac{\partial^2}{\partial t^2}\vec{H}(\vec{r},t) \tag{4.11}$$

$$\epsilon^{-1}(\vec{r})\nabla \times \left[\nabla \times \vec{E}(\vec{r},t)\right] = -\frac{1}{c^2}\frac{\partial^2}{\partial t^2}\vec{E}(\vec{r},t) \tag{4.12}$$

4.2.2 Bloch waves and Brillouin Zone

A photonic crystal possesses discrete translational symmetry because of its periodic dielectric function,

$$\epsilon(\vec{r}) = \epsilon(\vec{r} + \vec{R}_i) \tag{4.13}$$

for some primitive lattice vectors $\vec{R}_i$ ($i = 1, 2, 3$ for a crystal periodic in all three dimensions). One of the most fundamental results in the theory of crystals is the Bloch theorem [5]. It states that the wave function $\vec{\Psi}(\vec{r})$ of an electron, moving in a periodic potential is given by

$$\vec{\Psi}_{n,k}(\vec{r}) = \vec{u}_{n,k}(\vec{r})\exp^{i\vec{k}\vec{r}} \tag{4.14}$$

where n is the so-called band index, $\vec{k}$ is the wave vector and the $\vec{u}_{n,k}$ are periodic functions with $\vec{u}_{n,k}(\vec{r}) = \vec{u}_{n,k}(\vec{r} + \vec{R}_i)$. This means that the crystal is invariant under a

translation by $\vec{R}_i$. The formation of energy bands for electrons in periodic potentials is a direct consequence of the Bloch theorem. For photonic crystals we describe the linear propagation of photons by the wave equation 4.12. But for a periodic arrangement of dielectric materials we find that the Bloch theorem holds as well. So we can express the solutions of the wave equation as

$$\vec{H}_{n,k}(\vec{r}) = \vec{u}_{n,k}(\vec{r}) \exp^{i\vec{k}\vec{r}} . \tag{4.15}$$

The consequences are, just like in the electronic case, the formation of energy bands for electromagnetic waves. Most importantly, it is possible to produce crystals where the different bands are separated by so-called band gaps. These gaps are frequency regions where no propagation of radiation is possible. If the bandstructure of a Photonic Crystal does contain such a band gap, it is called Photonic Band Gap (PBG) material.

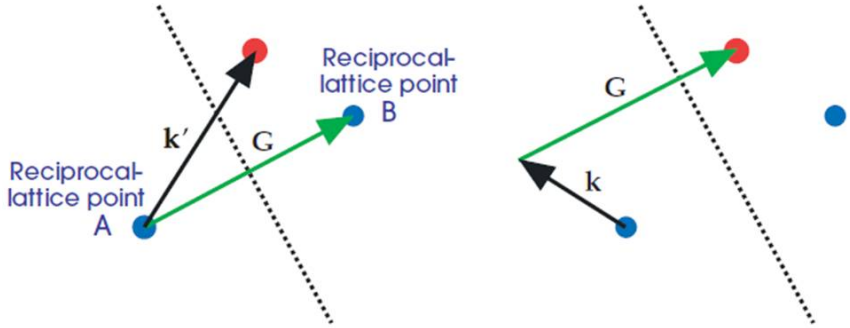

Figure 4.2: The Characterization of Brillouin zone - wavevectors $\vec{k}$ and $\vec{k} + \vec{G}$ ($\vec{G}$ is a reciprocal lattice vector) produce the same set of eigenfunctions and corresponding eigenvalues.

From Bloch's theorem, wavevectors $\vec{k}$ and $\vec{k} + \vec{G}$ ($\vec{G}$ is a reciprocal lattice vector) produce the same set of eigenfunctions and corresponding eigenvalues. Therefore we can restrict our analysis to the smallest region in k-space that can be expanded to the entire k-space by adding reciprocal lattice vectors. Only this region contains non-redundant information. From solid state physics we know that this smallest possible region can be constructed as the primitive Wigner-Seitz cell in reciprocal space and is called the first Brillouin-zone (1BZ) [4]. This concept is easily understood in a one dimensional photonic crystal, because it is obvious that only k-values from $-\pi/a$ to π/a (which is equivalent to -0.5G to 0.5G) fulfill this condition. The complete frequency eigenvalue spectrum of the system can be obtained by calculating the eigenvalues for

these k-values. One step further we can sort all eigenvalues corresponding to a certain k-value and label them by an index, we will refer from now to as the band-index n. The unique representation of an eigenfunction is therefore

$$\vec{H}^n_{\vec{k}}(\vec{r}) = \exp^{i\vec{k}\vec{r}} \sum_{\vec{G}} \vec{H}^n_{\vec{k},\vec{G}} \exp^{i\vec{G}\vec{r}} = \exp^{i\vec{k}\vec{r}}\, \vec{u}^n_{\vec{k}}(\vec{r}). \tag{4.16}$$

The combination of these two concepts results in an ω over $\vec{k}$ diagram which is called the bandstructure and has proven to be very useful when discussing the properties of periodic systems in solid state physics, and now as well in the field of photonic crystals. The frequencies are displayed in units of $2\pi c/a$, which has proven to be useful. As Maxwell's equations are linear, the geometry and eigenvalues/eigenfunctions scale also linearly. Therefore it makes sense to normalize frequencies by a fundamental length of the crystal, the lattice constant. The normalization to $2\pi c/a$ is always assumed in this work when no explicit frequency units are given.

4.3 The Origin and Principles of PBG

There is a special interest in photonic crystals with a photonic band gap (PBG). This is a frequency range where light is not allowed to propagate, irrespectively of the direction of propagation. Finding a PBG is of interest, since this gives suppression and enhancement of spontaneous emission inside a crystal. Numerous studies have shown the existence of such PBGs. As mentioned, the PBG can result in the modification of spontaneous emission in the crystal. In a PBG the density of states is zero and an atom is not allowed to emit in the frequency range of the gap. The control of spontaneous emission is very interesting from a fundamental point of view, but may also have various interesting applications. Lasers, for example, rely on stimulated emission, and spontaneous emission decreases their performance. When we embed a laser in a proper PBG material one may enhance the performance. If a defect is introduced in the otherwise perfect crystal, localized photonic states in the gap will be created. By introducing defects, light can be localized or guided along the defects modes. A defect can introduce an extra energy level in the gap, called an impurity level, in which a photon can be trapped.

A complete photonic band gap is a range of ω in which there are no propagating (real $\vec{k}$) solutions of Maxwell's equations (4.12),(4.12) for any $\vec{k}$, surrounded by propagating

states above and below the gap. There are also incomplete gaps, which only exist over a subset of all possible wavevectors, polarizations, and/or symmetries. We discuss both sorts of gaps in the subsequent sections, but in either case their origins are the same, and can be understood by examining the consequences of periodicity for a simple one-dimensional system.

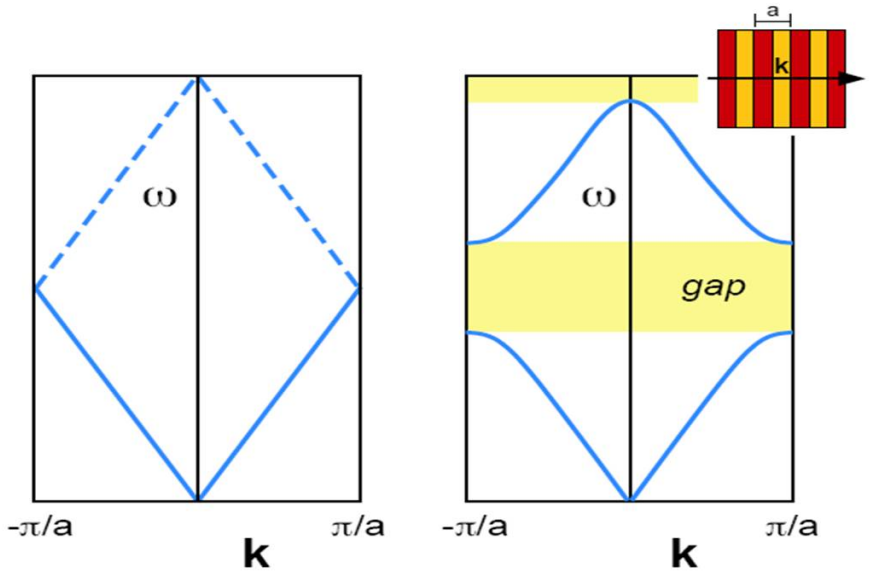

Figure 4.3: The Schematic description of variational theory - Left: Dispersion relation (band diagram), frequency ω versus wavenumber k, of a uniform one-dimensional medium, where the dashed lines show the folding effect of applying Bloch's theorem with an artificial periodicity a. Right: Schematic effect on the bands of a physical periodic dielectric variation (inset), where a gap has been opened by splitting the degeneracy at the $k = \pm\pi/a$ Brillouin-zone boundaries (as well as a higher-order gap at $k = 0$).

Consider a one-dimensional system with uniform $\epsilon = 1$, which has planewave eigensolutions $\omega k{=}ck$, as depicted in Fig. 4.3(left). This ϵ has simple periodicity a for any $a \geq 0$, with $a = 0$ giving the usual unbounded dispersion relation. We are free, however, to label the states in terms of Bloch envelope functions and wavevectors for some $a \neq 0$, in which case the bands for $|k| > a$ are translated ('folded') into the first Brillouin zone, as shown by the dashed lines in Fig. 4.3(left). In particular, the $k = -\pi/a$ mode in this description now lies at an equivalent wavevector to the $k = \pi/a$ mode, and at the same frequency; this accidental degeneracy is an artifact of the 'artificial' period we have chosen. Instead of writing these wave solutions with electric fields $\vec{E}(x) \approx \exp(\pm i\pi x/a)$, we can equivalently write linear combinations $e(x) = \cos(\pi x/a)$ and $o(x) = \sin(\pi x/a)$ as shown in Fig. 4.4, both at $\omega = c\pi/a$. Now, however, sup-

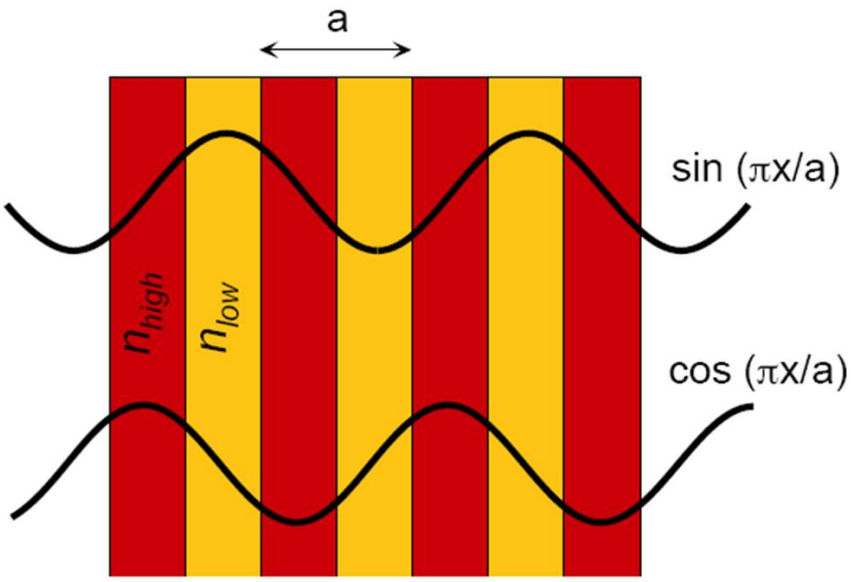

Figure 4.4: Schematic origin of the band gap in one dimension - The degenerate $k = \pm\pi/a$ planewaves of a uniform medium are split into $\cos(\pi x/a)$ and $\sin(\pi x/a)$ standing waves by a dielectric periodicity, forming the lower and upper edges of the band gap, respectively-the former has electric-field peaks in the high dielectric (n_{high}) and so will lie at a lower frequency than the latter (which peaks in the low dielectric).

pose that we perturb ϵ so that it is nontrivially periodic with period a; for example, a sinusoid $\epsilon(x) = 1 + \Delta \cdot \cos(2\pi x/a)$, or a square wave as in the inset of Fig. 4.3. In the presence of such an oscillating 'potential', the accidental degeneracy between $e(x)$ and $o(x)$ is broken: supposing $\Delta > 0$, then the field $e(x)$ is more concentrated in the higher-ϵ regions than $o(x)$, and so lies at a lower frequency. This opposite shifting of the bands creates a band gap, as depicted in Fig. 4.3(right). (In fact, from the perturbation theory described subsequently, one can show that for $\Delta << 1$ the band gap, as a fraction of mid-gap frequency, is $\Delta\omega/\omega \cong \Delta/2$). By the same arguments, it follows that any periodic dielectric variation in one dimension will lead to a band gap, i.e., $\epsilon \neq 0$.

Finally, we conclude that the low-frequency modes (modes under the gap) concentrate their energy in the high-ϵ regions, and the high-frequency (modes above the gap) modes concentrate their energy in the low-ϵ regions. The low-ϵ regions are called the air regions while the high-ϵ regions are called the dielectric regions. The situation is analogous to the electronic band structure of semiconductors, in which the 'conduction band' and the 'valence band' surround the fundamental gap.

4.3.1 Two-Dimensional Photonic Crystals

A two dimensional photonic crystal possesses periodicity in two directions. To achieve a complete photonic bandgap we need to fulfill two basic conditions: First we need overlapping bandgaps for each $\vec{k}$ point in each direction of the irreducible Brillouin zone. This means that for a given ω_0 inside the gap there exists no possible real value of $\vec{k}_{||}$, the mode is evanescent inside the crystal. Second, in a two-dimensional photonic crystal there are basically two types of polarization: transverse electrical (TE) modes with the electric field in plane and the magnetic field in z-direction and transverse magnetic (TM) modes with the magnetic field in plane and the electric field perpendicular in z-direction. To achieve a complete bandgap, both of the bandgaps of these two polarizations which possess entirely different band-structures need to overlap. Taking into account the vectorial boundary conditions of the electric field we can analytically find a heuristic of the topology of a lattice which possesses this behavior [4]: the dielectric structure should consist of dielectric veins which contain an electric field oriented parallel to them.

Note that structures with low index holes and high index dielectric are better suited for TE-modes, while structures composed of dielectric rods surrounded by air possess a larger TM-bandgap.

4.4 Applications of Photonic Crystals

Photonic crystal has applications in many areas including but not limited to Low-Loss Optical Waveguides, Waveguide Bends, High-Q Microcavities, High-Quality Filter, Channel Drop Filters, Optical Limiter, Beam Splitter, Bragg Reflector, Superprism Phenomenon, Spot Size Converter, Zero Cross-Talk, Waveguiding through Localized Coupled Cavities, and so on (the list continues). However, in this section we briefly discuss a few applications that are needed in our thesis, i.e., Waveguides.

4.4.1 Low-Loss Optical Waveguides

When line defects are introduced into a photonic crystal lattice, an electromagnetic wave having a frequency within the bandgap of the structure can be guided through the crystal. In this case the line defect resembles a waveguide as shown in Fig. 4.5 (b).

In this way line defects can be formed by either adding or removing dielectric material to a certain row or column along one of the directions of the photonic crystal.

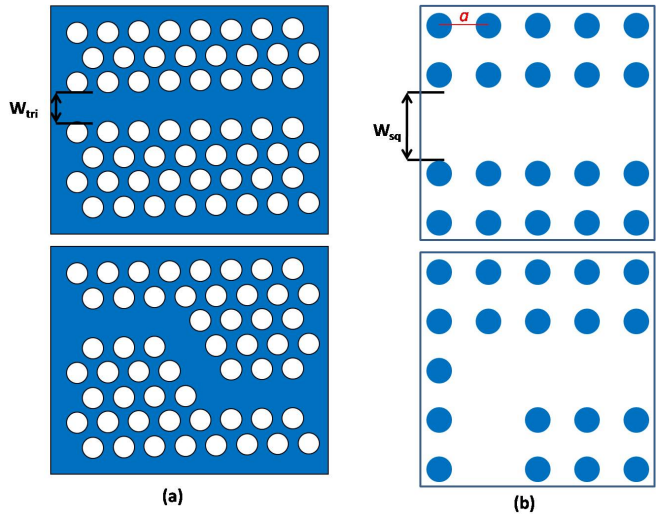

Figure 4.5: The Schematic description of defects introduction in 2D PhCs - different types of defects introduced in 2D PhC structures.

To this end, photonic crystal waveguides can be used as an optical wire to guide an optical signal between different points, or devices, within an optical integrated circuit or an optical network. To create such a channel, we can decrease the radius of a certain row to the point that it no longer exists. By doing so we have created a waveguide that has a width of

$$W_{sq} = (N + 1)a - 2r \tag{4.17}$$

where N is the number of rows or columns where the line defect will be created, and r is the radius of the rods from which the photonic crystal was created. The width of the line defect/waveguide is proportional to the number of guided modes for a certain wave vector.[6, 7] Field patterns for every eigenmode as well as energy flow can also be calculated using the FDTD method on the two-dimensional structure presented above.[8]

Waveguides can be also created on a two-dimensional triangular lattice photonic crystal of air holes in silicon (Si) background (Fig. 4.5 (a)), for which TE modes can be guided through a line defect. In such a structure the line defect is created in the crystal by increasing the dielectric constant of the line defect, as opposed to decreasing the

dielectric constant of the line defect for the two-dimensional rectangular lattice case, which was used to guide TM waves. For the triangular lattice the waveguide width can be calculated using:

$$W_{tri} = (N+1)\frac{\sqrt{3}}{2}a - 2r \tag{4.18}$$

Note that for a perforated dielectric slab, elimination of a single row or column will not be sufficient to have a single mode of propagation through the line defect, and further design considerations must be taken to achieve that goal.[7]

By removing a column or a row, we can confine the optical beam to the waveguide in a very similar fashion to the total internal reflection (TIR) concept, which is used to confine the optical signal in optical fibers. However, in photonic crystals the mechanism of in-plane optical confinement for a wave propagating through the defect is through multiple or distributed Bragg reflections (DBR). For finite height photonic crystal structures (slabs), vertical confinement is achieved through TIR at the interface between the PhC slab and lower dielectric constant material, e.g., air.

The main idea of operation for this kind of waveguide is that an incident beam with a frequency within the bandgap of the structure will not propagate through the structure, but it will propagate through the waveguide with minimal field leakage. Using this approach, a throughput efficiency as high as 100% can be achieved through the waveguide. [9] A snapshot of an FDTD simulation of an optical pulse propagating through the above structure is shown in Fig. 4.6.

4.4.2 Waveguide Bends

A low-loss waveguide that includes a sharp 90^o bend in the two-dimensional photonic crystals has been reported.[9] Theoretically, it was shown by a simple scattering theory that 100% transmission is possible. Experimentally, over 80% transmission was demonstrated at a frequency of 100 GHz by using a square array of circular alumina rods having a dielectric constant of 8.9 and a radius of $0.2a$, where a is the lattice constant of the array. For $a = 1.27$ mm, the crystal had a large bandgap extending from 76 GHz to 105 GHz. A line defect was created inside the crystal by removing a row of rods. The optical guided mode produced by the defect had a large bandwidth, extending over the entire bandgap. A snapshot of FDTD simulation of the structure described above is shown in Fig. 4.7.

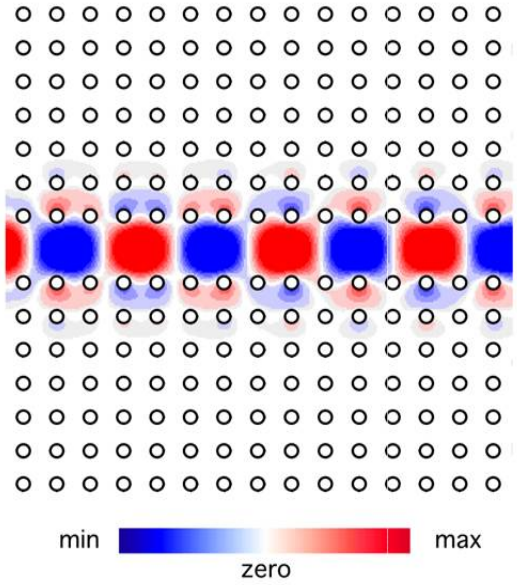

Figure 4.6: The propagation in 2D PhC line defects - a snapshot of an FDTD simulation of an optical pulse propagating through the above structure [9].

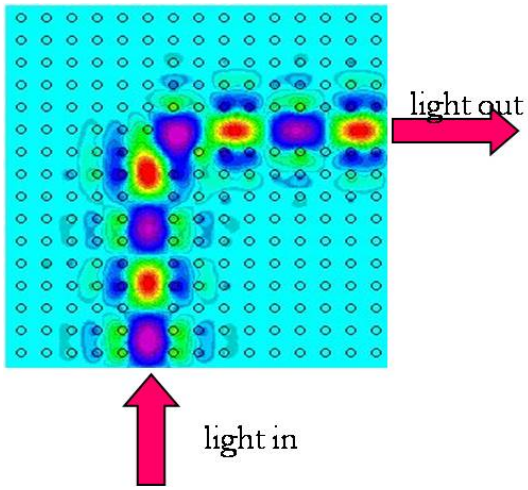

Figure 4.7: The propagation in 2D PhC bend defects - a snapshot of an FDTD simulation of an optical pulse propagating through the above structure [9].

4.4.3 Waveguiding Mechanism

What is the motivation of using PhC-based waveguides instead of conventional waveguides? In conventional slab-based waveguides the energy distribution has a tail extending in the claddings and the waveguiding relies on 'total internal reflection' (TIR). When the waveguide turns a bend TIR condition is broken and energy leaks away from the waveguide. On the other hand, in a PhC-based waveguide the lateral 'walls' are 'metallic-like' because the wave is strongly attenuated inside them for frequencies in the PBG. Then, sharp bends in PhC-based waveguides are possible, in principle, because inplane radiation losses are suppressed.

A line defect waveguide can be made, for example, by omitting an entire row of rods or holes from a 2D crystal lattice of air holes in silicon (see Fig. 4.5) Because we are increasing locally the amount of high-index material, the frequencies of some modes from the upper PBG edge will be reduced, and they will be pulled down into the PBG region, forming 'defect' states. These states (which can be called 'donor-type' in analogy with semiconductor physics) will be localized along the line defect, because of the PBG effect that prohibits propagation in the lateral direction. This phenomenon is called 'gap confinement' (GC) [10]. But even for frequencies outside PBG light localization along the line defect is possible, due to the effective index contrast between the waveguide and its lateral 'walls'. This is called 'index PBG. For a line defect waveguide in a PCS, the confinement in the vertical direction is of the IC-type, provided by the refractive index contrast between the slab core and its claddings.

4.4.4 The Projected band diagram

A line defect waveguide has 1D translational symmetry along its axis. The 1BZ collapses to a line interval because the only meaningful wave-vector component (named here β) is the one parallel to the line defect. The 1BZ's for line-defect waveguides along Γ-K and Γ-M are $(0,\pi/a)$ and $(0,\pi/a\sqrt{3})$, respectively. The analysis of guided modes requires a new representation of the band structure. We call this the projected band diagram Fig. 4.8.

Introduction of a line defect can break all the symmetries of the original lattice. That is why we have to consider the full 1BZ. Waveguides along high symmetry directions Γ-K and Γ-M (Fig. 4.5) can still have mirror symmetry with respect to their middle axis; their modes can be classified as 'even' or 'odd' with respect to this axis. In

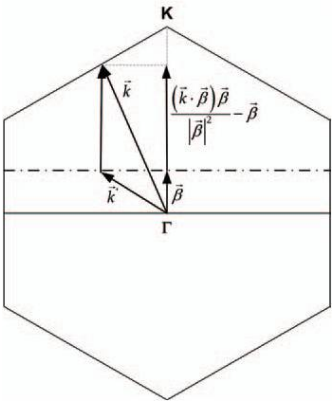

Figure 4.8: The Schematic description of projected band diagram - line defect waveguide has the only meaningful wave-vector component parallel to the line defect.

3D, the light cone of a PCS will be projected and become the light line. In the 1BZ of the line defect the light line is a line passing through the origin, with an inverse slope given by the effective index of the highest-index cladding.

The projection creates continua of states (combinations of ω-k) that are allowed to propagate in the bulk photonic crystal and reveals the projected gap between these states. The band projection can be done along Γ-K or Γ-M. For the projection along Γ-M, the gap region below the light line is very much reduced in comparison with the projection along Γ-K. Since this region is the window of lossless waveguiding, in what follows we will consider only waveguides along Γ-K. The existence of a projected gap does not require the original crystal to have a complete bandgap. In other words, an incomplete gap is sufficient for straight waveguides. However, when straight waveguides are combined into more complex devices, like bends and Y-junctions, only an omnidirectional gap can prevent scattering losses into the surrounding photonic crystal.

4.4.5 Supercell approach to Line Defect Waveguides

Line defect waveguides can be modeled by using a supercell (Fig. 4.9) approximation [11]. The supercell is a rectangular domain with a width (transverse to the line defect) equal to a few lattice constants and a length of one period (along the line defect). A proper choice of the supercell should contain an integer number of primitive cells of the original lattice.

In the computation, we apply Bloch boundary conditions on the supercell sides. This means that we are practically considering a periodic array of waveguides, where

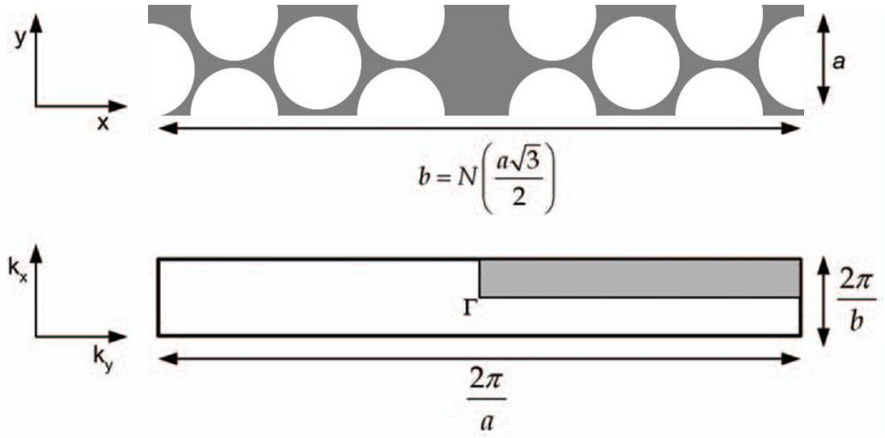

Figure 4.9: The Schematic description of Supercell - approach to line defect waveguides.

the separation between them is determined by the supercell width. The width should be large enough in order to minimize the coupling between guided modes in neighboring waveguides. A waveguide made by omitting a row of holes in an otherwise periodic slab (so-called W1 waveguide) is symmetric with respect to its middle axis, and the guided modes can be classified as odd and even with respect to it.

4.5 PhC Modeling Tools

The aim of this subsection is to present an overview of most common computational methods and modeling tools applicable to PhC design and analysis. The emphasis will be put on strengths and weaknesses of each method. The FDTD method will be discussed in greater level of detail, because it reveals the main physical properties of PhCs. The calculation results, their physical interpretation and the design rules derived from them will be presented in the next chapter.

4.5.1 Plane Wave Expanssion (PWE) Method

PWEM consists in expanding the periodic functions in appropriate Fourier series and inserting the expansions into the wave equation. The result is an infinite matrix-eigenvalue problem, which has to be truncated for numerical calculations. Through solving the eigenproblem one obtains the spectrum of eigen-frequencies (i.e. band structure) and expansion coefficients for the Bloch eigenmodes. An early PWEM implementation [12] was not successful due to the fact that vector nature of the EM field

was ignored. Shortly after, this mistake was corrected [13], and PWEM has become the most popular method of analyzing PhCs.

The MPB program [14] can be applied for calculating localized 'defect' states in the PBG (e.g. modes guided along a line-defect in a photonic crystal) by using a supercell. The supercell is a domain composed of many unit cells that surround the 'defect' region. The increase in domain size leads to the increase of memory requirements and calculation time. The band folding effect produces many redundant bands below the PBG that will all be computed through the standard eigensolver in MPB. A shortcut to the 'defect' states would be to use a 'targeted' eigensolver that can shift the frequency origin in the PBG region. Unfortunately, the targeted eigensolver in MPB seems to have convergence problems for line-defects.

A potential disadvantage of the planewave basis is that it corresponds to a uniform spatial grid. A set of localized functions on an unstructured mesh (e.g. finite-element) can provide a more economical solution. In the case of a dispersive material (i.e. dielectric function depends not only on position, but also on frequency), the frequency ω cannot be factorized, and solving for it means finding the roots of a nonlinear and transcendental function. This represents a very difficult numerical task. In PWEM the structure is supposed to be of infinite extent and only propagative Bloch states are calculated. Evanescent states are a priori excluded.

4.5.2 Finite-Difference Time-Domain (FDTD) Method

The FDTD [15] method reproduces numerically the propagation in real space of time-varying electromagnetic waves. FDTD has been widely used for calculating the radiating properties of finite-sized photonic crystals (e.g. quality factors [16] and their transmission spectra [17]. Moreover, FDTD has been combined with Bloch boundary conditions for calculating the band structure of a photonic crystal [18]. The most common implementation of FDTD is the Yee algorithm [19]. The real space is discretized in a cubic grid that stores the dielectric constant and the fields. $\vec{E}$ and $\vec{H}$ field components are interleaved at intervals in space and in time. Every $\vec{E}$ component is surrounded by a circulating $\vec{H}$ component and viceversa. The space and time derivatives are expressed through central differences, and a leap-frog time marching scheme is used for recursively updating the fields on every grid point. PMLs are used at the outer edge of the FDTD mesh in order to simulate the open space. After setting up the

domain geometry and materials properties, one has to specify the spatial and temporal excitation of electromagnetic fields and spatial positions and geometry of detectors.

4.5.3 Finite-Element Method (FEM)

The finite element method (FEM) is a numerical technique for finding approximate solutions of partial differential equations (PDE) as well as of integral equations. The solution approach is based either on eliminating the differential equation completely (steady state problems), or rendering the PDE into an approximating system of ordinary differential equations, which are then numerically integrated using standard techniques such as Euler's method, Runge-Kutta, etc.

FEM uses an unstructured mesh for representing the domain, which is broken down into many elements of simple shape and different size and orientation. This kind of mesh brings up two main improvements with respect to e.g. a uniform Cartesian grid: (i) regions of arbitrary shape are represented better (no staircase approximation); (ii) the FEM mesh can use locally a higher density of nodes in key regions that require it (e.g. narrow veins of high refractive index, typical in photonic crystals), without refining the discretisation of the whole domain. Moreover, since the discontinuous refractive index is handled in real space, FEM does not have the convergence problems of classical PWEM. Briefly, FEM goes as follows. Maxwell's equations are cast into a set of linear equations which approximate the field over an element: some interpolation function is chosen and its coefficients are computed for each element and stored as elemental matrices; these matrices are then assembled into global matrices that form an eigenvalue problem whose dimension depends on the number of elements. A detailed description of FEM technique applied to photonic crystals can be found in [20].

The eigenproblem matrices appearing in FEM are very sparse, leading to an algorithm complexity O(N), where N is the number of degrees of freedom, proportional with the number of nodes. Despite this favorable scaling, FEM runs into trouble for large 3D domains, due to huge memory requirements. Still, FEM can be successfully applied for 2D finite-sized photonic crystals and 3D primitive-cell problems with Bloch boundary conditions.

4.5.4 Transfer Matrix Method (TMM)

This method has been introduced by Pendry and MacKinnon [21] in analogy with on-shell (i.e. fixed frequency) methods in low-energy electron diffraction theory. Instead of transforming to Fourier space, TMM is based on representing Maxwell's equations on a discrete lattice (Cartesian, in general) of real space points. The resulting discrete equations are recast into the form of a transfer matrix that connects the electric and magnetic fields in one layer of lattice points to those in next layer.

By taking products of transfer matrices one can find the fields at every point of the domain. But it is well-known that the multiplication of transfer matrices can suffer from serious numerical instabilities, due to exponentially growing terms. The solution to this problem is to divide the domain in 'slices' thin enough so that these instabilities do not occur, then combine these slices using a stable recursion algorithm (e.g. scattering matrix). However, stability comes at the price of reduced speed, because the simple multiplication of sparse transfer matrices is replaced by a more involved recursion. TMM yields the transmission spectrum directly (this can then be compared with experimental data) and Bloch wavevectors via the eigenvalues of the matrix. TMM uses a uniform Cartesian grid, but it can be better adapted by a coordinate transformation [22].

4.6 Fabrication Methods

To fabricate photonic crystals, materials with a periodic refractive index on a wavelength length scale are needed. The most common way to accomplish this is to use two materials of different refractive index and use these as building blocks for a periodic lattice. If microwaves are used, the typical length scale is in the mm to cm range and crystals can be fabricated by hand. Because of the scaling properties of photonic crystals [4], experiments on such crystals were used to verify the early photonic band-structure calculations [23, 24, 25]. To scale down these ideas to visible and near-infrared wavelengths calls for fabrication techniques that assemble structures on a submicron length scale. Over the years the nanofabrication problem has proven to be a main research direction for many research groups and up to now the fabrication of large, high quality crystals still is a major challenge. Two fundamentally different approaches have

been tried, based on either self-assembly of colloidal particles, or lithography combined with etching techniques.

4.6.1 Self-Assembly of Colloidal Particles

The self-assembly approach utilizes colloidal spheres that can self-organize in several different colloidal crystal symmetries if their size polydispersity (i.e., the relative width of the size distribution) is low enough [26, 27]. Particles can be made from different materials (e.g. latex, SiO_2, ZnS) by a corresponding wet chemical synthesis route and are available in a size range from well below 100 nm up to several microns in diameter, providing the length scales required for visible and near-infrared wavelengths.

Although large 3-D colloidal crystals can be grown, the difficulty of this technique is to control the crystallization process in such a way as to make structures with different lattice symmetries. This technique inevitably leads to the incorporation of random defects in the crystal. Drying of the crystals results in cracking of the crystal, this is caused by shrinkage of the individual colloidal particles in the crystal. In practice most colloidal crystals thus consist of a number of relatively small single crystalline domains. In addition, the colloids used typically do not have a high enough index contrast to obtain a complete photonic bandgap. The latter issue can be solved by infiltrating the crystal with a high index material (e.g. TiO_2 [28] or Si [29, 30]) followed by removal of the original particles, thus creating an inverse structure of high index contrast.

4.6.2 Lithography combined with Etching

The other main route to fabricate photonic crystals is to use etching techniques in a planar substrate. This approach requires the fabrication of lithographic masks with feature sizes down to 100 nm. The mask is then used in an anisotropic etching process in high index materials, such as Si [31], GaAs [32, 33] and other semiconductors [34, 35]. Although deep-UV optical lithography can be used for this purpose, most masks are fabricated by electron-beam lithography which provides a high level of control over the structure. This technique is most suited for 2-D structures since the mask technology is essentially a 2-D technology.

Silicon-based structures and other materials can be used to fabricate photonic crystals. The etching of other materials calls for a different reactive ion etching process, using different reactive species to etch the material. To etch different structures one

needs to change the lithographically defined mask and tune the etching process to fabricate the structure. Two important limitations of the technique exist, being the minimum feature size that can be defined in the lithography process and the anisotropy of the reactive ion etching process which limits the maximum attainable aspect ratio of the elements constituting the photonic crystal. Feature sizes down to 100 nm and aspect ratios of 1-2 are readily available given modern semiconductor processing technology. By tuning the electron-beam lithography process, a smaller minimum feature size can be attained which enables fabrication of structures for visible and near-infrared wavelengths. For the aspect ratio, the requirements to fabricate most photonic crystals are just beyond these standards. A major challenge therefore is the optimization of the processing conditions to fulfill the requirements on aspect ratio.

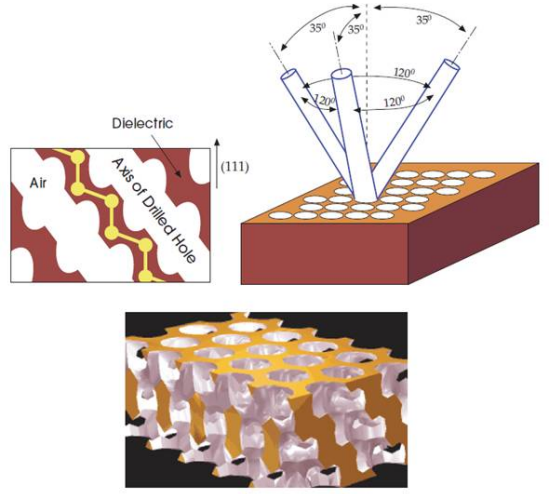

Figure 4.10: The Schematic diagram of Yablonovite - drilling of angular holes.[39]

The fabrication of 3-D structures for near-infrared wavelengths using lithographic tools is more difficult and is limited to a finite number of layers given the present technology. Different approaches have been tried, including the layer-by-layer fabrication of woodpile structures in Si [36, 37] and GaAs [38], direct etching of the 'Yablonovite' structure in GaAs [39], and a deposition technique in which a 2-D pattern defined in the first layer is propagated in the growth of a SiO_2/Si stack called authocloning [40]. Although in all these processes the number of layers is limited, these photonic crystals display many of the properties of their infinite counterparts because of the high index contrast that is typically used. Furthermore, since ion etching techniques are

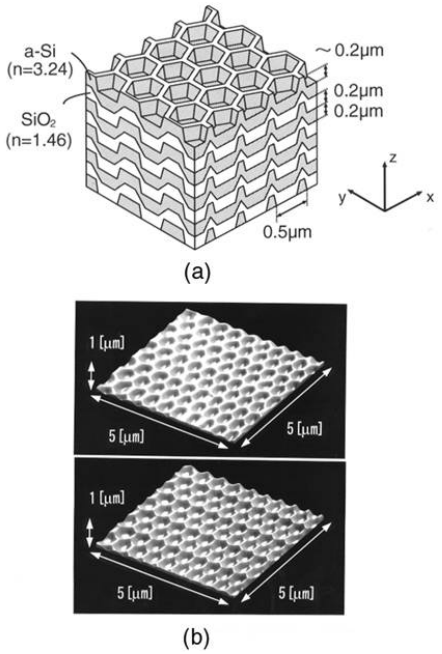

Figure 4.11: The Schematic diagram of Autocloned 3D PhCs - the 2-D pattern defined in the first layer is propagated in the growth of a SiO_2/Si stack.[40]

used, it becomes possible to define, control and tailor defects that add functionality to the structure; this is much more difficult to achieve in structures defined by self assembly. Fig. 4.10 and Fig. 4.11 show the examples of 3D PhCs (Yablonovite [39] and Autoclone [40]).

Therefore, since we are working on the two-dimensional photonic crystals, we will employ the EBL and plasma etching technique. Below we give an overview of these techniques and show their fabrication setups and processes.

4.6.3 Electron beam lithography (EBL) systems

Photonic crystals operating in the infrared wavelengths require uniform feature sizes on the order of hundreds of nanometers. To draw reproducible, uniform periodic patterns in this size range, a resolution of less than 10 nm is necessary. EBL is ideal for patterning small area devices since an electron beam can be focused to a spot size of under 5 nm diameter and can be scanned using magnetic lenses with precision of a nanometer or less. EBL systems (Fig. 4.12) can be classified according to both beam shape and beam deflection strategy. Older systems used Gaussian-shaped beams and scanned

these beams in a raster fashion. Newer systems use shaped beams, which may be deflected to various positions in the writing field also known as vector scan.

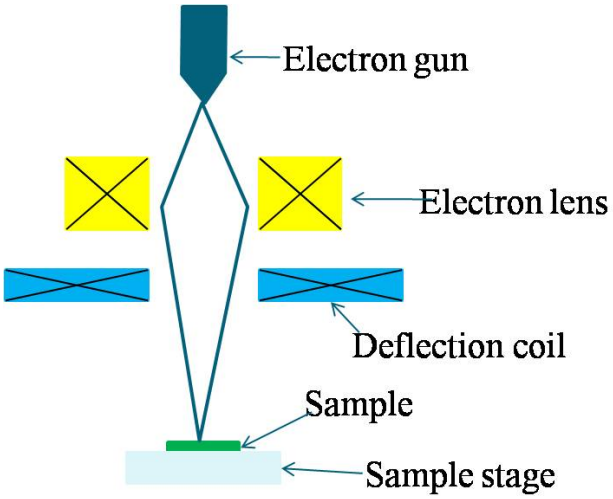

Figure 4.12: The Schematic diagram of EBL machine - the JEOL JSM-6500-F EBL system was utilized.

Fig. 4.12 shows a schematic of the major components of the EBL system. For this research, the JEOL JSM-6500-F EBL system was utilized. This system features a variable spot size ranging from 4 nm to 200 nm with vector scanning, and a step and repeat stage. The addressing resolution is 1 nm. The basic parts of the EBL system and its principle of operation are described below.

Electron sources

Lower resolution systems can use thermionic sources, which are usually formed from LaB6. However, systems with higher resolution requirements need to use field electron emission sources, such as heated W/ZrO_2 for lower energy spread and enhanced brightness. Thermal field emission sources are preferred over cold emission sources, in spite of their slightly larger beam size, because the former offer better stability over typical writing times of several hours.

Lenses

Both electrostatic and magnetic lenses may be used. However, electrostatic lenses have more aberrations and so are not used for fine focusing. There is no current mechanism to

make achromatic electron beam lenses, so extremely narrow dispersions of the electron beam energy are needed for finest focusing.

Stage, stitching and alignment

Typically, for very small beam deflections electrostatic deflection 'lenses' are used, larger beam deflections require electromagnetic scanning. Because of the inaccuracy and because of the finite number of steps in the exposure grid the writing field is of the order of 100 micrometre - 1 mm. Larger patterns require stage moves. An accurate stage is critical for stitching (tiling writing fields exactly against each other) and pattern overlay (aligning a pattern to a previously made one).

Electron beam write time

The minimum time to expose a given area for a given dose is given by the following formula:

$$Dose \times exposed\ area = \frac{beam\ current \times exposure\ time}{step\ size * 2} = \frac{}{total\ charge\ of\ incident\ electrons} \tag{4.19}$$

For example, assuming an exposure area of 1 cm^2, a dose of 10^{-3} Coulombs/cm^2, and a beam current of 10^{-9} Amperes, the resulting minimum write time would be 10^6 seconds (about 12 days). This minimum write time does not include time for the stage to move back and forth, as well as time for the beam to be blanked (blocked from the wafer during deflection), as well as time for other possible beam corrections and adjustments in the middle of writing. It is clear that throughput is a serious limitation for electron beam lithography, especially when writing dense patterns over a large area.

4.6.4 Plasma etching

Plasma etching is a form of plasma processing used to fabricate integrated circuits. It involves a high-speed stream of glow discharge (plasma) of an appropriate gas mixture being shot (in pulses) at a sample. The plasma source, known as etch species, can be either charged (ions) or neutral (atoms and radicals). During the process, the plasma will generate volatile etch products at room temperature from the chemical reactions between the elements of the material etched and the reactive species generated by the

plasma. Eventually the atoms of the shot element embed themselves at or just below the surface of the target, thus modifying the physical properties of the target.

Figure 4.13: The electron cyclotrone resonance (ECR) etching machine - apparatus ANELVA, RIB-300 was utilized.

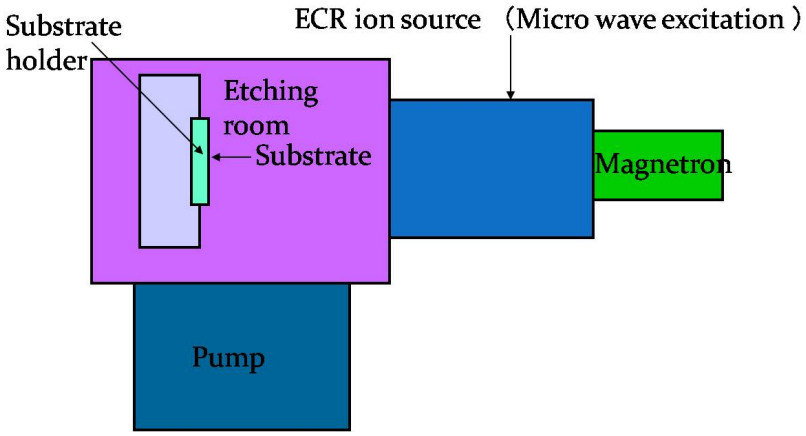

Figure 4.14: The Schematic diagram of ECR etching system - apparatus ANELVA, RIB-300 was utilized.

Fig. 4.13 and 4.14 show the electron cyclotrone resonance (ECR) etching machine and its schematic representation of the major components of the etching system. For this research, the ANELVA, RIB-300 etching system was utilized. Plasma systems ionize a variety of source gases in a vacuum system by using RF excitations. The frequency of operation of the RF power source is frequently 13.56 MHz, chosen by the Federal Communications Commission (FCC) for industrial and scientific use. Nevertheless, it can be used at lower frequencies (kilohertz) or higher (microwave). The mode of op-

eration of the plasma system will change if the operating pressure changes. Also, it is different for different structures of the reaction chamber. In the simple case, the electrode structure is symmetrical, and the sample is placed upon the grounded electrode. Free radicals such as fluorine or chlorine are created in the plasma and react at the sample surface.

Without the assistance of the plasma, much higher temperature would be required. The low processing temperature is possible because the plasma generates atoms, molecular radicals and positive ions that are more chemically reactive than the normal molecular gases from which the species are created. The key to developing successful complex etching processes is to find the appropriate gas (see Table 4.1) etch chemistry that will form volatile products with the material to be etched. For some difficult materials (such as magnetic materials), the volatility can only be obtained when the wafer temperature is increased.

Table 4.1: Etch Chemistries of Different Etch Processes - The key to developing successful complex etching processes is to find the appropriate gas etch chemistry that will form volatile products with the material to be etched.

Material Being Etched	**Etching Chemistry**
Deep Si trench	$HBr/NF_3/O_2/SF_6$
Shallow Si trench	$HBr/Cl_2/O_2$
Poly Si	$HBr/Cl_2/O_2$, HBr/O_2, BCl_3/Cl_2, SF_6
Al	BCl_3/Cl_2, $SiCl_4/Cl_2$, HBr/Cl_2
AlSiCu	$BCl_3/Cl_2/N_2$
W	SF_6 only, NF_3/Cl_2
TiW	SF_6 only
WSi2, $TiSi_2$, $CoSi_2$	CCl_2F_2/NF_3, CF_4/Cl_2, $Cl_2/N_2/C_2F_6$
Si0$_2$	CF_4/O_2, $CF_4/$**CHF**$_3$/Ar, C_2F_6, C_3F_8,C_4F_8/CO, C5F_8, CH_2F_2
Si3N4	CF_4/O_2, $CHF_3/0_2$, CH_2F_2, CH_2CHF_2

4.7 Characterization Methods

Characterization of photonic crystal properties has attracted extensive attention in the literature [16, 17, 24, 25]. The most important characteristics of photonic crystals are the band structure and spectral dependencies of transmission and reflection coefficients. One way to determine these characteristics is by solving Maxwell's equations numerically for a model structure similar to the investigated one. It could be suspected that such characterization may be inherently inaccurate, just like the theoretical calculations

of electronic band structures in solids. Luckily, this is not the case for photonic crystals. Another way is to conduct practical experiments on them. Techniques have been developed to measure the band structure properties in transmission and reflection with an off-plane incident beam. Also, direct measurement of device functionality, such as filtering and switching, has been performed. The measurement methods utilized in this thesis are Scaning Electron Microscopy (SEM) and Atomic Force Microscopy (AFM), numerical measurements utilizing FDTD method and direct observation of transmitted light from the output view of the fabricated device. Brief explanations of these methods are given below.

4.7.1 Scaning Electron Microscopy (SEM) and Atomic Force Microscopy (AFM)

The scanning electron microscope (SEM) is a type of electron microscope that images the sample surface by scanning it with a high-energy beam of electrons in a raster scan pattern. The electrons interact with the atoms that make up the sample producing signals that contain information about the sample's surface topography, composition and other properties such as electrical conductivity. Fig. 4.15 shows a picture of the SEM system used for this research.

Figure 4.15: The picture of the scanning electron microscopy (SEM) machine - used in this research.

Atomic force microscopy (AFM) or scanning force microscopy (SFM) is a very high-resolution type of scanning probe microscopy, with demonstrated resolution of fractions

of a nanometer, more than 1000 times better than the optical diffraction limit. Fig. 4.16 shows a picture of the AFM system used for this research.

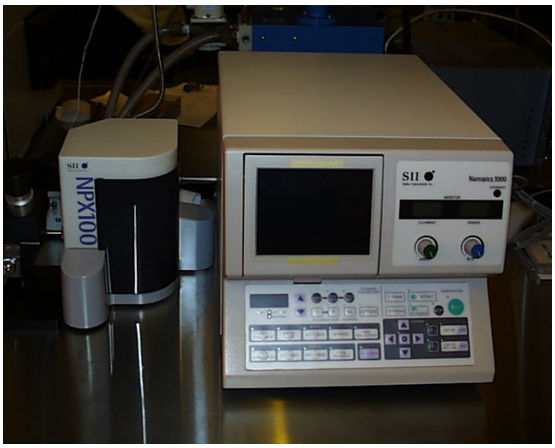

Figure 4.16: The picture of the atomic force microscopy (AFM) - used in this research.

4.7.2 Direct Beam Focusing

Fig. 4.17 shows the PhC waveguide measurement setup utilizing direct beam focus. It consists of a laser as light source (TE, TM polarization centered at 1.55 μm), single mode fiber, converging lens (focal length, F=5 mm), microscope (7×10), infrared TV (ITV) camera and control unit, and personal computer.

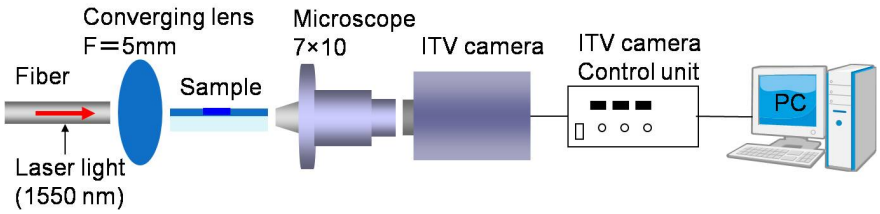

Figure 4.17: The Direct Beam Focus Experimental Setup - using 1550 nm laser source and ITV camera.

A cleaved single mode fiber carries the signals through polarization controlling paddles to the sample. A precision alignment stage with different manual adjustment axes are utilized for aligning the fiber to the sample and the microscope objective. The stage allows independent movement of the fiber and sample in addition to focusing of the microscope objective. An ITV camera images the sample through a 7x microscope objective. The output are recorded on a personal computer.

4.7.3 Numerical Characterization (FDTD)

In this subsection, we will briefly look at the overview of the transmission and reflection modeling approach in PhC waveguides. The dielectric properties of PhCs are contained in the macroscopic function $\epsilon(r)$. Under these circumstances, response of a PhC to the EM field can be found from first principles by solving Maxwell's equations. Thus, numerical modeling is in principle exact, and the accuracy of the solutions depends on the accuracy of the initial information about $\epsilon(r)$. For this reason, the power of numerical modeling in characterization of photonic crystals matches that of experimental characterization.

Two different approaches to solving Maxwell's equations are commonly used: the frequency-domain techniques, and the time-domain techniques. Frequency-domain techniques are aimed at finding the eigenstates and eigenfrequencies of the system, while disregarding the temporal evolution of the EM fields. This approach straightforwardly yields photonic bands, while transmission and reflection properties have to be calculated in an additional procedure. Time-domain techniques, in contrast, calculate temporal evolution of the input field propagating through the crystal, and disregards its frequency contents. The band structure is then obtained by Fourier transforming the fields. Therefore we will discuss the underlining mathematical principles for calculating the transmission, reflection and loss in Chapter 5 of this thesis using FDTD method.

4.8 Conclusions and Choice of Methods

After the brief overview of modeling and fabrication methods, now we discuss our choice criteria, including availability.

4.8.1 Choice of Modeling Tool

In the design process of photonic crystals considered in this thesis, two kinds of problems need to be addressed:

1. band diagrams of triangular lattice photonic crystals with 2D periodicity;

2. transmission and reflection in finite-sized photonic crystals, including their coupling to the outside world.

Propagation and coupling phenomena in finite-sized photonic crystals can be tackled by any of the methods presented, except PWEM. Besides, all these methods are on-shell frequency-domain, except FDTD. Evanescent modes are included in the analysis, and absorption or dispersion may be accounted for. Calculated transmission and reflection spectra can be related to the band structures. Moreover, one can quantify the influence of specific design parameters (number of PhC layers, PhC orientation, incidence angle).

The author has tested the available programs and selected FDTD as giving the best performance. The other methods have been found to suffer from instabilities and convergence problems already mentioned in this chapter. A self-developed code based on the modified FDTD (see Chapter 5 of this thesis) and MEEP free software (see Chapter 6 of this thesis) was used in this thesis. In author's experience, modified FDTD method proved to perform better than MEEP FDTD for 2D PhC triangular lattice band structure calculations, in terms of calculation time and memory usage. However, MEEP FDTD is well developed for waveguide analysis. Therefore, the finitesized PhC structures presented in this thesis were analyzed in 2D by Modified and MEEP FDTD methods.

4.8.2 Choice of Fabrication method

In this thesis, we introduce a novel fabrication technique that combines the characteristics of ion implantation and two-dimensional photonic crystals. From Chapter 2, we have described the ion implantation technique and its advantages. In this Chapter, we have also described the EBL and plasma etching technique for making two-dimensional structures. The details and application of the novel technique to the fabrication of novel photonic crystal waveguides will be given in Chapter 6 of this thesis.

References

[1] E. Yablonovitch, Inhibited spontaneous emission in solidstate physics and electronics, *Phys. Rev. Lett.*, vol. 58, no. 20, pp. 2059-2062, May 1987. 44, 45

[2] S. John, Strong localization of photons in certain disordered dielectric superlattices, *Phys. Rev. Lett.*, vol. 58, no. 23, pp. 2486-2489, Jun. 1987. 44, 45

[3] E. Yablonovitch. Photonic band-gap structures. J. Opt. Soc. Am. B, 10:283-296, 1993. 44

[4] J. D. Joannopoulos, R. D. Meade, and J. N. Winn, *Photonic Crystals: Molding the flow of Light*. Princeton, NJ: Princeton Univ. Press, 1995. 44, 46, 47, 51, 60

[5] S. Kittel, Introduction to Solid State Physics, John Wiley and Sons (1995). 46

[6] L. Liu and J.T. Liu, Photonic band structure in the nearly plane wave approximation, Eur. Phys. J. B, 9, 381-388, 1999. 52

[7] E. Yablonovitch and T.J. Gmitter, Donor and acceptor modes in photonic band structures, Phys. Rev. Lett., 67, 3380-3383, 1991. 52, 53

[8] T. Sondergaard and K.H. Dridi, Energy flow in photonic crystal waveguides, Phys. Rev. B, 61, 15688-15696, 2000. 52

[9] A. Mekis, J.C. Chen, I. Kurland, S. Fan, P.R. Villeneuve, and J.D. Joannopoulos, High transmission through sharp bends in photonic crystal waveguides, Phys. Rev. Lett., 77, 3787-3790, 1996. 53, 54

[10] K. Yamada, H. Morita, A. Shinya, and M. Notomi, Improved line-defect structures for photonic-crystal waveguides with high group velocity, Optics Communications, 198, pp. 395-402, 2001 55

[11] S. Noda, M. Yokoyama, M. Imada, A. Chutinan, and M. Mochizuki, Polarization mode control of two-dimensional photonic crystal laser by unit cell structure design, Science, 293, pp.1123-1125, 2001 56

[12] K. M. Leung and Y. F. Liu, Photon band structures: The plane wave method, Physical Review B, 41, pp. 10188-10190, 1990 57

[13] K. M. Leung and Y. F. Liu, Full vector wave calculation of photonic band structures in face-centered-cubic dielectric media, Physical Review Letters, 65, pp. 2646-2649, 1990 58

[14] MIT Photonic Bands, http://ab-initio.mit.edu/mpb 58

[15] Allen. Taflove, Sussan C. Hagness, Computational Electromagnetics- The finite-Difference Time-Domain Method, 3rd ed., Artech House Inc., USA, 2005, Chapter 16. Photonics. 58

[16] Miyai, E. and Sakoda, K., Quality factor for localized defect modes in a photonic crystal slab upon a low-index dielectric substrate, Optics Letters, 26, pp. 740-742, 2001 58, 67

[17] Qiu, M., Azizi, K., Karlsson, A., Swillo, M. and Jaskorzynska, B., Numerical studies of mode gaps and coupling efficiency for linedefect waveguides in two-dimensional photonic crystals, Physical Review B, 64, art. no. 155113, 2001 58, 67

[18] Loncar, M., Doll, T., Vuckovic, J. and Scherer, A., Design and fabrication of silicon photonic crystal optical waveguides, Journal of Lightwave Technology, 18, pp. 1402-1411, 2000 58

[19] K. S. Yee, Numerical solution of initial boundary value problems involving Maxwell's equation in isotropic media, *IEEE Trans. Antennas Propag.*, vol. AP-14, no. 3, pp. 302-307, May 1966. 58

[20] Hiett, B. P., Photonic Crystal Modelling using Finite Element Analysis, PhD Thesis, University of Southampton, Faculty of Engineering and Applied Science, 2002 59

[21] Pendry, J. B. and MacKinnon, A., Calculation of photon dispersion relations, Physical Review Letters, 69, pp. 2772-2775, 1992 60

[22] Pendry, J. B., Calculating photonic band structure, J. Phys.: Condens. Matter, 8, pp. 1085-1108, 1996 60

[23] E. Yablonovitch, T. J. Gmitter, and K. M. Leung, Photonic band structure: The face-centered-cubic case employing nonspherical atoms, Phys. Rev. Lett. 67, 2295 (1991). 60

[24] W. M. Robertson, G. Arjavalingham, R. D. Meade, K. D. Brommer, A. M. Rappe, and J. D. Joannopoulos, Measurement of photonic band structure in a two-dimensional periodic dielectric array, Phys. Rev. Lett. 68, 2023 (1992). 60, 67

[25] E. O zbay, A. Abeyta, G. Tuttle, M. Tringides, R. Biswas, C. T. Chan, C. M. Soukoulis, and K. M. Ho, Measurement of a three-dimensional photonic band gap in a crystal structure made of dielectric rods, Phys. Rev. B 50, 1945 (1994). 60, 67

[26] D. A. Kofke and P. G. Bolhuis, Freezing of polydisperse hard spheres, Phys. Rev. E 59, 618 (1999). 61

[27] S. Auer and D. Frenkel, Suppression of crystal nucleation in polydisperse colloids due to increase in free energy, Nature 413, 711 (2001). 61

[28] J. E. G. J. Wijnhoven and W. L. Vos, Preparation of photonic crystals made of air spheres in titania, Science 281, 802 (1998). 61

[29] A. Blanco, E. Chomski, S. Grabtchak, M. Ibisate, S. John, S. W. Leonard, C. Lopez, F. Messeguer, H. Miguez, J. P. Mondia, G. A. Ozin, O. Toader, and H. M. van Driel, Large-scale synthesis of a silicon photonic crystal with complete three-dimensional bandgap near 1.5 micrometers, Nature 405, 437 (2000). 61

[30] Y. A. Vlasov, X.-Z. Bo, J. C. Sturm, and D. J. Norris, On-chip natural assembly of silicon photonic crystals, Nature 71, 289 (2001). 61

[31] J. S. Foresi, P. R. Villeneuve, J. Ferrera, E. R. Thoen, G. Steinmeyer, S. Fan, J. D. Joannopoulos, L. C. Kimmerling, H. I. Smith, and E. P. Ippen, Photonic-bandgap microcavities in optical waveguides, Nature 390, 143 (1997). 61

[32] C. C. Cheng and A. Scherer, Fabrication of photonic band-gap crystals, J. Vac. Sci. Technol. B 13, 2696 (1995). 61

[33] T. F. Krauss, R. M. De La Rue, and S. Brand, Two-dimensional photonic bandgap structures operating at near-infrared wavelengths, Nature 383, 699 (1996). 61

[34] T. Baba and M. Koma, Possibility of InP-based 2-dimensional photonic crystal: An approach by the anodization method, Jpn. J. Appl. Phys. 34, 1405 (1995). 61

[35] H. Hatate,M. Hashimoto, H. Shirakawa, Y. Fujiwara, Y. Takeda, H. Nakano, T. Tatsuta, and O. Tsuji, Fabrication of InP submicron pillars for two-dimensional photonic crystals by reactive ion etching, Jpn. J. Appl. Phys. 37, 7172 (1998). 61

[36] S.-Y. Lin, J. G. Fleming, D. L. Hetherington, B. K. Smith, R. Biswas, K. M. Ho, M. M. Sigalas, W. Zubrzycki, S. R. Kurtz, and J. Bur, A three-dimensional photonic crystal operating at infrared wavelengths, Nature 394, 251 (1998). 62

[37] J. G. Fleming and S.-Y. Lin, Three-dimensional photonic crystal with a stop band from 1.35 to 1.95 μm, Opt. Lett. 24, 49 (1999). 62

[38] S. Noda, K. Tomoda, N. Yamamoto, and A. Chutinan, Full three-dimensional photonic bandgap crystals at near-infrared wavelengths, Science 289, 604 (2000). 62

[39] C. C. Cheng, A. Scherer, V. Arbet-Engels, and E. Yablonovitch, Lithographic band gap tuning in photonic band gap crystals, J. Vac. Sci. Technol. B 14, 4110 (1996). 62, 63

[40] O. Hanaizumi K. Ono Y. Ogawa and T. Matsumoto: Appl. Phys. Lett. Vol. 84 (2004). p. 3843 62, 63

Chapter 5

The Modified Finite-Difference Time-Domain (FDTD) Method

In this chapter we will explain the fundamentals of the FDTD Method and our modified approach for triangular lattice photonic crystals. The FDTD is an electromagnetic modeling technique generally belonging to the class of differential time-domain modeling methods [1, 2]. It is based directly on Maxwells equations which makes it very well applicable on for example photonic crystals with their sharp discontinuities of dielectric materials. As most of our later results are based on FDTD simulations, this chapter summarizes the basic concepts of FDTD with respect to its application on photonic crystal simulations.

5.1 Introduction

The Finite-Difference Time-Domain (FDTD) Method is a very general way of solving the time and space dependent Maxwell's equations using a specialized linearisation scheme. Ken Yee presented the FDTD algorithm initially in 1966 [2]. This method is used in many field of electromagnetism and covers the whole range of electro dynamical problems. The PWE method is useful for perfectly periodic materials where a small number of Fourier coefficients may be used to accurately depict both the dielectric modulation and the solution. However, many geometries of interest are not perfectly periodic and are too complex to accurately depict using a small number of Fourier coefficients. For these cases, the FDTD simulation method can be used. FDTD has the advantage of using a grid to define the material properties so sharp discontinuities can be accurately modeled compared to using a Fourier series. However, due to the use of square or cubic grids, smooth curves need to be approximated using blocks causing

a staircase effect [1]. The evolution of an EM wave is followed through discretized time steps in this finite grid.

In this chapter we will give a short overview of the basic principles and components of an FDTD simulation as well as discussing the special modifications needed for analysing photonic crystals. Additionally, we will present the modified FDTD method for triangular lattice PhCs. For further reading about FDTD and its applications we suggest e.g. [1].

5.1.1 The FDTD method and its Application to Photonic Crystals

Photonic crystals (PhCs), one, two and three dimensionally periodic materials can be used to manipulate the flow of light [3, 4, 5]. These structures provide a frequency range in which light is forbidden to propagate, thereby making them very attractive in today's information and communication technologies. To effectively model these structures, Maxwell's equations have to be numerically solved. The FDTD method, which is widely used by many researchers around the Globe, is a powerful tool for modeling photonic crystal devices. The triangular lattice is of a special interest since the structure can possess a large bandgap [6, 7, 8, 9] for transverse electric (TE) field polarization and can even possess a complete bandgap for both TE and transverse magnetic (TM) field polarization for some lattice parameters.

One of the problems of modeling a triangular lattice unit-cell PhCs using FDTD is the application of boundary conditions. The physical boundary of a triangular lattice unit-cell does not directly conform to the FDTD grid. This makes it difficult to directly enforce the desired periodic boundary conditions on the physical boundary but rather on an auxiliary boundary. Because of this problem many have proposed different methods for the application of FDTD method in a triangular lattice band structure calculations. For example: Non-orthogonal method [10]; application on the slanted boundary of the rhombus unit-cell, which is a staircased approximation of the physical boundary [1], [11]; big rectangle with double unit cell [12]. The difficulties in using these methods are well known. For example: by using the nonorthogonal mesh [10], [13], the non-rectangular unit cell can be matched quite well but a coordinate transformation is needed and more complicated formulae need to be derived, which is not easy to understand especially for the beginners in this field; the application of the boundary conditions on the slanted side of the rhombus unit-cell as in [1], [11] leads to instability, additional time-marching steps

are performed which is a waste and even difficult to implement; the use of parallelogram and split-field formulation as in [11] still uses slanted side, cannot simulate larger radius, and more so not easy to apply and only initial field value can be used to simulate the structure; the big rectangular unit-cell is easy to implement but unfortunately has a folded version of the bandgap since the unit-cell is two copies and needs to be unfolded with difficulties.

In this work, a simple and easy FDTD method, which uses small rectangular unit-cell, is presented for calculating the dispersion diagram of 2-D triangular lattice Photonic crystals. The small rectangular unit cell was reported by Yablonovitch's group in 1998 [14], [15]. However, in this work, we pesent a formulation and implementation completely different from that found in [14] and [15]. Our method is very easy for beginners in this field to understand and implement. Unlike these methods stated above, our method uses Yablonovitch's small rectangular unit-cell with translated periodic boundary conditions, which is very easy to implement in any computing environment, can simulate larger radius and initial condition or point sources can be used. The band diagram of a triangular lattice Photonic crystal is calculated by a 2-D FDTD method using our approach and compared with that of 2-D plane wave expansion (PWE) method [16, 17]. To enhance the identification of the spectral peaks, we employ Blackman window function [1], [18] on this method and show the effect on the raw spectrum. Also we carryout the convergence, accuracy, and stability analysis of our method and the requirements for using it.

5.2 The FDTD Theory

5.2.1 Basic components and Methods

In general, an FDTD-program consists of four fundamental building blocks:

- the spatial definition of the system with a distribution of dielectric or magnetic materials and the choice of a proper termination of the calculation space, the boundary conditions,
- the core algorithm that calculates the electromagnetic fields at each spatial discretisation point and timestep,
- an exciting source of some kind and

- routines for data extraction, especially when not only the fields but also derived quantities like energy are of interest.

The structures of the different building blocks are closely related to each other depending on the problem under consideration. E.g. the use of anisotropic materials requires a special form of the core algorithm, periodic (Bloch) boundaries require complex fields in all other building blocks and so on. In this section we will focus on the components that are needed to obtain the results presented in this work, but there are many variations and extensions also within the field of photonic crystals [5].

5.2.2 The Time-stepping Algorithm and the Yee Lattice

Maxwell's Equation

For linear, isotropic, nondispersive material, the general form of Maxwell's curl equations are:

$$\nabla \times \vec{E}(\vec{r},t) = -\frac{1}{c}\frac{\partial}{\partial t}\vec{H}(\vec{r},t) \tag{5.1}$$

$$\nabla \times \vec{H}(\vec{r},t) = \frac{1}{c}\epsilon(\vec{r})\frac{\partial}{\partial t}\vec{E}(\vec{r},t) \tag{5.2}$$

In Cartesian coordinates, the vector components of the curl operator yields six coupled scalar equations:

Magnetic Field components:

$$\frac{\partial H_x(\vec{r},t)}{\partial t} = \frac{\partial E_y(\vec{r},t)}{\partial z} - \frac{\partial E_z(\vec{r},t)}{\partial y} \tag{5.3}$$

$$\frac{\partial H_y(\vec{r},t)}{\partial t} = \frac{\partial E_z(\vec{r},t)}{\partial x} - \frac{\partial E_x(\vec{r},t)}{\partial z} \tag{5.4}$$

$$\frac{\partial H_z(\vec{r},t)}{\partial t} = \frac{\partial E_x(\vec{r},t)}{\partial y} - \frac{\partial E_y(\vec{r},t)}{\partial x} \tag{5.5}$$

Electric Field components:

$$\frac{\partial E_x(\vec{r},t)}{\partial t} = \frac{1}{\epsilon(\vec{r})}\left(\frac{\partial H_z(\vec{r},t)}{\partial y} - \frac{\partial H_y(\vec{r},t)}{\partial z}\right) \tag{5.6}$$

$$\frac{\partial E_y(\vec{r},t)}{\partial t} = \frac{1}{\epsilon(\vec{r})}\left(\frac{\partial H_x(\vec{r},t)}{\partial z} - \frac{\partial H_z(\vec{r},t)}{\partial x}\right) \tag{5.7}$$

$$\frac{\partial E_z(\vec{r},t)}{\partial t} = \frac{1}{\epsilon(\vec{r})}\left(\frac{\partial H_y(\vec{r},t)}{\partial x} - \frac{\partial H_x(\vec{r},t)}{\partial y}\right) \tag{5.8}$$

These equations (5.5),(5.8) form the basis of FDTD numerical algorithm for electromagnetic wave interactions with general three-dimensional objects.

The FDTD Basic Idea and Notation: Yee Algorithm

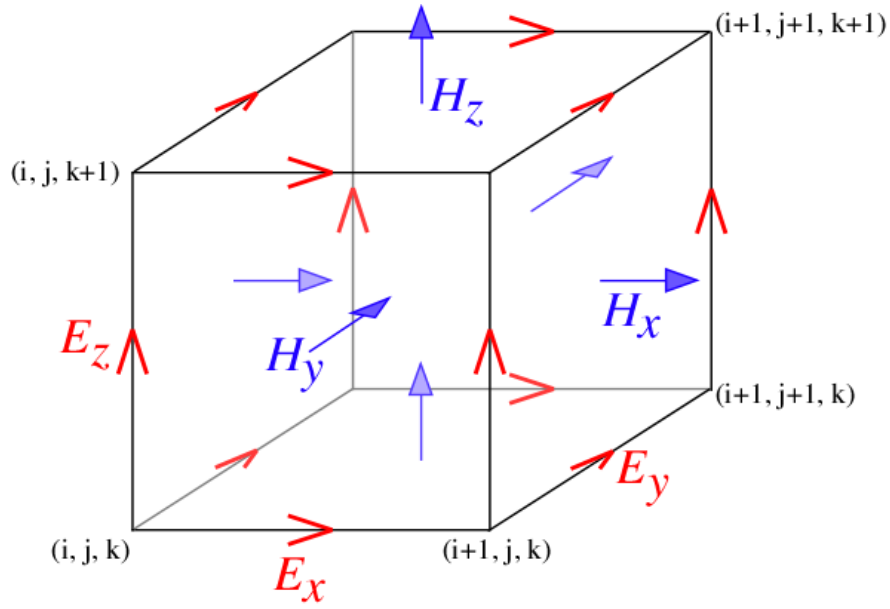

Figure 5.1: The 3-D Yee's lattice - Caption

The Yee algorithm centers its electric field (E) and magnetic field (H) components in three-dimensional space so that every H component is surrounded by four circulating E components. (See Fig. 5.1) The Yee algorithm uses central-difference in nature and second-order accurate. First, divide continuous space and time into discrete grid cells and replace spatial and temporal derivatives by finite differences on this discrete mesh. The spatial grid is defined as

$$\vec{r} = (x, y, z) \rightarrow (i\Delta x, j\Delta y, k\Delta z) \tag{5.9}$$

for the general three dimensional case and the time dimension as

$$t \rightarrow n\Delta t \tag{5.10}$$

where $i\Delta x, j\Delta y, k\Delta z$ are the discretisation stepwidths and i, j, k and n are the integer coordinates within the discrete mesh. The vector components of the fields are therefore denoted as, e.g.

$$H_x(\vec{r}, t) \rightarrow H_x|^n_{i,j,k} \tag{5.11}$$

The next step is the linearisation of the derivatives, following the scheme

$$\frac{\partial f(x = i\Delta x)}{\partial x} \rightarrow \frac{f_{i+1} - f_{i-1}}{(2\Delta x)} \tag{5.12}$$

By this approach, which is used typically in applied mathematics and numerics, the linearisation is effectively done over a $2\Delta x$-interval. All components are localised at the same position (i, j, k) in space and will result in e.g. the following update equation for H_x

$$\frac{H_x|^{n+1}_{i,j,k}}{2\Delta t} = \frac{H_x|^{n-1}_{i,j,k}}{2\Delta t} + \frac{E_y|^{n}_{i,j,k+1} - E_y|^{n}_{i,j,k-1}}{2\Delta z} - \frac{E_z|^{n}_{i,j+1,k} - E_z|^{n}_{i,j-1,k}}{2\Delta y} \tag{5.13}$$

The resulting finite difference expression of Maxwell's equations in three dimensional space are

Magnetic field components:

$$H_x|^{n+1}_{i-\frac{1}{2},j+1,k+1} = D_a|_{i-\frac{1}{2},j+1,k+1} \cdot H_x|^{n}_{i-\frac{1}{2},j+1,k+1} + D_b|_{i-\frac{1}{2},j+1,k+1} \cdot \left[\frac{E_y|^{n+\frac{1}{2}}_{i-\frac{1}{2},j+1,k+\frac{3}{2}} - E_y|^{n+\frac{1}{2}}_{i-\frac{1}{2},j+1,k+\frac{1}{2}}}{\Delta z} - \frac{E_z|^{n+\frac{1}{2}}_{i-\frac{1}{2},j+\frac{3}{2},k+1} - E_z|^{n+\frac{1}{2}}_{i-\frac{1}{2},j+\frac{1}{2},k+1}}{\Delta y} \right] \tag{5.14}$$

$$H_y|^{n+1}_{i,j+\frac{1}{2},k+1} = D_a|_{i,j+\frac{1}{2},k+1} \cdot H_y|^{n}_{i,j+\frac{1}{2},k+1} + D_b|_{i,j+\frac{1}{2},k+1} \cdot \left[\frac{E_z|^{n+\frac{1}{2}}_{i+\frac{1}{2},j+\frac{1}{2},k+1} - E_z|^{n+\frac{1}{2}}_{i-\frac{1}{2},j+\frac{1}{2},k+1}}{\Delta x} - \frac{E_x|^{n+\frac{1}{2}}_{i,j+\frac{1}{2},k+\frac{3}{2}} - E_x|^{n+\frac{1}{2}}_{i,j+\frac{1}{2},k+\frac{1}{2}}}{\Delta z} \right] \tag{5.15}$$

$$H_z|^{n+1}_{i,j+1,k+\frac{1}{2}} = D_a|_{i,j+1,k+\frac{1}{2}} \cdot H_z|^{n}_{i,j+1,k+\frac{1}{2}} + D_b|_{i,j+1,k+\frac{1}{2}} \cdot \left[\frac{E_x|^{n+\frac{1}{2}}_{i,j+\frac{3}{2},k+\frac{1}{2}} - E_x|^{n+\frac{1}{2}}_{i,j+\frac{3}{2},k+\frac{1}{2}}}{\Delta y} - \frac{E_y|^{n+\frac{1}{2}}_{i+\frac{1}{2},j+1,k+\frac{1}{2}} - E_y|^{n+\frac{1}{2}}_{i-\frac{1}{2},j+1,k+\frac{1}{2}}}{\Delta x} \right] \tag{5.16}$$

Electric field components:

$$E_x|^{n+\frac{1}{2}}_{i,j+\frac{1}{2},k+\frac{1}{2}} = C_a|_{i,j+\frac{1}{2},k+\frac{1}{2}} \cdot E_x|^{n-\frac{1}{2}}_{i,j+\frac{1}{2},k+\frac{1}{2}} + C_b|_{i,j+\frac{1}{2},k+\frac{1}{2}} \cdot \left[\frac{H_z|^{n}_{i,j+1,k+\frac{1}{2}} - H_z|^{n}_{i,j,k+\frac{1}{2}}}{\Delta y} - \frac{H_y|^{n}_{i,j+\frac{1}{2},k+1} - H_y|^{n}_{i,j+\frac{1}{2},k}}{\Delta z} \right]$$

$$E_y|^{n+\frac{1}{2}}_{i-\frac{1}{2},j+1,k+\frac{1}{2}} = C_a|_{i-\frac{1}{2},j+1,k+\frac{1}{2}} \cdot E_y|^{n-\frac{1}{2}}_{i-\frac{1}{2},j+1,k+\frac{1}{2}} + C_b|_{i-\frac{1}{2},j+1,k+\frac{1}{2}} \cdot \left[\frac{H_x|^{n}_{i-\frac{1}{2},j+1,k+1} - H_x|^{n}_{i-\frac{1}{2},j+1,k}}{\Delta z} - \frac{H_z|^{n}_{i,j+1,k+\frac{1}{2}} - H_z|^{n}_{i-1,j+1,k+\frac{1}{2}}}{\Delta x} \right]$$

$$E_z|^{n+\frac{1}{2}}_{i-\frac{1}{2},j+\frac{1}{2},k+1} = C_a|_{i-\frac{1}{2},j+\frac{1}{2},k+1} \cdot E_z|^{n-\frac{1}{2}}_{i-\frac{1}{2},j+\frac{1}{2},k+1} + C_b|_{i-\frac{1}{2},j+\frac{1}{2},k+1} \cdot \left[\frac{H_y|^n_{i,j+\frac{1}{2},k+1} - H_y|^n_{i-1,j+\frac{1}{2},k+1}}{\Delta x} - \frac{H_x|^n_{i-\frac{1}{2},j+1,k+1} - H_x|^n_{i-\frac{1}{2},j,k+1}}{\Delta y} \right] \quad (5.17)$$

where $C_a|_{i,j,k}, C_b|_{i,j,k}, D_a|_{i,j,k}$ and $D_b|_{i,j,k}$ are updating coefficients and are defined as follows:

$$\begin{aligned} C_a|_{i,j,k} &= \frac{1 - \sigma_{i,j,k} \times \Delta t/2\epsilon_{i,j,k}}{1 + \sigma_{i,j,k} \times \Delta t/2\epsilon_{i,j,k}} \\ C_b|_{i,j,k} &= \frac{\Delta t/2\epsilon_{i,j,k}}{1 + \sigma_{i,j,k} \times \Delta t/2\epsilon - i,j,k} \\ D_a|_{i,j,k} &= \frac{1 - \sigma^*_{i,j,k} \times \Delta t/2\mu_{i,j,k}}{1 + \sigma^*_{i,j,k} \times \Delta t/2\mu_{i,j,k}} \\ D_b|_{i,j,k} &= \frac{\Delta t/2\mu_{i,j,k}}{1 + \sigma^*_{i,j,k} \times \Delta t/2\mu_{i,j,k}} \end{aligned} \quad (5.18)$$

The arrangement of the shifted grids for each component is illustrated in Fig. 5.1. The field values at a new time step only depend on former values of other fields as can be seen in 5.16 and 5.17. In applied mathematics this is called an explicit scheme and is well known to be unstable in general. However, in the case of Maxwell's curl equations we can force stability by obeying the Courant condition. The accuracy of the discrete numerical scheme depends mainly on the discrete space and time steps. As a rule of thumb the smallest wavelength appearing in the calculations should be at least resolved with 12 numerical grid points.

The three-dimensional equations are further reduced to two-Dimensional Maxwell equation for transverse electric (TE) and transverse magnetic (TM) polarisation as follows

TE mode:

$$\begin{aligned} E_x|^{n+\frac{1}{2}}_{i,j+\frac{1}{2}} &= C_a|_{i,j+\frac{1}{2}} \cdot E_x|^{n-\frac{1}{2}}_{i,j+\frac{1}{2}} + C_b|_{i,j+\frac{1}{2}} \cdot \left[\frac{H_z|^n_{i,j+1} - H_z|^n_{i,j}}{\Delta y} \right] \\ E_y|^{n+\frac{1}{2}}_{i-\frac{1}{2},j+1} &= C_a|_{i-\frac{1}{2},j+1} \cdot E_y|^{n-\frac{1}{2}}_{i-\frac{1}{2},j+1} + C_b|_{i-\frac{1}{2},j+1} \cdot \left[\frac{H_z|^n_{i,j+1} - H_z|^n_{i-1,j+1}}{\Delta x} \right] \end{aligned} \quad (5.19)$$

$$H_z|^{n+1}_{i,j+1} = D_a|_{i,j+1} \cdot H_z|^n_{i,j+1} + D_b|_{i,j+1} \cdot \left[\frac{E_x|^{n+\frac{1}{2}}_{i,j+\frac{3}{2}} - E_x|^{n+\frac{1}{2}}_{i,j+\frac{3}{2}}}{\Delta y} - \frac{E_y|^{n+\frac{1}{2}}_{i+\frac{1}{2},j+1} - E_y|^{n+\frac{1}{2}}_{i-\frac{1}{2},j+1}}{\Delta x} \right] \quad (5.20)$$

TM mode:

$$H_x|^{n+1}_{i-\frac{1}{2},j+1} = D_a|_{i-\frac{1}{2},j+1} \cdot H_x|^{n}_{i-\frac{1}{2},j+1} - D_b|_{i-\frac{1}{2},j+1} \cdot \left[\frac{E_z|^{n+\frac{1}{2}}_{i-\frac{1}{2},j+\frac{3}{2}} - E_z|^{n+\frac{1}{2}}_{i-\frac{1}{2},j+\frac{1}{2}}}{\Delta y} \right] \quad (5.21)$$

$$H_y|^{n+1}_{i,j+\frac{1}{2}} = D_a|_{i,j+\frac{1}{2}} \cdot H_y|^{n}_{i,j+\frac{1}{2}} + D_b|_{i,j+\frac{1}{2}} \cdot \left[\frac{E_z|^{n+\frac{1}{2}}_{i+\frac{1}{2},j+\frac{1}{2}} - E_z|^{n+\frac{1}{2}}_{i-\frac{1}{2},j+\frac{1}{2}}}{\Delta x} \right] \quad (5.22)$$

$$E_z|^{n+\frac{1}{2}}_{i-\frac{1}{2},j+\frac{1}{2}} = C_a|_{i-\frac{1}{2},j+\frac{1}{2}} \cdot E_z|^{n-\frac{1}{2}}_{i-\frac{1}{2},j+\frac{1}{2}} + C_b|_{i-\frac{1}{2},j+\frac{1}{2}} \cdot \left[\frac{H_y|^{n}_{i,j+\frac{1}{2}} - H_y|^{n}_{i-1,j+\frac{1}{2}}}{\Delta x} - \frac{H_x|^{n}_{i-\frac{1}{2},j+1} - H_x|^{n}_{i-\frac{1}{2},j}}{\Delta y} \right] \quad (5.23)$$

The conditions for chosing $\Delta x, \Delta y, \Delta z$, and Δt are:

The FDTD algorithm requires that the time step (Δt) have a specific bound relative to the lattice space increments ($\Delta x, \Delta y, \Delta z$). This bound is necessary to avoid numerical dispersion and instability, which is an undesirable possibility with explicit differential equation solvers that can cause the computed results to spuriously increase without limit as matching-on-time iteration continues. $\Delta x, \Delta y, \Delta z$ are fixed by the need to resolve the problem geometry (less than or equal to half of the lowest wavelength, λ_{min}):

$$\Delta \leq \frac{\lambda_{min}}{2} \quad (5.24)$$

while Δt is fixed by Courant stability bound:

$$\Delta t \leq \Delta t_{max} = \frac{1}{c\sqrt{\frac{1}{(\Delta x)^2} + \frac{1}{(\Delta y)^2} + \frac{1}{(\Delta z)^2}}} \quad (5.25)$$

this in turn fixes the total number of time steps needed to complete the simulation:

$$N_{sim} = \frac{T_{sim}}{\Delta t_{max}} \quad (5.26)$$

where N_{sim}, T_{sim} are the total simulation number and timestep respectively.

5.2.3 Boundary Conditions

It is obvious that in practical calculations only a finite number of discretization points and therefore a finite space volume (and time interval) can be calculated. The consequence is that the discrete curl equations can not be applied for certain field components at the edges of the computational domain because some of the required components would lie outside and are therefore not defined. If we look e.g. in x-direction and a domain bounded by i = 0 and i = i_{max} we see that equations 5.16 are still valid because they only require well defined field values for i = 0. However, in equations 5.17 some of the components are not defined. Therefore, we have to take special care of the tangential components of the electric field at the interfaces $i, j, k = 0$ and $i, j, k = (i, j, k)_{max}+1$ to obtain a completely defined system. In the next subsections, typical boundary conditions used for the calculations in this work are shortly described.

Perfect Electric Conductor (PEC)

The simplest way of treating the tangential electric field components is to set them to zero after each time step. Mathematically this corresponds to the von Neumannboundary condition of a constant potential at the interface and physically it describes a perfectly conducting material which is approximated best in experiment by metals. Therefore we speak of metallic boundary conditions. An incoming electromagnetic wave that hits the boundary is entirely reflected back into the computational domain and no energy can escape from the system. This type of boundary does not represent the desired circumstances for most calculations. However, because of its easy implementation it is sometimes used in combination with other methods.

Periodic Boundary Condition (PBC)

For Photonic crystals, with periodicity in 1, 2, 3- dimensions, periodic boundary conditions are necessary at the physical boundaries in order to simulate the infinite structures in a finite computational domain. Therefore, the Bloch boundary condition, which is defined by:

$$\mathbf{E}(\mathbf{r}+\mathbf{R}) = \mathbf{E}(\mathbf{r})\exp(j\mathbf{k}\cdot\mathbf{R}), \tag{5.27}$$

$$\mathbf{H}(\mathbf{r}+\mathbf{R}) = \mathbf{H}(\mathbf{r})\exp(j\mathbf{k}\cdot\mathbf{R}), \tag{5.28}$$

where $j \equiv \sqrt{-1}$, $\mathbf{r}$ is the position vector, $\mathbf{R}$ is the lattice vector of the unit cell, and $\mathbf{E}$, $\mathbf{H}$ are electric and magnetic field component vectors characterized by $\mathbf{k}$ the wave vector, are applied at the edges of the computational boundary of the unit cell.

For perfectly periodic systems (which means they are infinitely extended in the direction(s) of periodicity) we know from Bloch's theorem (see Chapter 4) that the field values at equivalent positions in different unit cells only differ by a phase factor. Numerically this has the consequence that we can describe the entire infinite system by just one unit cell and apply periodic boundaries that fulfill Bloch's theorem. We illustrate this for a one dimensional system extending in x-direction and bounded by i = 0 and i = i_{max}. We know from the introduction of this section that we have to take special care of $\mathrm{E}_y|_{i=0}$, $\mathrm{E}_y|_{i=i_{max}+1}$, $\mathrm{E}_z|_{i=0}$ and $\mathrm{E}_z|_{i=i_{max}+1}$. If we assume a periodicity of length $i_{max}\Delta x$ we can relate the components at the boundaries by applying Bloch's theorem in the following way:

$$E_y|_{i=0} = \exp(+ik_x i_{max}\Delta x) \cdot E_y|_{i=i_{max}} \tag{5.29}$$

$$E_z|_{i=0} = \exp(+ik_x i_{max}\Delta x) \cdot E_z|_{i=i_{max}} \tag{5.30}$$

$$E_y|_{i=i_{max}+1} = \exp(+ik_x i_{max}\Delta x) \cdot E_y|_{i=1} \tag{5.31}$$

$$E_z|_{i=i_{max}+1} = \exp(+ik_x i_{max}\Delta x) \cdot E_z|_{i=1} \tag{5.32}$$

For the application of Bloch's theorem we have to introduce a wavevector k_x in the direction of periodicity. This is a parameter in the calculation and has to be given from the outside. The restriction to only one k-value is the price one have to pay for the benefit of limiting the computational domain to just one unit cell. Moreover, the phase factor in Bloch's theorem is complex, requiring complex electric and magnetic fields also. In practice this doubles the memory requirements of the calculation. The generalisation to three dimensions is straightforward but requires a $\vec{k}$-vector with components in all space directions.

Absorbing Boundary Conditions (ABC)

In many cases it is desirable to simulate a structure embedded in infintely extended free space because this is closest to most experimental situations. Numerically this means we have to define boundary conditions with the property that waves approaching the interfaces of the computational domain are completety absorbed without any spurious

reflection back into the system. This has to be achieved for waves of arbitrary frequency and angle of incidence. There are several propositions in literature for addressing this task like Mur's boundary conditions [19] of first and second order or perfectly matched layers (PML) invented by Berenger [20] in several variations. In this work we use the so-called uniaxial perfectly matched layers (UPML) boundary [1] in some cases and Mur's boundary conditions [19] in other cases. A short description of their fundamentals and practical implementation follows. The idea of PML boundaries is simple: We introduce a layer of a certain thickness d (in units of numerical discretization points) consisting of an artifical conducting material that absorbs incoming waves. The absorbing layer is terminated by metallic boundaries that reflect the rests of the wave entirely and the wave is damped again on its way back. Only a vanishing part of the original amplitude reenters the calculation domain. The obvious dificulty that has to be solved is that for conventional absorbing materials there would be a partial reflection at the interface between the calculation volume and the absorbing material due to impedance mismatch. We have to choose the material properties therefore in a way that there is no impedance discontinuity for any frequency and angle of incidence. It has been shown in [1] that this condition can be fulfilled for a plane wave with frequency ω by the modified frequency domain Maxwell's equations. In a three dimensional volume we have six PML-layers (two for each dimension).

5.2.4 Sources

To calculate the optical response of a dielectric structure we obviously need some kind of excitation. The choice of a proper excitation for a given problem does not follow a general guideline but strongly depends on experience. In many cases, the exspected results play an important role for the choice of the excitation. E.g. the symmetry or spatial localisation of the exspected solutions can help to selectively excite the desired field distributions. This does not mean that FDTD is not an a-priori-method. However, its general character is one major disadvantage in this respect. A solution obtained by FDTD is always reliable. However, under circumstances to be discussed more detailed later on a solution can be forgotton due to an awkward excitation, which often means it is superposed by solutions that are excited orders of magnitude stronger. In this subsection we will discuss several types of excitations. The explicit forms how they are

used in practice are given directly in the related chapters of photonic crystal applications later on.

Initial Field

A method used quite often is the assignment of the field to certain values for $t = n\Delta t = 0$. When this type of excitation is used one has to take care of the following issues: The initial field distribution must fulfill the homogenous Maxwell's equations that are not directly incorporated in the FDTD-algorithm. Especially the condition

$$\nabla \vec{H}(\vec{r}, t = 0) = 0 \tag{5.33}$$

must be fulfilled because a violation would lead to unphysical results. A violation of

$$\nabla \left[\epsilon(\vec{r}) \vec{E}(\vec{r}, t = 0) \right] = 0 \tag{5.34}$$

would physically introduce static charges that may also modify the results. Beside this physical considerations, there are also numerical ones that can influence the simulations. The initial condition will project to the solutions allowed by the system. This process takes some relaxation time. The proper choice of the initial condition can reduce this time significantly and thereby also reducing numerical noise. However, when solutions are investigated that couple only weakly to external excitations. Then a pulsed excitation with a narrow frequency spectrum around the exspected solution should be preferred.

Current Source

A very simple way of creating electromagnetic fields is the introduction of a pointlike oscillating current source at position $\vec{r}_0$ into the H-field curl equation:

$$\nabla \times \vec{H}(\vec{r}_0, t) = \epsilon(\vec{r}) \frac{\partial \vec{E}(\vec{r}_0, t)}{\partial t} + \delta(\vec{r} - \vec{r}_0) \cdot \vec{j}(t) \tag{5.35}$$

This is practically done by keeping the time-stepping algorithm unchanged and updating the corresponding electric field components after each timestep according to

$$E_x|^n_{i_0+\frac{1}{2},j_0,k_0} = E_x|^n_{i_0+\frac{1}{2},j_0,k_0} + \epsilon^{-1}|_{i_0+\frac{1}{2},j_0,k_0} \cdot j_x|^n_{i_0+\frac{1}{2},j_0,k_0} \tag{5.36}$$

e.g. for a x-polarised dipole with arbitrary temporal dependance $j_x|^n$. A proper choice for $\vec{j}(\vec{r}_0, t)$ is then e.g. a sinosoidal function with center frequency ω_0 multiplied with a Gaussian envelope of width σ.

$$\vec{j}(\vec{r}_0, t) = \delta(\vec{r} - \vec{r}_0) \cdot \vec{j}_0 \sin(\omega_0 t) \exp(-\frac{1}{2} \cdot (\frac{t - t_0}{\sigma})^2) \tag{5.37}$$

where the spectral width of the pulse around ω_0 is determined by σ^{-1}. To avoid static charges we can therefore choose a current distrubution that has either no divergence, or that is zero when integrated in time. In practice, the second condition can be easily fullfilled by adjusting the phase of the sine function

$$\vec{j}(\vec{r}_0, t) = \delta(\vec{r} - \vec{r}_0) \cdot \vec{j}_0 \sin[\omega_0 (t - t_0)] \exp(-\frac{1}{2} \cdot (\frac{t - t_0}{\sigma})^2) \tag{5.38}$$

because now we integrate over the product of a sine function that is odd with respect to t_0 with a Gaussian that is even with respect to t_0.

5.2.5 Transmission, Reflection, and Loss Modeling

In this subsection, we will explain the transmission, reflection, and loss modeling in PhC waveguides. We are therefore more interested in the power flow rather than the actual component values of the fields.

Power Flow

The energy flux at a specific time is defined by Poynting's vector,

$$\vec{S}(\vec{r}, t) = \vec{E}(\vec{r}, t) \times \vec{H}(\vec{r}, t) =$$
$$(E_y H_z - E_z H_y, E_z H_x - E_x H_z, E_x H_y - E_y H_x). \tag{5.39}$$

This is the energy per square meter propagating in the x, y and z direction, respectively. However, in this research we are interested in the transmission and reflection for specific frequencies. The field components are expressed as functions of the frequency instead of time, i.e. we take the Fourier transform of the components,

$$\vec{E}_x(\vec{r}, \omega) = \int_{-\infty}^{\infty} \vec{E}_x(\vec{r}, t) \exp^{i\omega t} \, dt \tag{5.40}$$

Numerically we are not able to integrate over infinity, therefore the Fourier transform has to be approximated for some interesting values of ω (which has to agree with the

properties of the source),

$$\vec{E}_x(\vec{r},\omega_l) = \sum_{k=1}^{N_t} \vec{E}_x(\vec{r},t_k)\exp^{i\omega_l t_k}\,\Delta t, t_k = k\Delta t \tag{5.41}$$

In the frequency domain, Poynting's vector is defined as [19],

$$\vec{S}(\vec{r},\omega) = \frac{1}{2}\vec{E}(\vec{r},\omega)\times\vec{H}^*(\vec{r},\omega) =$$
$$\frac{1}{2}(E_yH_z^* - E_zH_y^*, E_zH_x^* - E_xH_z^*, E_xH_y^* - E_yH_x^*). \tag{5.42}$$

A problem that arises here is that the electric and magnetic fields are staggered from each other. Therefore the field components are interpolated to the center of every twinkle (a twinkle is the side of a Yee cell, see chapter 4 for details). Poynting's vector describes the energy propagating in the x, y and z direction. Considering a surface S, the energy passing through that surface, the power flow, is obtained by integrating the normal component of 5.42,

$$\vec{P}_s(\omega) = \int\int_s \vec{S}(\vec{r},\omega)\cdot\hat{n}\cdot ds \tag{5.43}$$

Considering S as a square in the yz-plane (as applied in this thesis for two different values of x) the power flow $\vec{P}_y(\omega)$ becomes,

$$P_x(\omega) = \int_{z_1}^{z_2}\int_{y_1}^{y_2} S_x(\vec{r},\omega)dydz \tag{5.44}$$

numerically,

$$P_x(\omega_l) = \sum_{k_{z_1}}^{k_{z_2}}\sum_{k_{y_1}}^{k_{y_2}} S_x(\vec{r},\omega_l)\Delta y\Delta z \tag{5.45}$$

Note that power flow may be positive or negative, in difference from energy.

Transmission

The estimation of the transmission properties are conducted using a reference structure. Then we compute the power flows $P^{ref}(x_{trans})$ and $P^{ref}(x_{inc})$ for a structure where the subject of interest is not appearing in the specified problem, for example a waveguide without holes. Then we do the computations once again, with the interesting subject appearing. Now we can separate the transmission and reflection that is due

to the interesting subject (for example how the holes is affecting the transmission and reflection properties). The transmission becomes:

$$T(\omega_l) = \frac{P(x_{trans}, \omega_l)}{P^{ref}(x_{trans}, \omega_l)} \tag{5.46}$$

This is the fraction of energy that passes through an area at $x = x_{trans}$ with and without a specific subject.

Reflection

The incident wave packet should be separated from the reflection, otherwise they may cancel each other out, and information is destroyed. For simplicity, we use reference structures whenever we compute reflections. The reflection is by definition:

$$R(\omega_l) = \frac{P^{ref}(x_{inc}, \omega_l)}{P(x_{inc}, \omega_l)} \tag{5.47}$$

Loss

The loss, $L(\omega_l)$, is the part of the wave that is neither transmitted nor reflected, i.e. the part of the wave that passes the first detector and then disappear from the computational region without passing some of the detectors (probably emitted through some of the sides, making the waveguide a little bit shining). The definition is simply:

$$L(\omega_l) = 1 - T(\omega_l) - R(\omega_l). \tag{5.48}$$

5.3 The Modified FDTD Method for Triangular Lattice PhCs

5.3.1 The Triangular Unit Cell

Our focus is on the choice of unit-cell and how to easily and effectively enforce the boundary conditions on the physical boundaries of the unit-cell in the computational domain to give us the expected result that agrees with other methods. The triangular lattice consists of holes arranged in equilateral triangles of sides length a with the height. Thus the real and reciprocal space of triangular lattice in $x - y$ plane is shown in Fig. 5.2 and Fig. 5.3.

Thus the real space lattice vectors $\mathbf{a}_1$ and $\mathbf{a}_2$ in Fig. 5.2 are $\frac{a}{2}(\hat{x} + \sqrt{3}\hat{y})$ and $\frac{a}{2}(\hat{x} - \sqrt{3}\hat{y})$ respectively, where $\hat{x}, \hat{y}$ are the unit vectors in the 2-D real space lattice. The

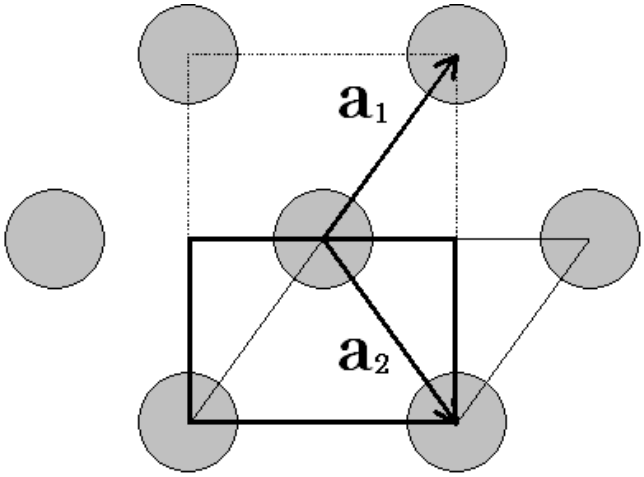

Figure 5.2: The realspace of 2-D triangular lattice - where $\mathbf{a}_1$ and $\mathbf{a}_2$ are the unit vectors for the real space lattice. The big rectangular unit cell (dotted line) has double unit-cell. The rhombus unit cell (light line) and the small rectangular unit cell (thick line) are employed in the numerical calculations.

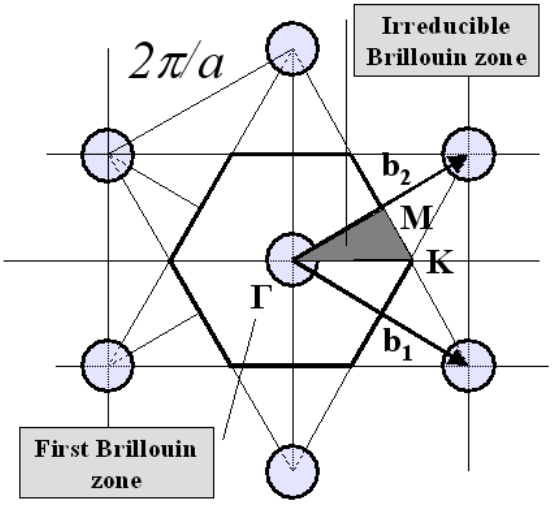

Figure 5.3: The reciprocal space of 2-D triangular lattice - where $\mathbf{b}_1$ and $\mathbf{b}_2$ are the unit vectors for the reciprocal space lattice. The enclosed hexagon is the first Brillouin zone and the shaded triangle is the irreducible Brillouin zone.

reciprocal space lattice vectors $\mathbf{b}_1$ and $\mathbf{b}_2$ in Fig. 5.3 are $\frac{2\pi}{a}(\hat{u}+\hat{v}/\sqrt{3})$ and $\frac{2\pi}{a}(\hat{u}-\hat{v}/\sqrt{3})$ respectively where $\hat{u}$ and $\hat{v}$ are the unit vectors in the reciprocal space lattice (k-space), a is the lattice constant. The hexagonal shape in Fig. 5.3 shows the first Brillouin zone of a triangular lattice and is exactly the same with hexagonal Wigner-Seitz unit cell, which is very difficult to handle numerically. As shown in Fig. 5.3, the first Brillouin zone contains some redundant points and by eliminating them, we obtain the irreducible Brillouin zone (highlighted triangle in Fig. 5.3). The vertices called the high-symmetry points have the following Cartesian coordinates: $\Gamma(0,0); M(\pi/a, \pi/\sqrt{3}a); K(4\pi/3a, 0)$ and cosequently the high-symmetry directions are: ΓM, MK and $K\Gamma$.

The rhombus unit cell depicted in Fig. 5.2 (light line) is the exact unit cell of a triangular lattice. The explanations of how to apply the boundary conditions on the slanted sides were given in [1] and [11]. The big rectangular unit cell (dotted line in Fig. 5.2) contains two unit-cells, which gives a folded version of the band diagram. We will move straight to our small rectangular unit cell (thick line in Fig. 5.2) and explain how to enforce the Bloch boundary conditions on their sides.

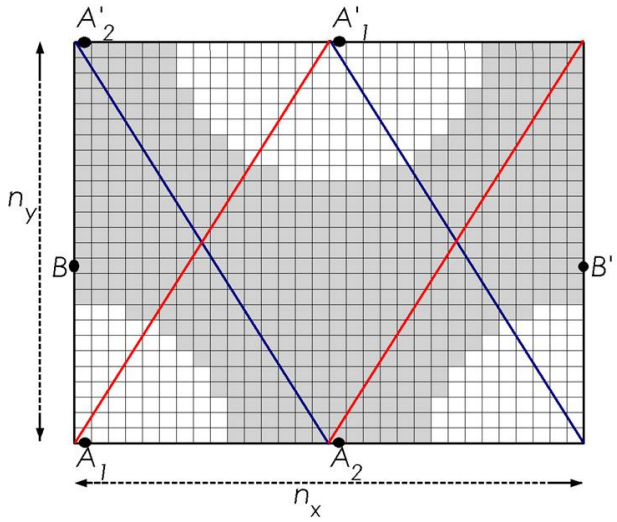

Figure 5.4: The small rectangular unit-cell of 2-D triangular lattice of airholes employed in the numerical calculation - number of grid points in $x-axis$ n_x=30, and $y-axis$ $n_y = \sqrt{3}n_x/2$ is rounded up to the nearest interger 26.

Our unit cell (smaller rectangle thick line in Fig. 5.2) also is exactly the unit cell of triangular lattice on which we can still apply the boundary conditions as shown in Fig. 5.4. The Bloch boundary conditions used along $y-axis$ are in two stages: first, by translating the first half of horizontal bottom segment of the small rectangle by $a/2$ in

positive $x-axis$ direction and $\sqrt{3}a/2$ in $y-axis$ direction (point A_1 maps onto point A_1') and second, by translating the second half of horizontal bottom segment by $a/2$ in negative $x-axis$ direction and $\sqrt{3}a/2$ in $y-axis$ direction (point A_2 maps onto point A_2') corresponding to

$$A_1' = A_1 \times \exp[-ja(k_x + \sqrt{3}k_y)/2], \; and \tag{5.49}$$

$$A_2' = A_2 \times \exp[-ja(-k_x + \sqrt{3}k_y)/2] \tag{5.50}$$

respectively. The Bloch boundary conditions used along $x-axis$ corresponds to translating the left side of the small rectangle by a (point B maps point B'),

$$B' = B \times \exp[-jak_x]. \tag{5.51}$$

The spatial step Δx and Δy are calculated in such a way that Δy is slightly less than Δx by using the following equation: $\Delta x = a/n_x$; $\Delta y = n_y/\lceil n_y/\Delta x \rceil$, where n_x and n_y are the number of grid points per lattice constant a, $\lceil \; \rceil$ is the "*ceil*" function [1] while the time step Δt will be automatically adjusted by using the Courant stability criterion (5.25).

However, it can be seen from the small rectangular unit cell (Fig. 5.4) that the Bloch boundary conditions are applied in three different directions, which is exactly the periodicity of a 2-D triangular lattice under consideration. This small rectangle is also half of the big rectangle that gives the folded version of band diagram thereby throwing more light in the reason for the folded band diagram in the dual unit-cell rectangle. Our choice of small rectangular unit-cell and the application of boundary condition approach can easily handle triangular lattice 2-D PCs on a Cartesian FDTD grid scheme.

5.3.2 The Computer Implementation

In the computational domain, the implementation of the structure shown in Fig. 5.4 can be summarized in the following discretization scheme: U is the electric and magnetic field components at the boundaries that is required for field updates, BC stands for boundary condition, p, q are integers, k_{y1} and k_{y2} are calculated as follows: $k_{y1} = (\sqrt{3}k_y + k_x)/2$ and $k_{y2} = (\sqrt{3}k_y - k_x)/2$, where k_x and k_y are the values of the wave

vectors in the reciprocal space of irreducible first Brillouin zone. These can be calculated by using the high symmetry coordinate points (ΓMK).

TE mode:

$$\begin{aligned} E_x\{p=0,1,\cdots n_x-1; q=1,2,\cdots n_y;\ \text{BC at } E_x(q=0)\} \\ E_y\{p=1,2,\cdots n_x; q=0,1,\cdots n_y-1;\ \text{BC at } E_y(p=0)\} \\ H_z\{p=0,1,\cdots n_x-1; q=0,1,\cdots n_y-1;\ \text{BC at } H_z(p=n_x; q=n_y)\} \end{aligned} \tag{5.52}$$

TM mode:

$$\begin{aligned} H_x\{p=1,2,\cdots n_x; q=0,1,\cdots n_y-1;\ \text{BC at } H_x(q=n_y)\} \\ H_y\{p=0,1,\cdots n_x-1; q=1,2,\cdots n_y;\ \text{BC at } H_y(p=n_x)\} \\ E_z\{p=1,2,\cdots n_x; q=1,2,\cdots n_y;\ \text{BC at } E_z(p=0; q=0)\} \end{aligned} \tag{5.53}$$

The Bloch boundary condition on $x-axis$ is:

$$\begin{aligned} \{for\ q=0,1,\cdots n_y\} \\ U(p=0) = U(p=n_x)\times \exp(jk_x a); \\ U(p=n_x) = U(p=0)\times \exp(-jk_x a) \end{aligned} \tag{5.54}$$

The Bloch boundary condition on $y-axis$ is in two stages:

$$\begin{aligned} \left\{for\ q=0; p=0,1,\cdots \frac{n_x}{2}-1\right\} \\ U(q=0; p=0,1,\cdots \frac{n_x}{2}-1) \\ = U(q=n_y; p=\frac{n_x}{2}, \frac{n_x}{2}+1, \cdots n_x)\times \exp(jak_{y1}) \end{aligned} \tag{5.55}$$

$$\begin{aligned} \left\{for\ q=0; p=\frac{n_x}{2}, \frac{n_x}{2}+1, \cdots n_x\right\} \\ U(q=0; p=\frac{n_x}{2}, \frac{n_x}{2}+1, \cdots n_x) \\ = U(q=n_y; p=0,1,\cdots \frac{n_x}{2}-1)\times \exp(jak_{y2}) \end{aligned} \tag{5.56}$$

$$\begin{aligned} \left\{for\ q=n_y; p=0,1,\cdots \frac{n_x}{2}-1\right\} \\ U(q=n_y; p=0,1,\cdots \frac{n_x}{2}-1) \\ = U(q=0; p=\frac{n_x}{2}, \frac{n_x}{2}+1, \ldots n_x)\times \exp(-jak_{y2}) \end{aligned} \tag{5.57}$$

$$\left\{for\ q=n_y; p=\frac{n_x}{2}, \frac{n_x}{2}+1, \cdots n_x\right\}$$

$$U(q = n_y; p = \frac{n_x}{2}, \frac{n_x}{2} + 1, \cdots n_x)$$
$$= U(q = 0; p = 0, 1, \cdots \frac{n_x}{2} - 1) \times \exp(-jak_{y1}) \quad (5.58)$$

The boundary conditions (5.52) - (5.58) are then applied using the values of k_x and k_y along the irreducible Brillouin zone. This means that the matching-on-time loop must be repeated for every wave vector k_x, k_y value along the irreducible brillouin zone directions and also observation point (or points) are placed and recorded for all time steps. These records are Fourier transformed and the peaks, which correspond to the eigen-frequencies, are then extracted and plotted as the band diagram. More so, there is need to be extremely careful of the geometric structure used since its misrepresentation can greatly affect the simulation results. The electromagnetic field at the boundary carries an important phase information and consequently, the grid point along the x-axis (n_x in this case) is required to be even (excluding the external field required for field update at the boundary, which is used only for storing boundary data). This ensures the symmetry of the geometric structure when divided into two along x-axis. It makes it easy to apply the boundary conditions diagonally otherwise we will be having longer or shorter grids at both sides and thus causes spurious data during simulations (more explainations can be found in section III). To effectively implement Bloch boundary conditions on this unit cell using our method, the lattice vectors have to satisfy $a = l_x D_x + l_y D_y$, (where l_x and l_y are integers, D_x and D_y are the vectors pointing to the neighboring Yee's grid points). This implies that this method can handle structures made up of an equilateral triangle, i.e., a_1 and a_2 vectores form angle 60^o. It is also worth noting that nonorthogonal [13] FDTD method can handle more complex structures, for example, lattice vectors a_1 and a_2 form angles other than 60^o (non-equilateral triangle). However, beginners in this field and those already having Cartesian version of FDTD can easily understand our method and quickly get started with it and can later progress toward more difficult method like that of nonorthogonal scheme.

5.4 RESULTS AND DISCUSSION

In order to demonstrate the accuracy of our method, we first calculate the band diagram of a triangular lattice 2-D PC using PWE method and also carry out calculation using FDTD method with our unit cell and boundary condition approach. Then we

compare both results. The initial parameters taken from [11] are effective refractive index n_{eff}=2.76, radius to lattice constant ration r/a=0.3.

5.4.1 Triangular Lattice Photonic crystal Band Diagram

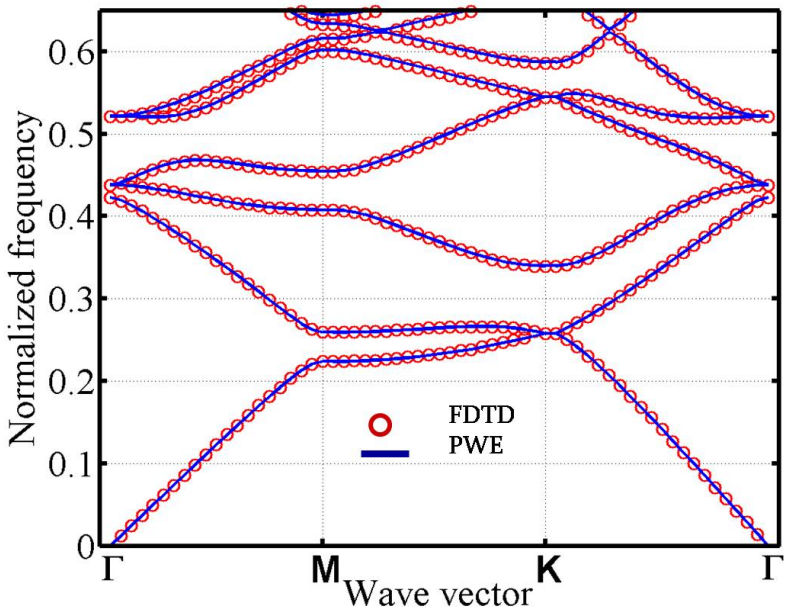

Figure 5.5: The photonic band diagram of the TM mode - for 2-D triangular lattice of airholes using the 2-D FDTD and PWE method. The effective index of 2.76 and r/a of 0.3 used here were taken from [11]. The grid point=$30/a$ and $N_{pw} = 31 \times 31$.

Fig. 5.5 and Fig. 5.6 show the TM and the TE modes band diagram of triangular lattice 2-D PhC using PWE method ($N_{pw} = 31 \times 31$) and FDTD method (grid point=$30/a$) respectively. We can see a very good agreement between two different computational methods for TM and TE field band structure of 2-D PhCs, which is a proof of the accuracy of our method. The FDTD method is shown as the open circles while the PWE method is shown as solid lines. Comparing the results of the two methods closely, we can see that there is better agreement at the lower frequency than at the higher frequency especially for the TE mode. The stair-cased grid used in FDTD discretization causes this error. However, using permittivity averaging or increasing the number of grid points per lattice constant can greatly reduce this error.

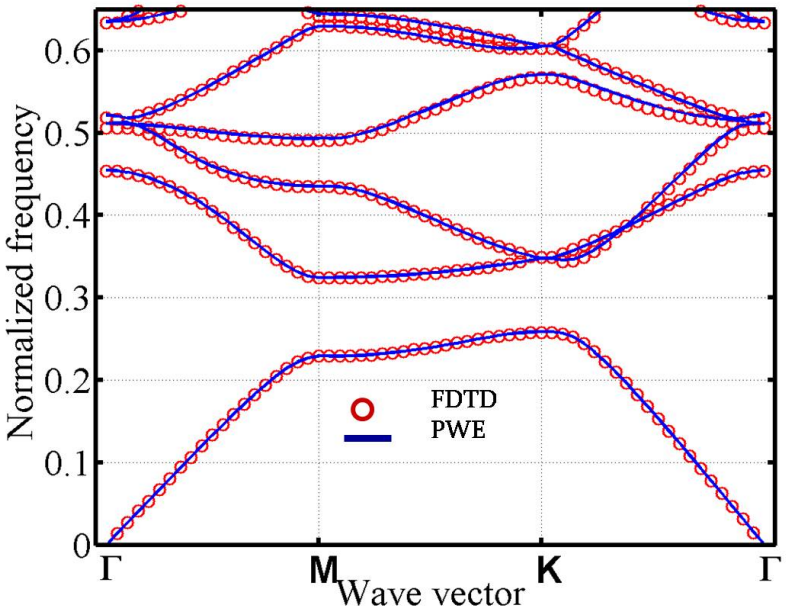

Figure 5.6: The photonic band diagram of the TE mode - for 2-D triangular lattice of airholes using the 2-D FDTD and PWE method. The effective index of 2.76 and r/a of 0.3 used here were taken from [11]. The grid point=$30/a$ and $N_{pw} = 31 \times 31$.

5.4.2 Frequency resolution

Frequency resolution is an important area in FDTD method. How many FDTD time steps are really necessary in order for our method to unambiguously identify the spectral peaks? To accurately determine the resonance frequencies, fine grid and long FDTD simulations are required. Furthermore, due to the inherently abrupt truncation of the ongoing temporal response, the raw spectrum tend to have a significant amount of ripples, as shown in Fig. 5.7 and Fig. 5.8. Here the spectral peak corresponding to the particular k point M$(\pi/a, \pi/\sqrt{3}a)$ and K$(4\pi/3a, 0)$ are shown for TE mode only. These undesirable ripples tend to complicate the indentification of spectral peaks, since the derivative of the spectrum will go through zero in many places other than at the peak. Therefore, since the main interest here is the presence and position of the spectral peaks, not their width, by multiplying the original temporal response data with a windowing function [1], [18] such as the Blackman window

$$f(t) = 0.42 - 0.5\cos\left(2\pi\frac{t}{t_{max}}\right) + 0.08\cos\left(4\pi\frac{t}{t_{max}}\right) \tag{5.59}$$

can reduce the ripples in the spectrum without significantly affecting the spectral peak position.

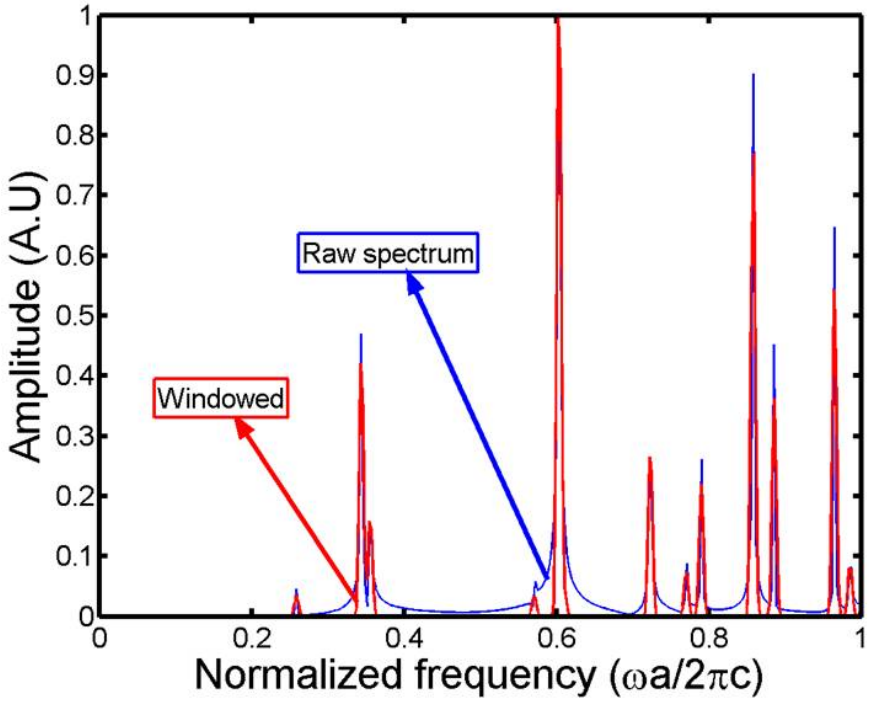

Figure 5.7: The spectral peaks for the TE mode at M point - M$(\pi/a, \pi/\sqrt{3}a)$ for 2-D triangular lattice of airholes PhC using the 2-D FDTD. The effective index = 2.76 and $r/a = 0.3$. The grid point=$30/a$.

As shown in Fig. 5.7 and Fig. 5.8, the center of these peaks, representing the normalized frequencies we want to extract to place as dots on the dispersion diagram, remain almost completely unchanged especially for the isolated peaks. We also found that the use of windowing function can significantly reduce the number of total grid points (about 144) and the total number of iterations (about 2^{14}) necessary to obtain good results especially in the area of lower bands. This is very useful in three-dimensional extension, where memory and computation time is usually huge for FDTD method.

5.4.3 Convergence, Accuracy, and Stability

The question of convergence, accuracy, and stability [21], [22] of numerical methods is extremely important if our method is to be reliable and useful. In the light of the above, we performed the TE/TM mode band calculation for an ideal triangular lattice with air holes in dielectric slab. To examine the convergence characteristics, we

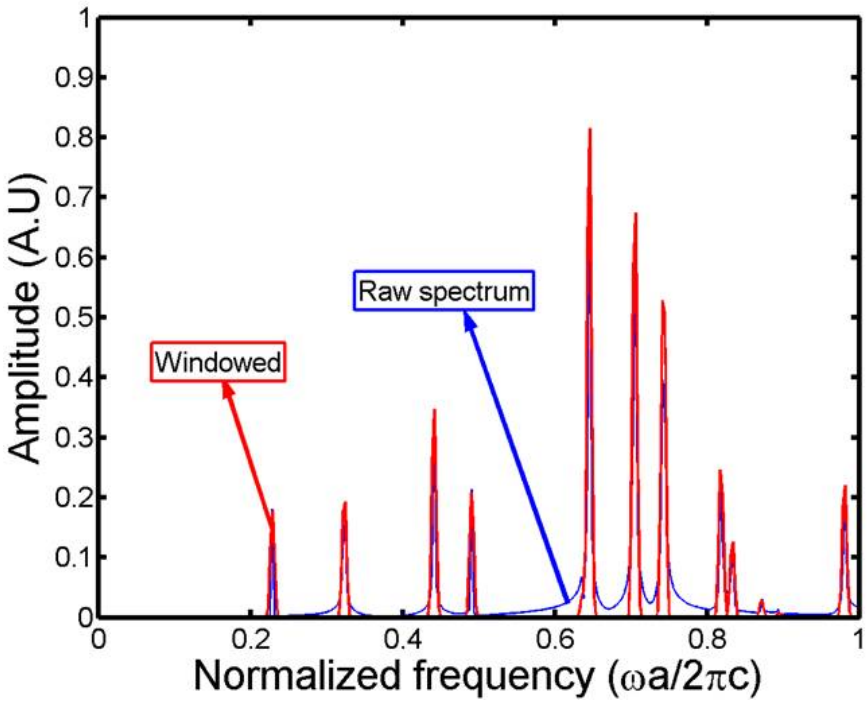

Figure 5.8: The spectral peaks for the TE mode at K point - K$(4\pi/3a, 0)$ for 2-D triangular lattice of airholes PhC using the 2-D FDTD. The effective index = 2.76 and $r/a = 0.3$. The grid point=$30/a$.

consider the k vector corresponding to the M and K point in the first Brillouin zone, i.e., M$(\pi/a, \pi/\sqrt{3}a)$; K$(4\pi/3a, 0)$. The convergent behaviors for the first to fifth bands of the TE and TM modes with the grid points from 10 to 40 stepping of 2 points and with the application of windowing function (5.59) are illustrated in Fig. 5.9, Fig. 5.10 and Fig. 5.11, Fig. 5.12 respectively. We can see that this method converges fast from the grid points per lattice constant $N > 12$.

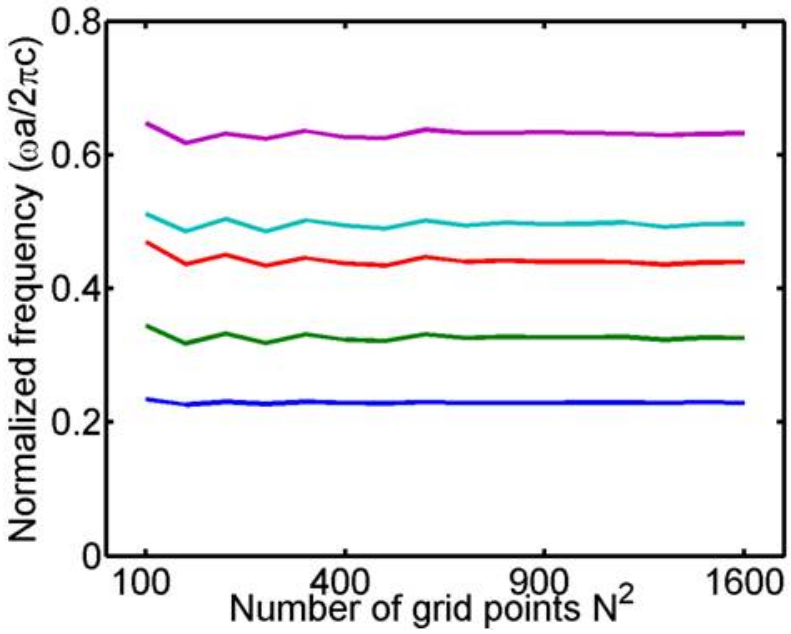

Figure 5.9: Frequency convergence for the TE mode at M point - (first to fifth bands) M$(\pi/a, \pi/\sqrt{3}a)$ for 2-D triangular lattice of airholes PhC using the 2-D FDTD. The effective index = 2.76 and $r/a = 0.3$. The grid point=10 to 40 grids per a.

Accuracy has to do with the closeness of the approximate solution(in this case FDTD) to exact solutions (in this case PWE). Fig. 5.13, Fig. 5.14 and Fig. 5.15, Fig. 5.16 show the relative errors of the first and second bands for the TE and TM modes as a function of total number of grid points N^2. The relative error (5.60) here refers to the difference of normalized frequency between the result from FDTD obtained at grid points N from 10 to 40 stepping of 2 points and the reference result from PWE obtained at high resolution plane waves $N_{pw} = 31 \times 31$.

$$Relative\ error \quad = \quad \frac{|\omega_{PWE} - \omega_{FDTD}|}{\omega_{PWE}} \tag{5.60}$$

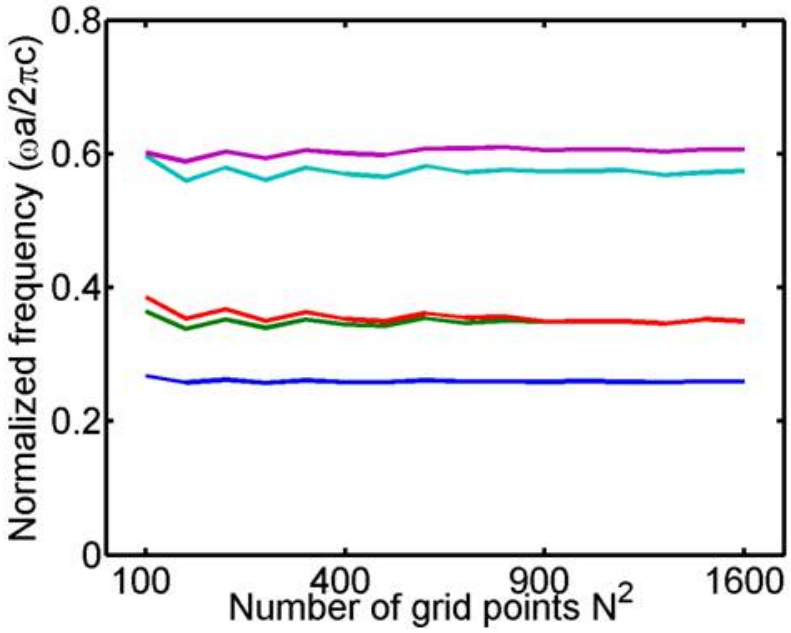

Figure 5.10: Frequency convergence for the TE mode at K point - (first to fifth bands) K$(4\pi/3a, 0)$ (bands 2 and 3 are degenerate) for 2-D triangular lattice of airholes PC using the 2-D FDTD. The effective index = 2.76 and $r/a = 0.3$. The grid point=10 to 40 grids per a.

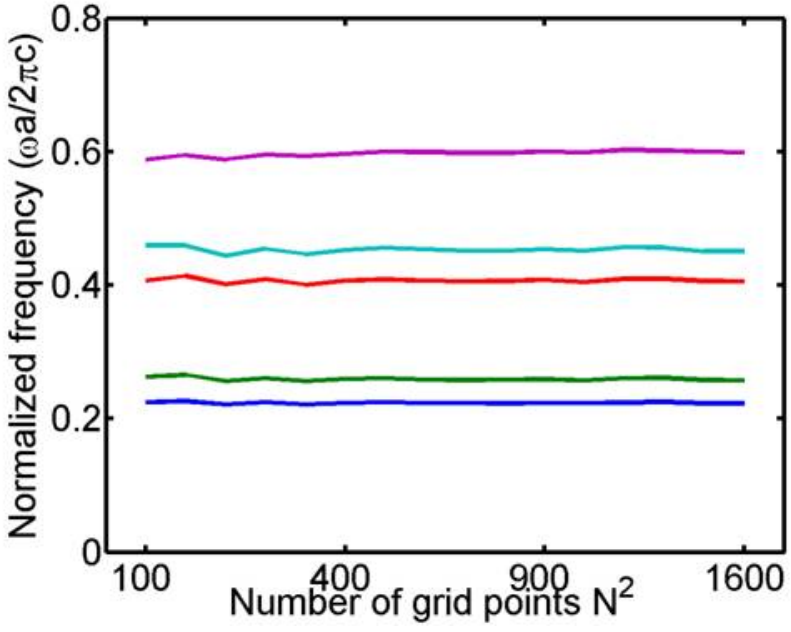

Figure 5.11: Frequency convergence for the TM mode at M point - (first to fifth bands) M$(\pi/a, \pi/\sqrt{3}a)$ for 2-D triangular lattice of airholes PhC using the 2-D FDTD. The effective index = 2.76 and $r/a = 0.3$. The grid point=10 to 40 grids per a.

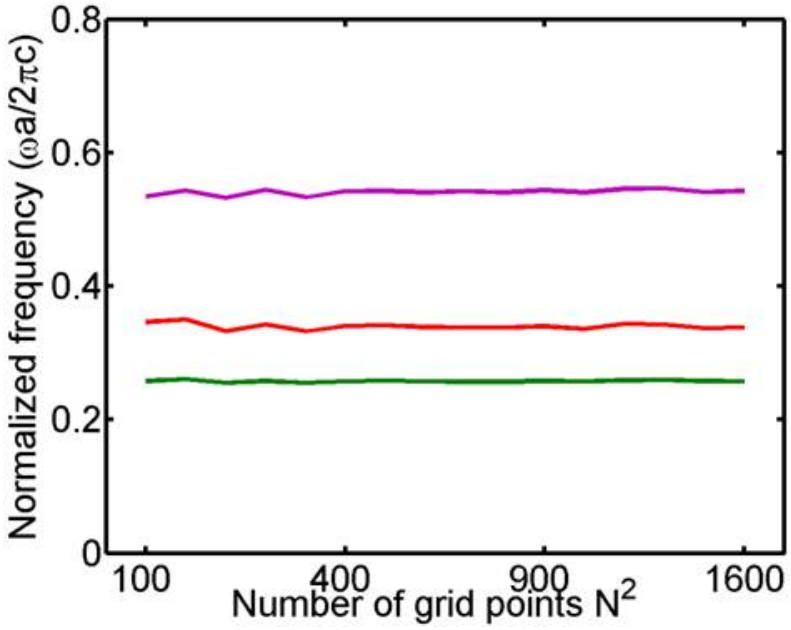

Figure 5.12: Frequency convergence for the TM mode at K point - (first to fifth bands) K$(4\pi/3a, 0)$ (bands 2 and 3 are degenerate) for 2-D triangular lattice of airholes PhC using the 2-D FDTD. The effective index = 2.76 and $r/a = 0.3$. The grid point=10 to 40 grids per a.

where ω_{PWE} and ω_{FDTD} are the normalized eigenfrequencies from PWE and FDTD methods respectively. It shows that as the number of total grid points N^2 is larger than 144, our method can achieve a relative error less than 1%. One can see the convergence property of our method is very good and preserves the second-order accuracy of the original FDTD scheme. Also we noticed in Fig. 5.14 TE mode at the K point (second and third bands) and in Fig. 5.16 TM mode also at the K point (first and second bands) and (fourth and fifth bands) are degenerate bands. Longer FDTD runs can reduce the uncertainty about having resolved all the pairs of spectral peaks, which directly follow the frequency resolution of the Fourier transform. However, there are more accurate ways than Fourier analysis to extract resonance frequencies at a shorter timesteps. Example of such method is filter-diagonalization method [23], [24].

Stability is the requirement that the scheme does not increase the magnitude of the solution with increase in time. In this regard, we found out that by using an even grid number, our method is highly stable with increase in time while odd grid number can course this method to be unstable thereby generating spurious data, i.e., the magnitude of the solution increases with time. The actual reason for this can be traced back to

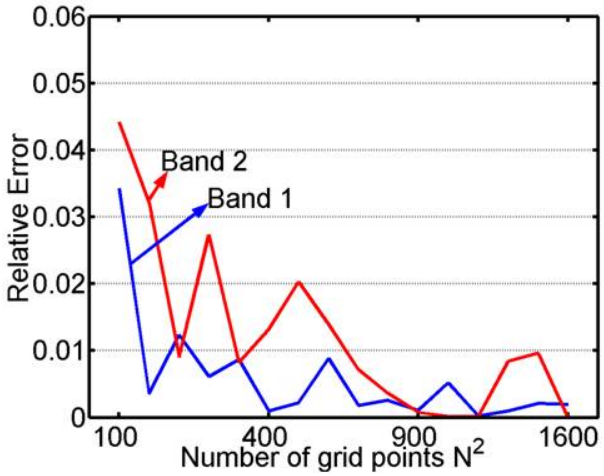

Figure 5.13: Relative error for the TE mode at M point - (5.60) (first and second bands) M($\pi/a, \pi/\sqrt{3}a$) for 2-D triangular lattice of airholes PhC using the 2-D FDTD and PWE. The grid points N =10 to 40 grids per a and $N_{pw} = 31 \times 31$.

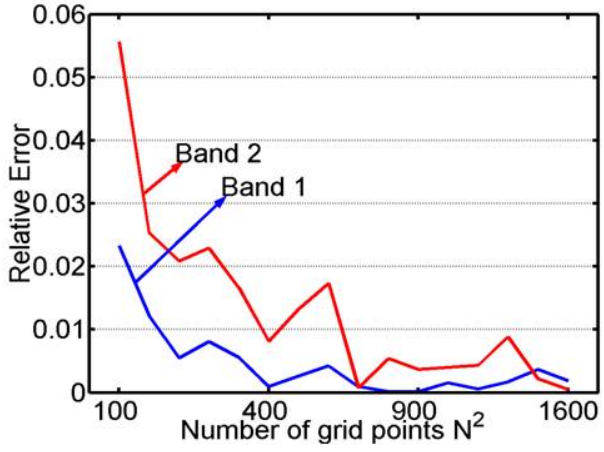

Figure 5.14: Relative error for the TE mode at K point - (5.60) (first and second bands) K($4\pi/3a, 0$) for 2-D triangular lattice of airholes PhC using the 2-D FDTD and PWE. The grid points N =10 to 40 grids per a and $N_{pw} = 31 \times 31$.

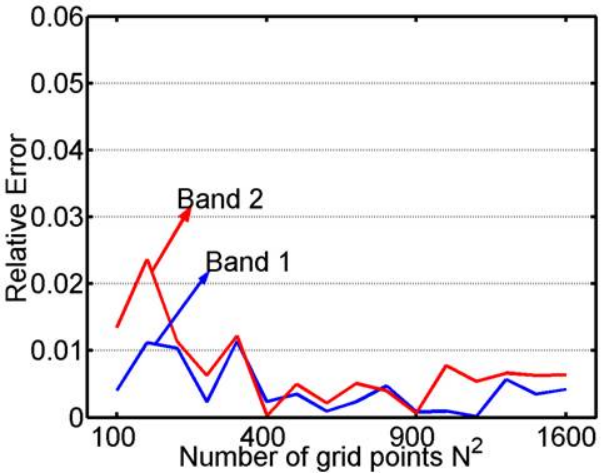

Figure 5.15: Relative error for the TM mode at M point - (5.60) (first and second bands) M$(\pi/a, \pi/\sqrt{3}a)$ for 2-D triangular lattice of airholes PhC using the 2-D FDTD and PWE. The grid point N =10 to 40 grids per a and $N_{pw} = 31 \times 31$.

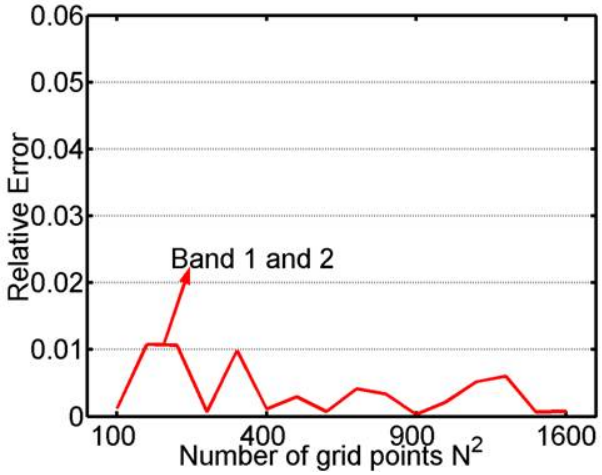

Figure 5.16: Relative error for the TM mode at K point - (5.60) (first and second bands) K$(4\pi/3a, 0)$ for 2-D triangular lattice of airholes PhC using the 2-D FDTD and PWE. The grid point N =10 to 40 grids per a and $N_{pw} = 31 \times 31$.

the definition of periodic structures [5], [1], which shows that each point in one unit cell can be mapped to another point in another unit cell by a lattice vector. The material structure remains the same while the electromagnetic wave in both points differs only by their phase shift. So by using odd grid number, this mapping becomes difficult in this unit cell and thereby causing instability during simulation. With these in mind, the user is hereby required to use even grid number.

5.5 Conclusion

In this Chapter we have discussed some basic principles of FDTD method and developed a simple and easy 2-D FDTD method for calculating the band structure of triangular lattice 2-D photonic crystals. This unit cell enables the use of Cartesian FDTD to handle general triangular lattice and our translated periodic boundary conditions can be easily applied on the physical boundaries of the unit cell. Our method provides the following advantages: simple to understand and easy to implement; utilizes minimum computation time and space; our choice of small rectangular unit cell makes it possible to use initial field or point source in the simulation and it uses exactly one unit cell thus the band diagram is accurate and not folded. The photonic band diagrams for 2-D TE and TM modes using our approach of triangular lattice photonic crystal calculated with 2-D FDTD method are in good agreement with those calculated with PWE method. Our implementation yields good convergence and accurate results. The use of windowing function such as Blackman window before the fourier transform can greatly reduce the number of grid points and total timesteps, which is very useful especially in 3-D simulation. However, a well-known disadvantage of FDTD method is that of accurately determining the resonant frequency due to the stair-casing error involved in FDTD discretization and numerical velocity error. These errors occur especially in the higher frequency (the TE is mostly affected). The staircase error can be greatly reduced by increasing the number of grid points per lattice constant or by using permittivity averaging or sub-cell method, while the numerical velocity error can be greatly reduced by compensating the velocity of light inside the medium. The 3-D FDTD method using this approach can be applied straightforward and is very easy.

References

[1] Allen. Taflove, Sussan C. Hagness, Computational Electromagnetics- The finite-Difference Time-Domain Method, 3rd ed., Artech House Inc., USA, 2005, Chapter 16. Photonics. 77, 78, 79, 87, 93, 94, 98, 106

[2] K. S. Yee, Numerical solution of initial boundary value problems involving Maxwell's equation in isotropic media, *IEEE Trans. Antennas Propag.*, vol. AP-14, no. 3, pp. 302-307, May 1966. 77

[3] E. Yablonovitch, Inhibited spontaneous emission in solidstate physics and electronics, *Phys. Rev. Lett.*, vol. 58, no. 20, pp. 2059-2062, May 1987. 78

[4] S. John, Strong localization of photons in certain disordered dielectric superlattices, *Phys. Rev. Lett.*, vol. 58, no. 23, pp. 2486-2489, Jun. 1987. 78

[5] J. D. Joannopoulos, R. D. Meade, and J. N. Winn, *Photonic Crystals: Molding the flow of Light*. Princeton, NJ: Princeton Univ. Press, 1995. 78, 80, 106

[6] S. Fan, P. R. Villeneuve, and J. D. Joannopoulos, Large omnidirectional band gaps in metallodielectric photonic crystals, *Phys. Rev. B, Condens. Matter*, vol. 54, no. 16, pp. 11245-11251, Oct. 1996. 78

[7] R. D. Meade, A. M. Rappe, K. D. Brommer, and J. D. Joannopoulos, Accurate theoretical analysis of photonic band-gap materials, *Phys. Rev. B, Condens. Matter*, vol. 48, no. 11, pp. 8434-8437, Sep. 1993. 78

[8] M. Plihal and A. A. Maradudin, Photonic band structure of two-dimensional systems: The triangular lattice, *Phys. Rev. B, Condens. Matter*, vol. 44, no. 16, pp. 8565-8571, Oct. 1991. 78

[9] P. R. Villeneuve and M. Piche, Photonic band gaps in two-dimensional square and hexagonal lattices, *Phys. Rev. B, Condens. Matter*, vol. 46, no. 8, pp. 4969-4972, Aug. 1992. 78

[10] J. F. Lee, R. Palendech, and R. Mitta, Modeling threedimensional discontinuities in waveguides using nonorthogonal FDTD algorithm, *IEEE Trans. Microw. Theory Tech.*, vol. 40, no. 2, pp. 346-352, Feb. 1992. 78

[11] W. Kuang, W. J. Kim, J. D. O'Brien, Finite-Difference Time-Domain Method for Nonorthogonal Unit-Cell Two- Dimensional Photonic Crystals, *Journal of lightwave Tech.* Vol. 25, no. 9, Sept. 2007. 78, 79, 93, 97, 98

[12] A. Chutinan and S. Noda, waveguides and Waveguide bends in two-dimensional Photonic crystal slabs, *Phys. Rev. B, Condens. Matter*, vol. 62, no. 7, pp. 4488-4492, Aug. 2000. 78

[13] A. J. Ward and J. B. Pendry, Calculating photonic green's functions using a nonorthogonal finite-difference time-domain method, *Phys. Rev. B*, vol. 58, no. 11, pp. 7252-7259, Apr. 1998. 78, 96

REFERENCES

[14] R. Coccioli, M. Boroditsky, K. W. Kim, Y. Rahmat-Samii and E. Yablonovitch, Smallest possible electromagnetic mode volume in a dielectric cavity, *IEE Proc.-Optoelectron.*, vol. 145, no. 6, Dec. 1998. 79

[15] M. Boroditsky, R. Coccioli and E. Yablonovitch, Analysis of photonic crystals for light emitting diodes using the finite-difference time-domain technique, *Photonics West 1998*, San Jose, CA, 28-29 January 1998. 79

[16] S. G. Johnson and J. D. Joannopoulos, Block-iterative frequency-domain methods for maxwell's equations in a planewave basis. *Optics Express*, vol. 8, no. 3, pp. 173-190, 2001. 79

[17] S. G. Johnson, S. Fan, A. Mekis, and J. D. Joannopoulos, Multipole-cancellation mechanism for high-q cavities in the absence of a complete photonic band gap, *Applied Physics Letters*, vol. 78, no. 22, pp. 3388-3390, 2001. 79

[18] Fredric J. Haris, On the Use of Windows for Harmonic Analysis with the Discrete Fourier Transform, *IEEE Proceedings*, vol. 66, no. 1, pp. 51-83, Jan. 1978. 79, 98

[19] G. Mur, Absorbing boundary conditions for the finite-difference approximation of the time-domain electromagnetics field equations, IEEE trans. antennas propagat. EMC-23, 377 (1981). 87

[20] J. P. Berenger, A perfectly matched layer for the absorbtion of electromagnetic waves, J. Computational Physics 114, 185 (1994). 87

[21] A. Taflove and S. C. Hagness, *Computational Electromagnetics: The finite-Difference Time-Domain Method*. Norwood, MA: Artech House, 2000. 99

[22] Shangping Guo and Sacharia Albin, Simple plane wave implementation for photonic crystal calculations, *Optics Express*, vol. 11, no. 2, pp. 167-175, Jan. 2003. 99

[23] M. R. Wall and D. Neuhauser, Extraction, through filter-diagonalization, of general quantum eigenvalues or classical normal-mode frequencies from a small number of residues or a short-time segment of a signal, *Journal of Chemical Physics*, vol. 102, no. 20, pp. 8011-8022, 1995. 103

[24] S. G. Johnson and J. D. Joannopoulos, *Photonic Crystals: the road from theory to practice*. Kluwer Academic Publishers, Norwell, MA, 2002. 103

Chapter 6

Novel Photonic Crystal Waveguides

The existence and properties of photonic bandgaps (PBG) were investigated for a triangular lattice of air holes in silicon-rich region of Si-ion implanted SiO_2 layers using finite-difference time-domain (FDTD) simulations and transport of ion in matter (TRIM) simulation software. The photonic crystal (PhC) design parameters based on the telecommunication wavelength (λ=1.55 μm) were obtained by varying the radius to lattice constant ratio (r/a) from 0.2 to 0.45. We analyzed both transverse electric (TE) and transverse magnetic (TM) mode propagation in triangular-lattice PCs. The result obtained shows that a PC bandgap (PBG) exists for TE-mode propagation in the Si-ion implanted SiO_2 patterned 2-D triangular lattice of air holes. We have also calculated the dispersion relations for the TE mode of a line defect in the structure. Based on the simulated parameters, we designed and fabricated two-dimensional photonic crystal (2-D PhC) consisting of the Si-ion implanted SiO_2 layers. By analyzing the fabricated samples using different fabrication approaches, we found a suitable fabrication method for 2-D PhCs based on the Si-ion implanted SiO_2 layers. We have analyzed the fabricated sample using atomic force microscope (AFM) and scanning electron microscopy (SEM). The annealing temperature and time were optimized in order to recover the damage done by Si-ion implantation. Finally, the transmission and reflection properties of a straight line and two 60-degree bend waveguides were characterized experimentally using direct beam focus and numerically using FDTD method.

6.1 Introduction

Silicon based photonic crystal [1, 2, 3] structures for manipulating the flow of light has attracted much attention to many researchers all over the world due to their compatibility with the existing silicon technology. To be able to have a full control of light in all directions, a three-dimensional photonic crystal (3-D PhC) structure is required. However, the fabrication of 3-D PhC structures is still a difficult process, which has resulted in using 2-D PhC to confine light in the lateral directions by PhC bandgap and using different method to confine light in the vertical direction. Many approaches have been reported in this area [4, 5, 6]. Example of such method is the use of dielectric slab, which uses total internal reflection technique to confine light in the vertical direction. The integration of such structures into the existing silicon technology constitutes problem because their methods of fabrication are not compatible with the existing silicon technology.

One of the most promising approaches to producing 3-D waveguide structures, compatible with conventional microelectronic processing, may be ion implantation [7, 8] and subsequent process of 2-D PhC on them by electron beam (EB) lithography. Especially of interest is the PhC consisting of triangular lattice of air-holes because this structure possesses a large bandgap for TE mode and air-holes are easy to handle during fabrication. As well known, high-density planar photonic integrated circuits can be realized by using sharp-bended 2-D PhC waveguides [9]. A large spot size and lower scattering loss can additionally be obtained by utilizing its gentle refractive-index distribution produced in the SiO_2 layer by Si-ion implantation than previous studies on various 2-D PhC waveguides conducted by other groups. Also by using air-holes instead of dielectric cylinder, we can obtain the mechanism for low-loss vertical confinement of the light within the waveguide at optical frequencies [6].

In this chapter, we develop the design and fabrication of a new type of 2-D PhC waveguide. A Si-ion-implanted SiO_2 layer is used as a base material of this structure. Novel photonic crystal waveguides are designed by combining the Si-ion implantation technique and the characteristics of 2-D photonic crystals. Therefore, we will explain the proposed model, and how they are realized from simulation through fabrication and characterization. We will then explain how this method can be used to completely control light in three dimensions. The design parameters such as the lattice constant

(a), the radius of air-holes (r) are estimated using the modified finite-difference time-domain (FDTD) method [10] to work at a wavelength λ=1.55 μm applicable to optical fiber communication systems. We analyzed two different approaches for the fabrication and propose a new fabrication method to define the PhC structures in the Si-ion implanted SiO_2 layers. We also analyzed the fabricated samples using atomic force microscope (AFM) and the results shown are in good agreement with the simulated design parameters from the FDTD. The attempt to characterize the fabricated sample experimentally are shown. However, because of the difficulty in coupling light into this structure, FDTD characterization will be used more fully. To conclude this chapter, we will briefly discuss the various applications and benefit of using this method of approach to guide light in 2-D photonic crystal structures.

6.1.1 The Proposed Waveguide Model

We are trying to realize a new type of 2-D PhC waveguide that incorporates the Si-ion implantation into SiO_2 layers (see Fig. 6.1) and the characteristics of 2-D PhCs. This approach is very promising to producing 3-D waveguide structures compatible with conventional microelectronic processing. The schematic model of Si-ion implantation into SiO_2 layers is shown in Fig. 6.1. The implantation energy and dose are 80 KeV and 1×10^{17} ions/cm^2, respectively.

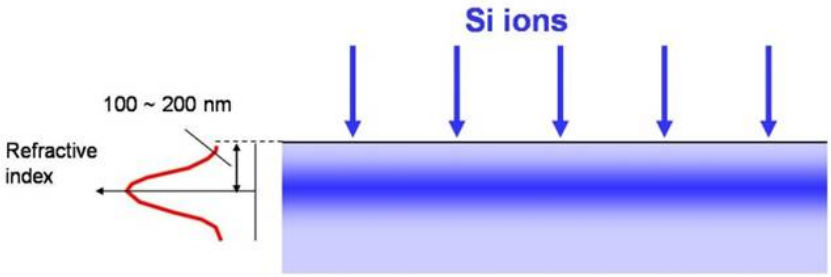

Figure 6.1: The schematic model of Si-ion implantation into SiO_2 layers - implantation energy and dose are 80 KeV and 1×10^{17} ions/cm^2, respectively.

Fig. 6.2 shows a schematic model of a PhC waveguide consisting of an Si-ion implanted SiO_2 substrate. The structure is made up of the core layer and the cladding. The core layer consists of a high-index Si-rich region due to Si-ion implantation and subsequent annealing, while the cladding layer consists of a low-index SiO_2 substrate on

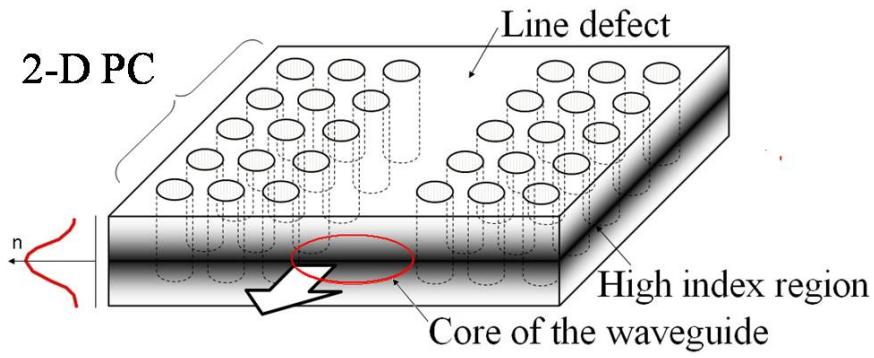

Figure 6.2: Schematic representation of a PC line-defect waveguide - waveguide consisting of Si-ion implanted SiO_2 substrate.

the vertical direction and PhC cladding (triangular lattice of air holes with line defect) on the lateral directions. The thickness and position of the core layer can be controlled by changing the implantation energy, while the refractive index of the core layer can be controlled by changing the implantation dose and choosing appropriate annealing temperature and time. The PhC cladding parameters are determined theoretically by FDTD simulations and experimentally by EBL and etching parameters. Accurately determining the refractive index of the core layer can be very complicated. L. Pavesi et al. [7] estimated the effective refractive index of the Si-rich region (implantation dose = 1×10^{17} ions/cm^2, implantation energy = 80 keV) to be n_{eff}=1.89. A PhC consisting of a triangular lattice of air holes is of great interest because this structure possesses a large PBG for the TE mode and air holes are easy to handle during fabrication. The waveguide can be obtained by introducing a line defect in the structure; that is by removing a line of air holes.

The S-ion implantation technique has many benefits. Firstly, this technique is compatible with the current Si-technology, thereby making it easy and possible to integrate Si-based optoelectronic components into the existing Si-technology. Secondly, it has the advantage that a given number of ions can be placed at a controlled depth and distribution by changing the ion dose and acceleration energy, which may enable the integration of optical functionalities such as lasers, waveguides, sensors, etc, into the existing silicon chips. Finally, ion-beam synthesis of Si-ncs is a potential candidate for manufacturing chemically stable and pure Si-ncs for fundamental research and applications in monolithically integrated Si-based optoelectronic devices. Therefore, we will procceed to the design and analysis of PhCs based on this model.

6.2 The Design and Analysis

In this section, we show the theoretical analyses of Si-ion implanted SiO_2 (1×10^{17} ions/cm^2, 80 keV) for use in the fabrication of photonic crystals. The transport of ions in matter (TRIM) [11] software was utilized to find the implantation profile predictions, while a modified FDTD method [10] was utilized to find the PC design parameters such as the lattice constant (a), the radius to lattice constant ration (r/a), and the slab thickness (h) for the wavelength of interest (1550 nm). Finally we design the partterns for fabrication using VectorWorks software.

6.2.1 TRIM Simulations and Analysis

The computer code [11] was applied to estimate the optimal conditions of several assumed parameters upon ion energies and doses for the ion implantation processing. In addition, entered ion types, target elements, target density and energy range, and the projected distance could be calculated.

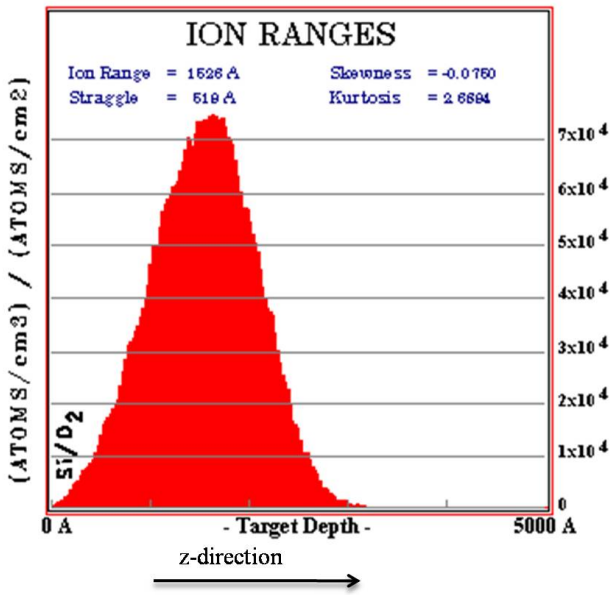

Figure 6.3: The TRIM prediction of Si-ion implantation into SiO_2 layers profile - implantation energy and dose are 80 KeV and 1×10^{17} ions/cm^2, respectively.

According to the different energies (see Fig. 2.8 in Chapter 2 for details), the calculations for Si-ion distribution in SiO_2 layer, the ion with higher energy has stronger implanting capability, that is, the penetrating depth of ions enlarges with the increasing

implanting energy. In Fig. 6.3 we show the implantation energy of 80 KeV and dose of 1×10^{17} ions/cm^2, which we use in our PhC waveguide fabrication. The calculations demonstrate that the mean projected depth (Rp) reaches about 100 - 150 nm. The straggling distance is at the range of 50 - 100 nm in the longitudinal range and the lateral projected range is about 94 - 116 nm. The effect of surface modification on the material surface is obvious, while the chaotic status of projected and/or scattered ions is increased.

6.2.2 The FDTD Simulations and Analysis

In this subsection we apply the FDTD method already discussed in Chapter 5 of this thesis. We employ Yee's FDTD formular (5.17) discussed in Chapter 5. In order to simulate the infinite periodic structures in a finite computational domain, the Bloch boundary conditions (5.27) and (5.28), are applied at the edges of the computational boundary of the unit cell [10]. More details of the FDTD algorithm are discussed in Chapter 5. In order to design a PhC waveguide structure, we need to choose a crystal geometry that provides a PhC bandgap. We should also choose a geometry that is relatively easy to fabricate at micron-level dimensions. Therefore, we will simulate the triangular lattice PhC gapmap based on the effective index of 1.89 and the working wavelength of interest λ=1.55 μm.

Fig. 5.3 (in Chapter 5) shows the reciprocal space of triangular lattice of air-holes and Fig. 6.4 shows its computational domain unit-cell respectively. The vertices of the irreducible Brillouin zone called the high-symmetry points have the following Cartesian coordinates: $\Gamma(0;0)$; $M(\pi/a;\pi/\sqrt{(}3)a)$; $K(4\pi/3a;0)$.

The photonic crystals are periodic structures, so naturally a single unit cell (Fig. 6.4) will be analyzed by applying appropriate periodic boundary conditions (more details about the unit-cell can be found in chapter 5 of this thesis). The computational domain contains 30×26 grid points (see Fig. 6.4; a is the lattice constant and r is the radius of air-holes). The FDTD analyses are carried out by applying Bloch periodic boundary conditions 5.27 and 5.28 in the x- and y-directions along the high symmetry points and by changing the value of radius to lattice constant ratio r/a from 0.2 to 0.45. When Bloch periodic boundary conditions are applied, the electromagnetic field will reach a steady state after some time and its spectrum, which contains peaks at frequency values corresponding to the eigenmodes compatible with the wave vector $\mathbf{k}$ chosen to

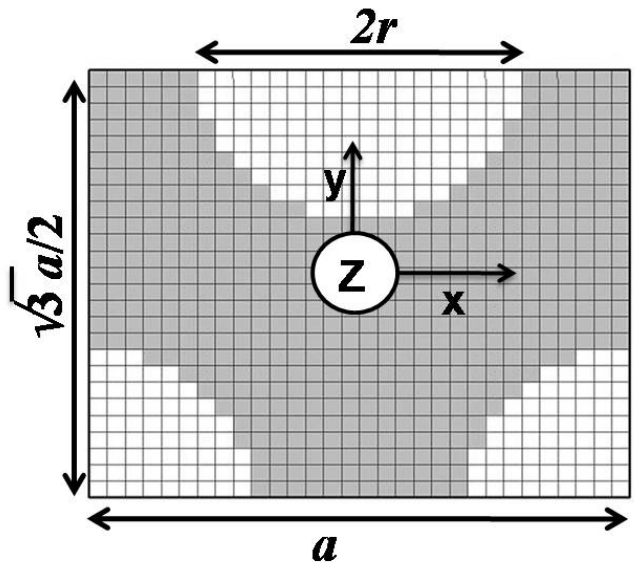

Figure 6.4: The triangular lattice unit cell model - computational domain unit-cell (30×26) is taken from [10].

enforce the periodic boundary conditions, could be obtained via Fourier transform. We will consider both the TE and TM mode in the triangular lattice and show that only triangular lattice TE-mode possesses a PBG suitable for PC waveguide design and fabrication.

PBG Analysis

By using the FDTD algorithm discussed in Chapter 5 and changing the radius to lattice constant ratio (r/a), we simulated the TE-mode gap map of triangular lattice PhCs as shown in Fig. 6.5. The normalized frequency ($\omega a/2\pi c{=}a/\lambda$) is plotted against the radius to lattice ratio (r/a), where $\omega{=}2\pi c/\lambda$ and c is the speed of light in vacuum. Here we have shown the first two bands (1 and 2) of TE-mode and especially we focused on the band 2 of M-point and band 1 of K-point in this analysis. As we can see from the figure, a very small band gap appears as the r/a ratio increases above 0.22 between band 1(K-point) and band 2(M-point).

From this analysis, it is obvious that the TE mode triangular lattice possesses a PC bandgap. It is worth noting firstly, that the increase of the TE-mode band gap as r/a ratio increases is the consequence of the ready decrease of the average dielectric constant ($\epsilon{=}n^2$) of the medium [3] and secondly, the band gap width becomes wider

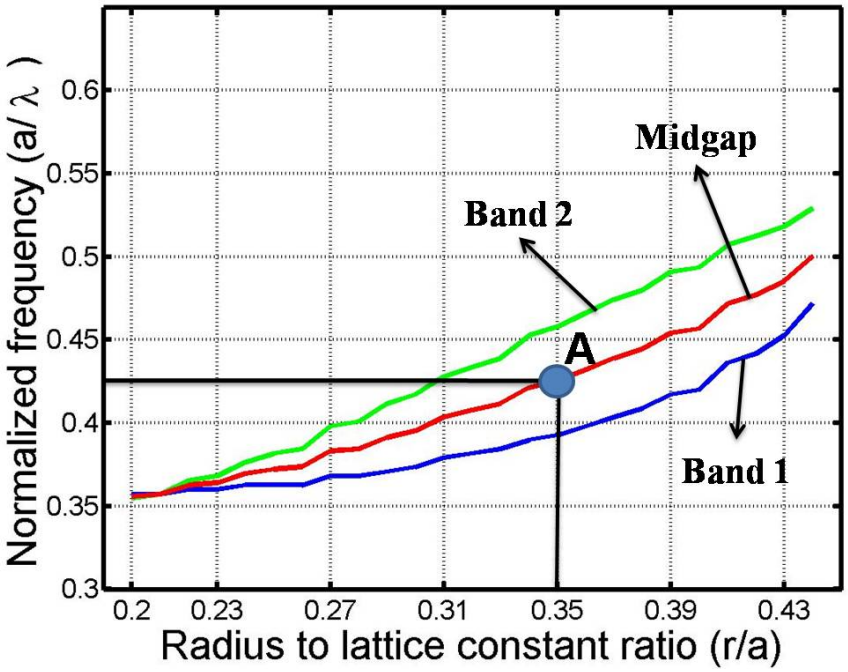

Figure 6.5: 2D Photonic bandgap map - for 2-D triangular lattice of air-holes PCs using the 2-D FDTD method. The effective index is 1.89 and r/a ratio is changed from 0.2 to 0.45., λ=1.55 μm, design point at midgap **A**(a/λ=0.43,r/a=0.35) with gap (0.39 to 0.46) is used.

with the increase of r/a ratio. These are consistent with the gap-map regularities of conventional PhCs with air columns in dielectric [3]. These also indicate that the Si-rich region formed in Si-ion implanted SiO_2 substrate plays a key role in the photonic band structure, for the r/a ratio is mainly controlled by EBL parameters.

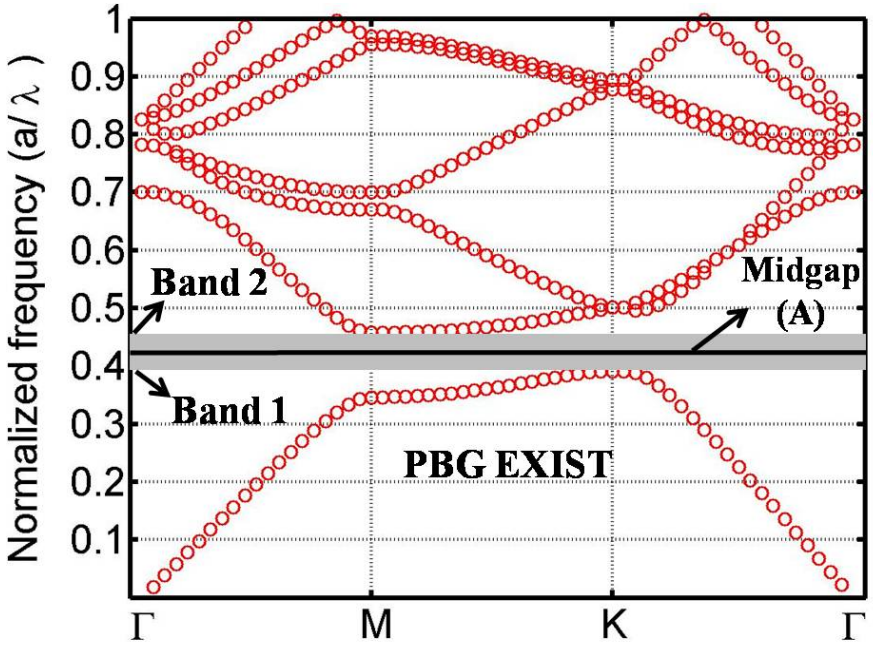

Figure 6.6: Photonic band diagram of the TE polarization - for 2-D triangular lattice of air-holes using the 2-D FDTD method. The effective index is 1.89 and r/a=0.35. The gap (band1=0.39 - band2=0.46) to midgap (0.43) ratio in this configuration is 16%, λ=1.55 μm.

The TM mode triangular lattice and TE/TM mode square lattice of air-holes do not possess PBG in this configuration, so the analyses are not shown, however, we have shown the band diagram of TM mode (Fig. 6.7) based on the fabrication point of choice for reference purpose only. Therefore, TM mode triangular lattice and TE/TM mode square lattices of air-holes are not suitable for our application. From the TE mode analysis figure (Fig. 6.5), we chose the fabrication point (**A** in Fig. 6.5) with parameters that is relatively easy to fabricate at micron-level dimensions and located in the non-leaky region. We have chosen our design point with the parameters r/a=0.35 and the normalized frequency (ω_m) at the midgap (ω_m)=a/λ=0.43 for the purpose of PC fabrication. We then calculate the remaining parameters a=$\omega_m\lambda$=0.664 μm, r=0.35a=0.232 μm and simulate the full band diagram for these parameters using

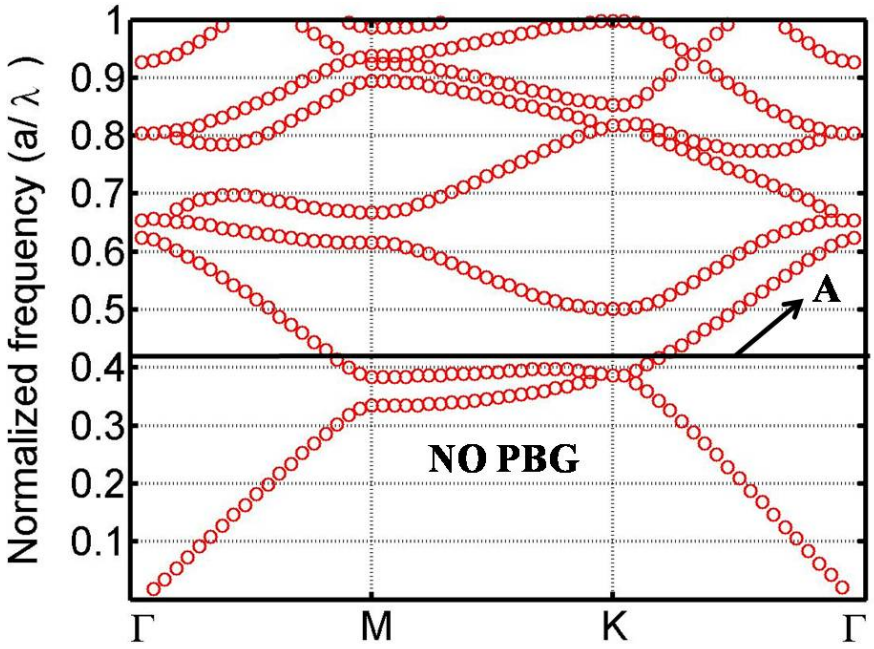

Figure 6.7: Photonic band diagram of the TM polarization - for 2-D triangular lattice of air-holes using the 2-D FDTD method. The effective index is 1.89 and r/a=0.35, λ=1.55 μm. There is no gap in this configuration.

FDTD as shown in fig. 6.6. The gap exists from normalized frequency 0.39 (band 1) to 0.46 (band 2) $[2\pi c/a]$. The gap to midgap ratio is 16%.

Defect modes in the triangular lattice PC waveguide.

Here, we create a line defect (a single line waveguide) by removing a row of air-holes in the x direction. Of prime significance in the design of ion implanted PC waveguide is an accurate knowledge of the waveguide parameters. These include the depth profile, core layer thickness and refractive index, the cladding layer index, lattice constant, and radius of holes, that will give us a bandgap centered around interesting wavelength. By using equation (4.18), W_{tri}=0.686 μm and applying Bloch periodic boundary conditions (5.27) and (5.28) in the x and absorbing boundary conditions in y directions, we calculated the band diagram of the triangular lattice PC waveguide and analyzed the TE defect mode.

Fig. 6.8 shows the result from FDTD simulations of TE mode triangular lattice PC waveguide band diagram. The real space triangular lattice with line defect used in this calculation is shown as the left inset in Fig. 6.8. The right inset in Fig. 6.8 shows the

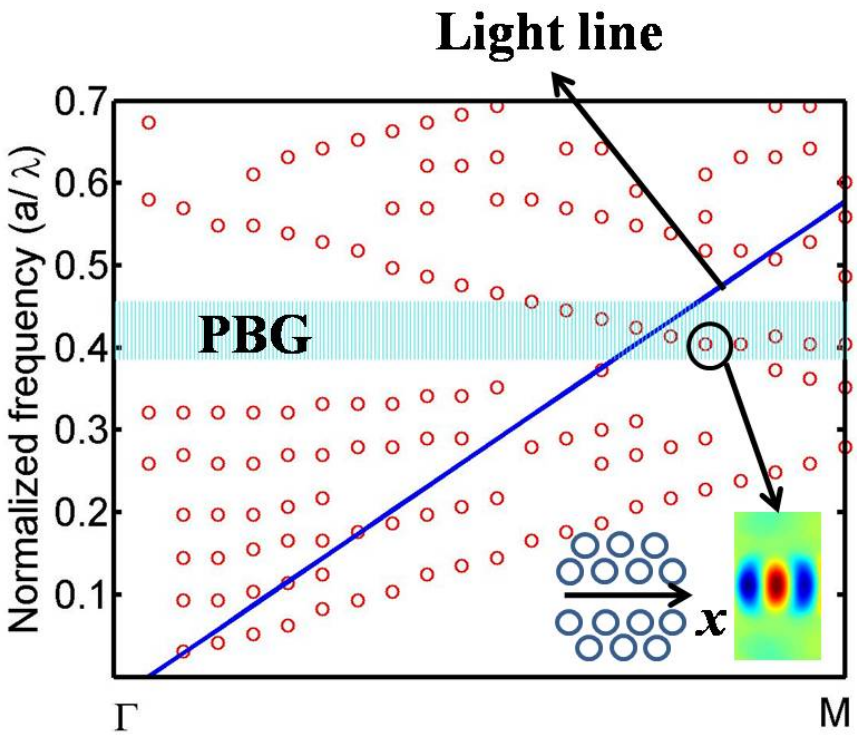

Figure 6.8: The band diagram of TE line defect mode - for 2-D triangular lattice of air-holes using the 2-D FDTD method. The effective index is 1.89 and r/a=0.35. The gap (band1=0.39 - band2=0.46), λ=1.55 μm.

fundamental mode field pattern of TE polarization (y-component of the electric field (E_y) in x-direction). This band diagram indicates the electromagnetic states that are localized in the crystal. The dark solid line shows the light line (above the PC) above which, every mode is leaky, while below it, every mode is non-leaky. In our design, since the Si-rich region is located inside the SiO_2 after the Si-ion implantation, we have chosen the mode inside the SiO_2 cladding for a non-leaky mode. Since the frequency of the guided mode lies within the PBG, the mode is forbidden to escape into the crystal. From this analysis, it is obvious that the TE mode triangular lattice with the PC bandgap can effectively guide light in the crystal. Therefore, we utilize these parameters to fabricate novel PC waveguide structures for integration into optoelectronic components and devices.

6.2.3 The Parttern Design and Analysis

Fig. 6.9 shows the schematic of the designed pattern of PhC waveguide. The core layer consists of high-index Si-rich region due to Si-ion implantation and subsequent annealing, while the cladding layer consist of low-index SiO_2 substrate. The thickness and position of the core layer can be controlled by changing the implantation energy, while the refractive index of the core layer can be controlled by the implantation dose and appropriate annealing temperature and time. The waveguide channels were composed of line and bend defects in the PhC with air-holes filled.

We designed line defects and 60^o bends in a waveguide pattern as shown in Fig. 6.9 using Vectorworks software (version 12). By using the TRIM 2008 simulation software [11], we estimated the depth of the high-index Si-rich region from the surface to be ≈100-200 nm. The designed lattice constant (a) and radius of air-holes (r) are 0.664 μm and 0.232 μm respectively. The design parameters were simulated using the method in [10] assuming the infinite height of the structure and an effective refractive index n_{eff}=1.89 [7] of the guided mode and working wavelength of λ=1.55 μm. The photonic bandgap was found to exist from normalized frequency of 0.39 to 0.46 [$2\pi c/a$] in the TE-mode triangular lattice PhC structure and the gap to midgap ratio was found to be 16%. However, there was no photonic bandgap in the TM-mode triangular lattice of air-holes PhC structure.

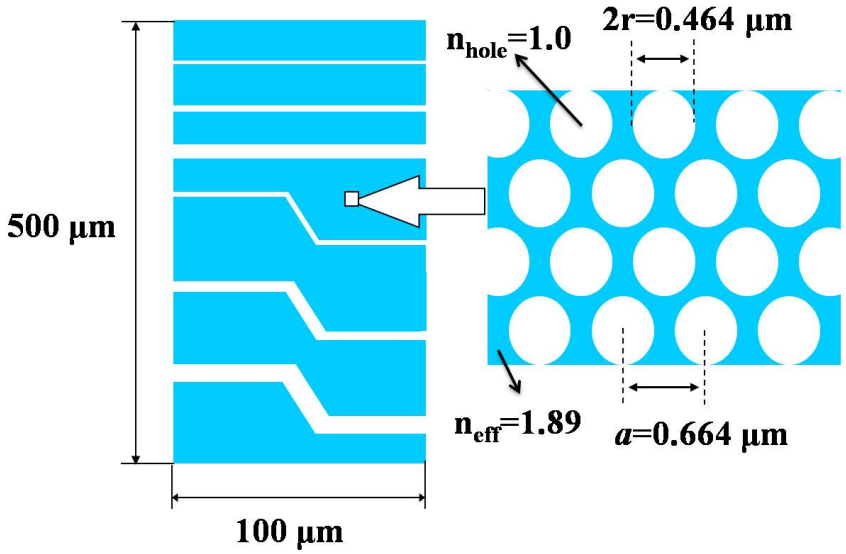

Figure 6.9: Schematic of PhC waveguide pattern design - consisting of Si-ion implanted SiO_2 layers and designed pattern of PhC waveguide.

6.2.4 Summary

In this subsection, we have analyzed the photonic bandgap and defect mode in a fused-silica substrate fabricated by Si-ion implantation and subsequent process of periodic structures by EBL using FDTD method. We have calculated the design parameters such as lattice constant (a=0.664 μm), radius of air-holes (r=0.224 μm) for PC and demonstrated that only TE mode triangular lattice of air-holes PC can effectively guide light of wavelength λ=1.55 μm in such structures. The PBG was estimated to be 16% gap. Next, we try to fabricate the designed pattern.

6.3 Fabrication of Novel PhC Waveguides

We start by describing the fabrication procedure for making PhC waveguides. Fig. 6.10 and Fig. 6.11 show the fabrication process flow schematics of the Si-ion implanted SiO_2 PhC waveguide. The fabrication process has two major steps: (1) The Si-ion implantation (Fig. 6.10) and (2) the processing 2-D PhC structures (Fig. 6.11).

6.3.1 Si-ion Implantation

In the first step (Fig. 6.10), Si-ions were implanted into a SiO_2 layer (≈500 nm thick, formed by thermal oxidation of a Si substrate) by using a 400-kV ion implanter in the

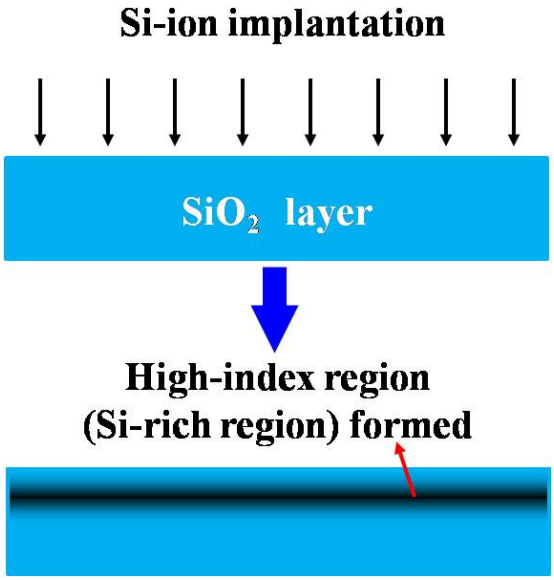

Figure 6.10: Schematic of the Si-ion implantation procedure - Si-ion implantation.

Takasaki ion accelerators for Advanced Radiation Application (TIARA) of the Japan Atomic Energy Agency. The implantation energy was 80 keV, and the implantation amount was 1×10^{17} ions/cm^2 [7, 8].

6.3.2 Electron Beam Lithography and Etching Proccess

Electron Beam Lithography (EBL) is a method to create nanoscale patterns in resist-coated substrate. A positive resist undergoes chain-scission and becomes soluble. A negative resist reacts to electrons by cross-linking or becoming insoluble. A solvent is used to dissolve away exposed soluble areas of a positive resist or leave behind the exposed insoluble areas on a negative resist. ZEP-520A is a positive electron beam resist suspended in Anisole, hence the A. Characterization of ZEP-520A involved determining what thicknesses of ZEP-520A were coated onto the substrate given a certain dilution and RPM. The optimization of ZEP-520A involved choosing a spin speed, thickness, e-beam parameters, and dilution corresponding to the clearest and most properly resolved features. The fabrication process is shown in Fig. 6.11. The overall process contains about 8 steps, which are hereby summarized in four major steps shown below:

1. Spin-coating EB resist (surface preparation, resist coating, pre-bake),

2. EB lithography (mask allignment, exposure),

3. Developing (development, post-bake), and

4. Etching (photoresist removal/processing).

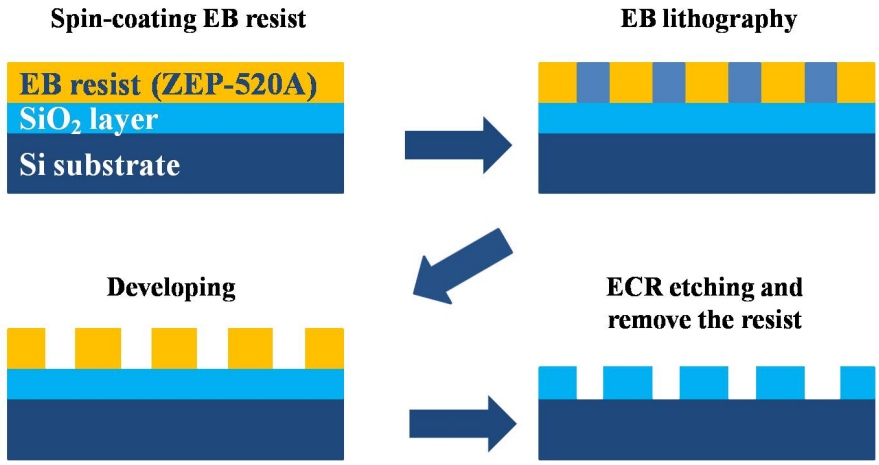

Figure 6.11: Schematic of the EB lithography and etching procedure - procedure for processing 2-D PhC structures.

Spin-coating EB resist

Surface preparation is the first and foremost thing to do. Because of the extreme delicacy of the lithography process, great care must be taken when preparing a surface for lithography. All surface contaminants must be cleaned to perfection. Some common surface irritants include dust, lint, bacteria, water, and oil. To remove such pesky particles, the surface is soaked and rinsed in a number of different chemicals. The surface is then primed with more chemicals to aid in the resist adhesion.

After the surface is cleaned and primed, the photoresist is applied by a method known as spin coating. The substrate was spin-coated with electron beam (EB) resist (ZEP-520A). Simply put, the surface is spun rapidly inside a vacuum, while being coated with the photoresist. The photoresist bonds uniformly to the surface, with the excess flying off during spinning. A coating solvent is then used to dissolve the buildup along the edge of the surface.

The pre-bake is a simple process of heating the surface in a convection oven or through a heated plate placed below the surface. Immediately after being spun, the substrate was placed on a hot plate, set to 180^{o}C, for 10 min. The purpose of the

pre-bake is to evaporate the excess coating solvent and to compact and harden the photoresist.

EB lithography

A photomask is a desired pattern that can be transferred onto a surface by means of light waves. The mask creates a sort of shadow between the light and the surface. Less light passes through sections blocked by the mask. Masks can be created by several different ways, but one of the most common and accurate methods is using an electron beam to etch a desired mask. The photoresist, surface, and mask are subjected to EB light via a EB lamp. In this case, the triangular lattice waveguide pattern was written in the resist using field-emission EB lithography using JSM-6500-F/Beam Draw (JEOL) with the optimized dose of 30 $\mu C/cm^2$.

Developing

During the development stage, chemicals are applied to the surface causing either a positive photoresist reaction or a negative photoresist reaction.

The developing solution (ZEP-RD) and rinsing solution (MD-B) were used. The substrate was placed on a hot plate, set to 140^{o}C, for 2 min. The post bake is used to stabilize and harden the photoresist. It also removes any trace of development chemicals.

Etching

The photoresist is only a means to an end; the important thing is the surface either underneath or below the photoresist. To remove the excess photoresist, simple solvents are used. The following cases are the results when the photoresist is applied on top or on bottom of the desired surface.

Etch-back: The photoresist is applied overtop the layer that is wanted to be patterned. The unwanted material is etched away. Lift-off: A layer is deposited over top of the photoresist. When the resist is removed, the unwanted layer is also removed.

The 2-D PhC structures were processed on the substrate using an electron cyclotron resonance (ECR) plasma etching apparatus (ANELVA, RIB-300) after developing the resist. The CHF_3 flow rate introduced into the vacuum chamber was 5 sccm, and the surface of the substrate was dry-etched under the acceleration voltage of 150 V

for 40 min. We have fabricated straight waveguides and 60^o bends waveguides with different number of air-holes filled in the triangular lattice.

6.4 Results and Discussion

We have carried out two different approach as shown in Fig. 6.12 and Fig. 6.14 in this fabrication and will here evaluate the results.

6.4.1 Fabricated Structure

The first approach is shown in Fig. 6.12. Here the processing of 2-D PhC structures on the SiO_2 substrate was done before Si-ion implantation was carried out. As we can see from the AFM image in Fig. 6.13, the result shows a crumbled PhC structure.

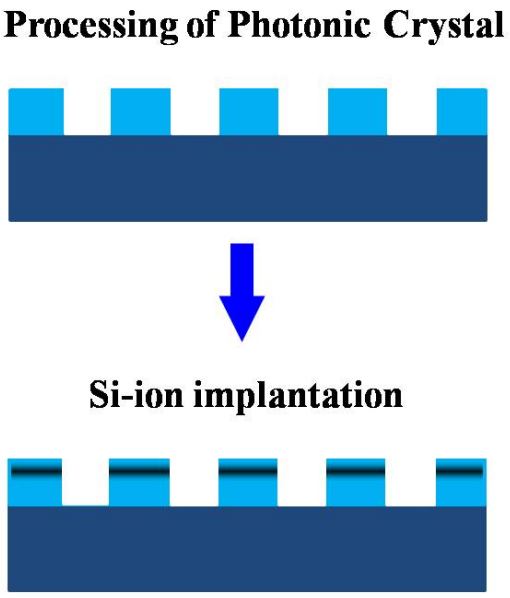

Figure 6.12: Schematic of the first approach - process of 2-D PhC structures before Si-ion implantation.

In order to restore the damage of Si-ion implantation, we annealed Si-ion implanted substrate before processing 2-D structure on it. The annealing conditions and the annealing setup are sown in table 6.1 and Fig. 2.7 (in section 2 of Chapter 2), respectively.

The second approach is shown in Fig. 6.14. Here the processing of 2-D PhC structures on the SiO_2 substrate was done after Si-ion implantation was carried out and

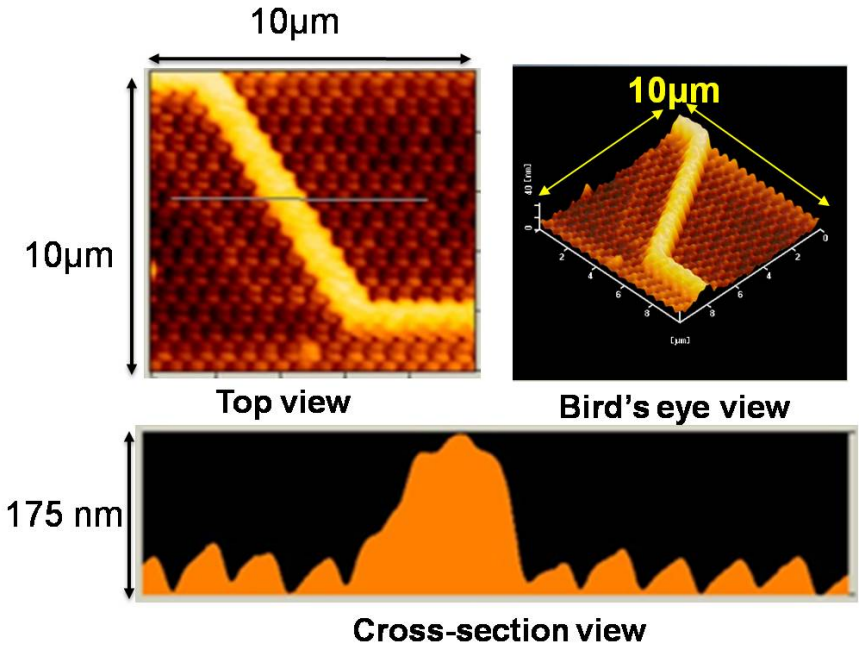

Figure 6.13: Fabricated structure utilizing the first approach - crumbled fabricated sample.

Table 6.1: Annealing conditions for PhC fabrication - Annealing of the substrate after Si-ion implantation restores the damages.

Annealing temperature:	700 ^{o}C
Annealing time:	20 min

subsequent annealing. As we can see from the AFM image in Fig. 6.15, the result shows a well defined PhC structure.

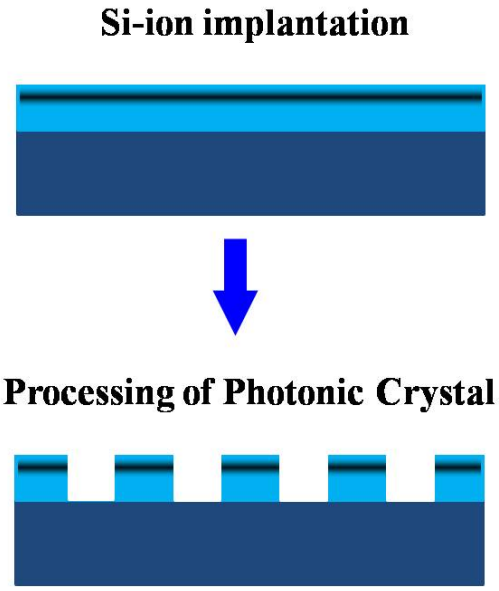

Figure 6.14: Schematic of the second approach - Si-ion implantation before processing of 2-D PhC structures.

After investigation, we found out that sputtering by the accelerated Si-ion could not be responsible for the crumbling in the first approach since it has been reported that sputtering takes place between the implant energy of 0.5 to 1 keV [12], while we had used 80 keV in our experiment. Also the sputtered region might not be recovered by annealing at high temperature after ion implantation. Therefore, we think that the cause might be the compressive stress [13] due to lattice expansion caused by the ion implantation on the thin walls of the cylindrical air holes, which in turn was weakened and consequently crumbled. More so, in the second approach, annealing of the sample after ion implantation had restored the lattice structures and removed the compressive stress, resulting in a well defined PhC structure after EB-Lithography and etching process(we also tried the sample without annealing, but still crumbled). Hence, the first approach cannot be used for the fabrication of PhC waveguide consisting of Si-ion implanted SiO_2 layers. We hereby propose a new fabrication method to define the PhC structures in the Si-ion implanted SiO_2 layers. The fabricated sample was measured using AFM and shows the lattice constant a=0.666 μm and radius of air-holes r=0.234 μm. The parameters of the fabricated sample were compared with the

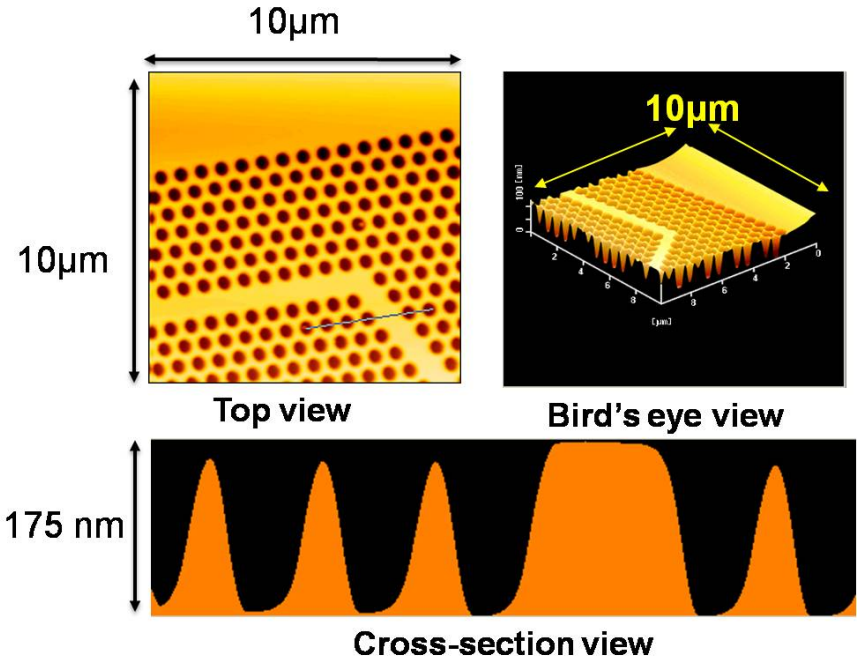

Figure 6.15: Fabricated structure utilizing the second approach - good fabricated sample (a=0.666 μm and r=0.234 μm).

designed parameters, and the result shows a good agreement with the designed values. In the near future, we will also demonstrate the experimental waveguiding properties of these structures. Therefore, we are carrying out an experimental characterization of the ion implanted sample in order to demonstrate its waveguiding properties and optimize its fabrication parameters.

6.4.2 Experimental Waveguide Properties

In order to be able to couple the light in and out of the waveguide, it is necessary to have access to both the input and the output facet of the guide. To do so, the sample was cleaved from both sides as shown in Fig. 6.16. Prior to cleaving, the sample was mechanically polished from the backside using Al_2O_3 polishing powder, and thinned from 500 to below 100 μm. This thinning enabled us to obtain smooth cleaved edges at both sides of the waveguide, which help to reduce the incertion losses during optical coupling from a glass fiber to the PhC waveguide.

Fig. 6.17 shows the result of light coupling into the PhC waveguide. We focused the laser light on the input facet of one piece. We first observed the sharp transmited

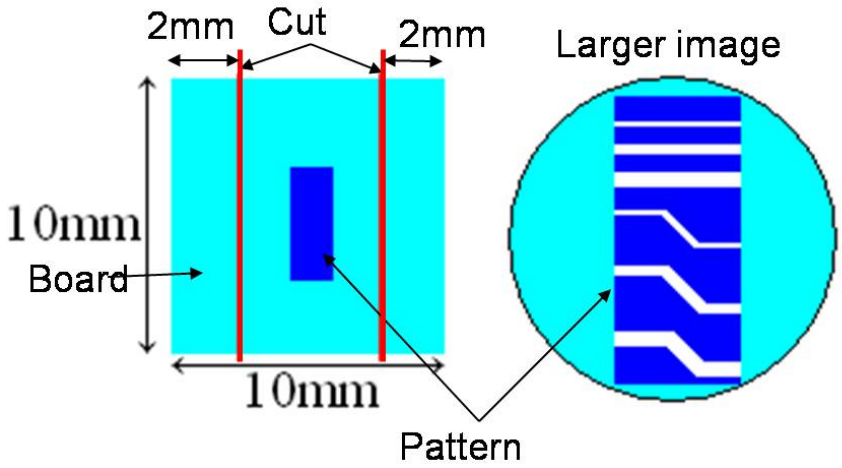

Figure 6.16: The Sample Preparation - The sample edges was cut with diamond-wire saw and polished in a rotating polish machine.

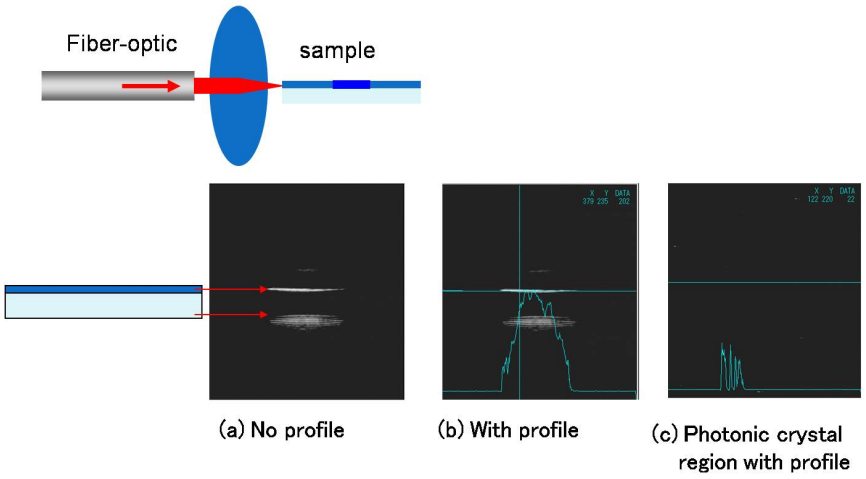

Figure 6.17: The Results of Direct Beam Focus - light propagation through the PhC waveguides with and without profiles.

light through the sample without the PhC by an ITV camera from the output facet. When the light is focused on the input facet with the PhC, we observed a weakly transmitted light at the output facet, which is also indicated by the computer profile as peaks denoting the presence of waveguiding in the sample. Since the fiber core diameter is around 10 μm, and the substrate thickness around 0.5 μm, coupling from the fiber to the waveguide was not efficient due to a large mode mismatch, and this problem remains to be solved. Therefore, we will investigate more of the waveguiding properties numerically using FDTD method in the following subsection.

6.4.3 Transmission, Reflection, and Loss properties (FDTD)

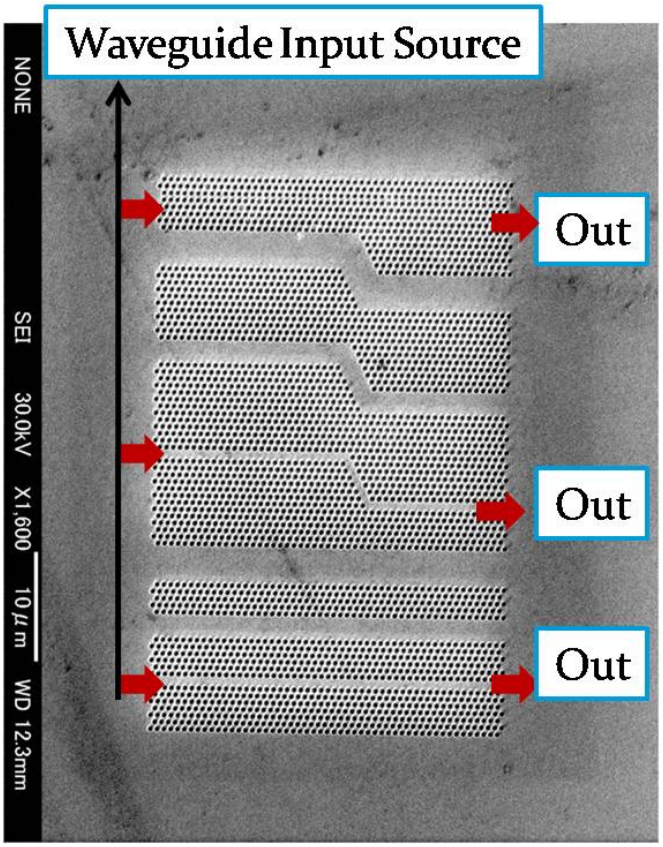

Figure 6.18: SEM image of the fabricated 2-D PhC with coupling - A gaussian source centered at wavelength, λ=1.55 μm was placed at the entrance of the waveguide.

The numerical characterization (see (5.46), (5.47) and (5.48) in Chapter 5 for more details) was carried out using the Meep FDTD [14] with perfectly matched layer (PML) boundaries. Fig. 6.18 shows the SEM image of fabricated pattern of the waveguides with

the input and output facets depicted for coupling of light. A gaussian source centered at wavelength, λ=1.55 μm was placed at the entrance of the waveguide, while the field amplitude was monitored at the output facet. The computational cell of 160 × 200 lattice constants was used. Fig. 6.19 shows the transmission properties of the PhC without defects, straight line (Fig. 6.20), and two 60^o bends (Fig. 6.21) waveguides. The insets show the magnetic field (H_z) pattern in the structures.

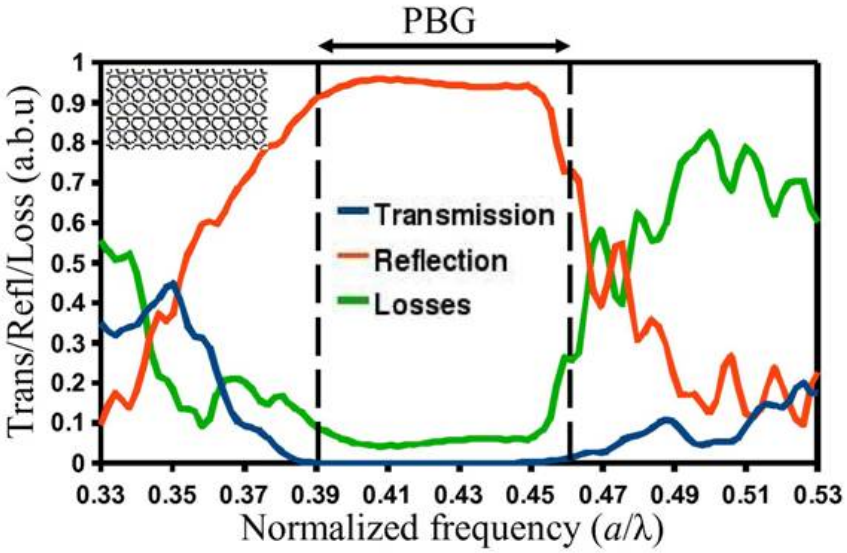

Figure 6.19: Transmission/Reflection properties of 2-D PhC without defects - No defects.

For the straight line (Fig. 6.20), we estimated the transmission of ≈ 100% and the guiding bandwidth is in agreement with the PBG. In the two 60^o bends (Fig. 6.21), we estimated the transmission of ≈ 80% and the overall bandwidth is also in agreement with the PBG. However, the guiding bandwidth is much smaller than the PBG. According to Chow et al. [15], the guiding modes that can be coupled with the input light have relatively flat dispersion, which has led to a narrow guiding bandwidth in the waveguide bend. The overall high transmission observed indicates that light is well guided within the 2-D PhC for the TE polarization only. These results are very usefull for connecting different optical components.

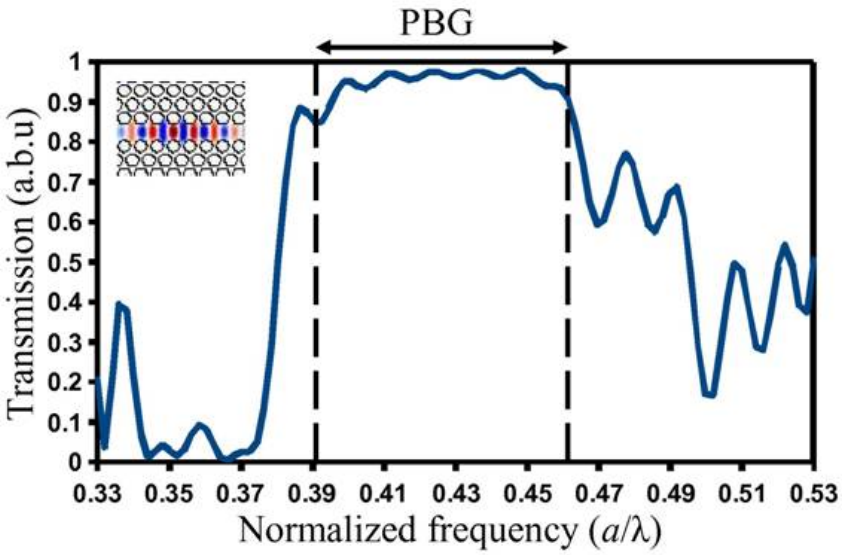

Figure 6.20: Transmission/Reflection properties of 2-D PhC with line defect - straight line guide.

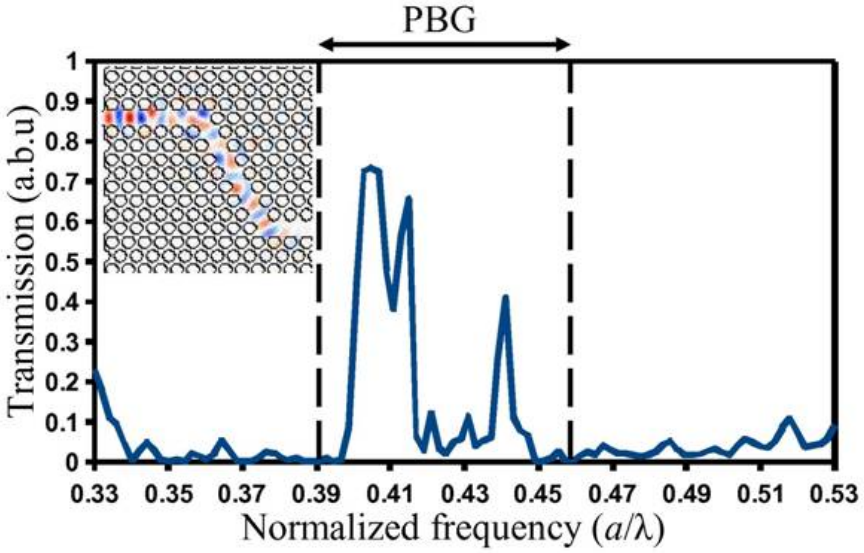

Figure 6.21: Transmission/Reflection properties of 2-D PhC with bend defects - two 60^o bend guide.

6.5 Summary

In this chapter, we have designed and fabricated a novel photonic crystal waveguide consisted of Si-ion implanted SiO_2 layers. Different number of straight and 60^o bends waveguide were designed and fabricated. We experimentally used two different approaches for the fabrication of the PhC waveguide. Evaluation of the results showed that, the second approach can be utilized to fabricate a well defined PhC structures consisting of Si-ion implanted SiO_2 layers. We also have measured the fabricated sample parameters and compared with the design parameters and estimated a relative error to be $< 0.2\%$, which is very small and has no significant effect on the calculated photonic bandgap. Numerical results showed that, straight line PhC waveguides can achieve $\approx 100\%$ transmission, while the 60^o bend showed $\approx 80\%$ transmission owing to the dispersion mismatch in the two 60^o bends.

References

[1] E. Yablonovitch: Phys. Rev. Lett. Vol. 58 (1987). p. 2059 110

[2] S. John: Phys. Rev. Lett. Vol. 58 (1987). p. 2486 110

[3] J. D. Joannopoulos R. D. Meade and J. N. Winn: *Photonic Crystals : Molding the flow of Light, Second edition* (Princeton NJ: Princeton University Press, 2008). 110, 115, 117

[4] O. Hanaizumi K. Ono Y. Ogawa and T. Matsumoto: Appl. Phys. Lett. Vol. 84 (2004). p. 3843 110

[5] N. Fukaya D. Oshaki and T. Baba: Jpn. J. Appl. Phys. Vol. 39 (2000). p. 2619 110

[6] M. Loncar T. Doll J. Vuckovic and A. Scherer: IEEE J. Lightw. Technol. Vol. 18 (2000). p. 1402 110

[7] L. Pavesi L.D. Negro C. Mazzoleni G. Franzo and F. Priolo: Nature Vol. 408 (2000). p. 440 110, 112, 120, 122

[8] K. Miura T. Tanemura O. Hanaizumi S. Yamamoto K. Takano M. Sugimoto and M. Yoshikawa: Nucl. Instr. and Meth. B Vol. 263 (2007). p. 532 110, 122

[9] A. Mekis J. C. Chen I. Kurland S. Fan P. R. Villeneuve and J. D. Joannopoulos: Phys. Rev. Let. Vol. 77 (1996). p. 3787 110

[10] A. V. Umenyi K. Miura and O. Hanaizumi: IEEE J. Lightw. Technol. Vol. 27 (2009). p. 4995 111, 113, 114, 115, 120

[11] J.F. Ziegler J.P. Biersack U. Littmark: *The Stopping and Range of Ion in Solids* (Pergamon, New York 1985). 113, 120

[12] H.J. Kang S.H. Ahn J.S. Lee and J.H. Lee: Int. J. Prec. Eng. and Manuf. Vol. 7 (2006). p. 1 127

[13] S. Sienz B. Rauschenbach A. Wenzel A. Lell S. Bader and V. Harle: Thin Solid Films Vol. 415 (2002). p. 1 127

[14] Meep FDTD, http://ab-initio.mit.edu/meep. 130

[15] E. Chow et al., *Proceedings of SPIE* vol. 4283 (2001) 453. 131

Chapter 7

Conclusions and Future Work

The field of Si-based optical materials and photonic crystals is very active and scientists throughout the world produce amazingly fast development in this area. This dissertation work cannot cover all these interesting areas, but provides an overview of these areas and an important base for future works. We have fabricated and analyzed the light emission properties of silicon nanocrystals utilizing Si-ion implantation, thermal annealing and PL measurements. Furthermore, we have studied, analyzed, and developed the photonic crystal modeling methods and especially based on the FDTD method and its applications to PhCs. Finally, we studied and analyzed photonic band gap materials using several analysis techniques, mainly TRIM and FDTD method. Novel photonic crystal waveguide is fabricated and analyzed both experimentally and numerically. Below we try to summarize the major works in this desertation and finally outline the areas of greater need for future work.

7.1 UV-Light Emission

We fabricated fused-silica substrates that emit UV-light by using Si-ion implantation and high-temperature annealing. In particular, we found a sharp UV peak around a wavelength of 370 nm after annealing at 1250 ^{o}C. The UV-light emission seems to originate from Si-ncs themselves and interface layers between Si-ncs and SiO_2 media. In addition to the UV-PL peak, we observed other PL peaks ranging from red to infrared wavelengths from our samples. However, we successfully obtained only the UV-light emission peaks by selecting the proper annealing temperatures. Therefore, it is important to further optimize the conditions in order to increase the UV-light

emission intensity. Such UV-light emission can be useful for a light source of higher-density optical-disk systems. If this kind of light source utilizing Si-based materials is realized, we will obtain many benefits as compared with III-V semiconductors, such as suitability for environment applications, lower cost, and matching for Si-based large-scale-integrated circuits in terms of their materials and fabrication processes.

7.2 FDTD

In this work we have developed a simple and easy 2-D FDTD method for calculating the band structure of triangular lattice 2-D photonic crystals using Yablonovitch's small rectangular unit cell. This unit cell enables the use of Cartesian FDTD to handle general triangular lattice and our translated periodic boundary conditions can be easily applied on the physical boundaries of the unit cell. Our method provides the following advantages: simple to understand and easy to implement; utilizes minimum computation time and space; our choice of Yablonovitch's small rectangular unit cell makes it possible to use initial field or point source in the simulation and it uses exactly one unit cell thus the band diagram is accurate and not folded. The photonic band diagrams for 2-D TE and TM modes using our approach of triangular lattice photonic crystal calculated with 2-D FDTD method are in good agreement with those calculated with PWE method.

Our implementation yields good convergence and accurate results. The use of windowing function such as Blackman window before the fourier transform can greatly reduce the number of grid points and total timesteps, which is very useful especially in 3-D simulation. However, a well-known disadvantage of FDTD method is that of accurately determining the resonant frequency due to the stair-casing error involved in FDTD discretization and numerical velocity error. These errors occur especially in the higher frequency (the TE is mostly affected). The staircase error can be greatly reduced by increasing the number of grid points per lattice constant or by using permittivity averaging or sub-cell method, while the numerical velocity error can be greatly reduced by compensating the velocity of light inside the medium. The 3-D FDTD method using this approach can be applied straightforward and is very easy.

7.3 Novel Photonic Crystal Waveguide

In this work, we have designed and fabricated a novel photonic crystal waveguide consisted of Si-ion implanted SiO_2 layers. The implantation profile and parameters were predicted by using TRIM software and showed that Si-rich regions are formed in the SiO_2 layers. Following this, we analyzed the photonic bandgap and defect mode in a fused-silica substrate using FDTD method. We have calculated the design parameters such as lattice constant (a=0.664 μm), radius of air-holes (r=0.232 μm) for PC and demonstrated that only TE mode triangular lattice of air-holes PC can effectively guide light of wavelength λ=1.55 μm in such structures. The PBG was estimated to be 16% gap.

Based on the calculated parameters, we also have shown a fabricated sample of the PC waveguide. The details of fabrication were also shown and discussed. Different number of straight and 60^o bends waveguide were designed and fabricated. We experimentally used two different approaches for the fabrication of the PhC waveguide. Evaluation of the results showed that, the second approach can be utilized to fabricate a well defined PhC structures consisting of Si-ion implanted SiO_2 layers. We also have measured the fabricated sample parameters and compared with the design parameters and estimated a relative error to be <0.2%, which is very small and has no significant effect on the calculated photonic bandgap.

The PhC waveguides were characterized both experimentally and numerically. Experimental characterization results showed the effect of PhC when light of wavelength λ=1550 nm was focused on the input facet, however, we found it difficult to achieve a clear transmission due to the coupling problem from fiber (10 μm) to PhC (0.666 μm). Numerical characterization results showed that, straight line PhC waveguides can achieve ≈100% transmission, while the 60^o bend showed ≈80% transmission owing to the dispersion mismatch in the two 60^o bends.

It is also worth noting that the actual refractive index of ion implanted sample can only be determined experimentally. Therefore more experiments are to be conducted in order to determine the refractive index of the ion implanted sample and demonstrate the experimental waveguiding properties of the sample and optimize its fabrication parameters.

7.4 Future Works

There remains a lot of research in this area. More theoretical and experimental works are needed to improve on this area of research. Nonlinear effects is also of interest and are not covered.

7.4.1 Light emission

Optimize the ion implantation and annealing conditions in order to increase the UV-light emission intensity. Investigate the dependency of PL wavelength/intensity on fabrication conditions.

7.4.2 Photonic crystal waveguides

Conduct experiment to determine the refractive index of the ion implanted sample. Demonstrate the waveguiding properties of the fabricated samples and optimize their fabrication parameters and extend to other applications.

7.4.3 Modified FDTD Method

Develop an FDTD desktop quick-tool for photonic crystal analysis utilizing the modified method. Develop a 3-D FDTD method using this approach and validate it.

Declaration

I herewith declare that I have produced this thesis without the prohibited assistance of third parties and without making use of aids other than those specified; notions taken over directly or indirectly from other sources have been identified as such. This thesis has not previously been presented in identical or similar form to any other examination board.

The thesis work was conducted from October 2006 to September 2010 under the supervision of Professor Osamu Hanaizumi at the Graduate School of Engineering, Gunma University, Kiryu Campus, Japan.

Umenyi Amarachukwu Valentine
September 2010
Gunma University, Kiryu, Japan.